



Estd. 1962  
"A++" Accredited by NAAC (2021)  
with CGPA 3.52

# SHIVAJI UNIVERSITY, KOLHAPUR

---

Volume-50 Issue-1 (Jan., 2024)

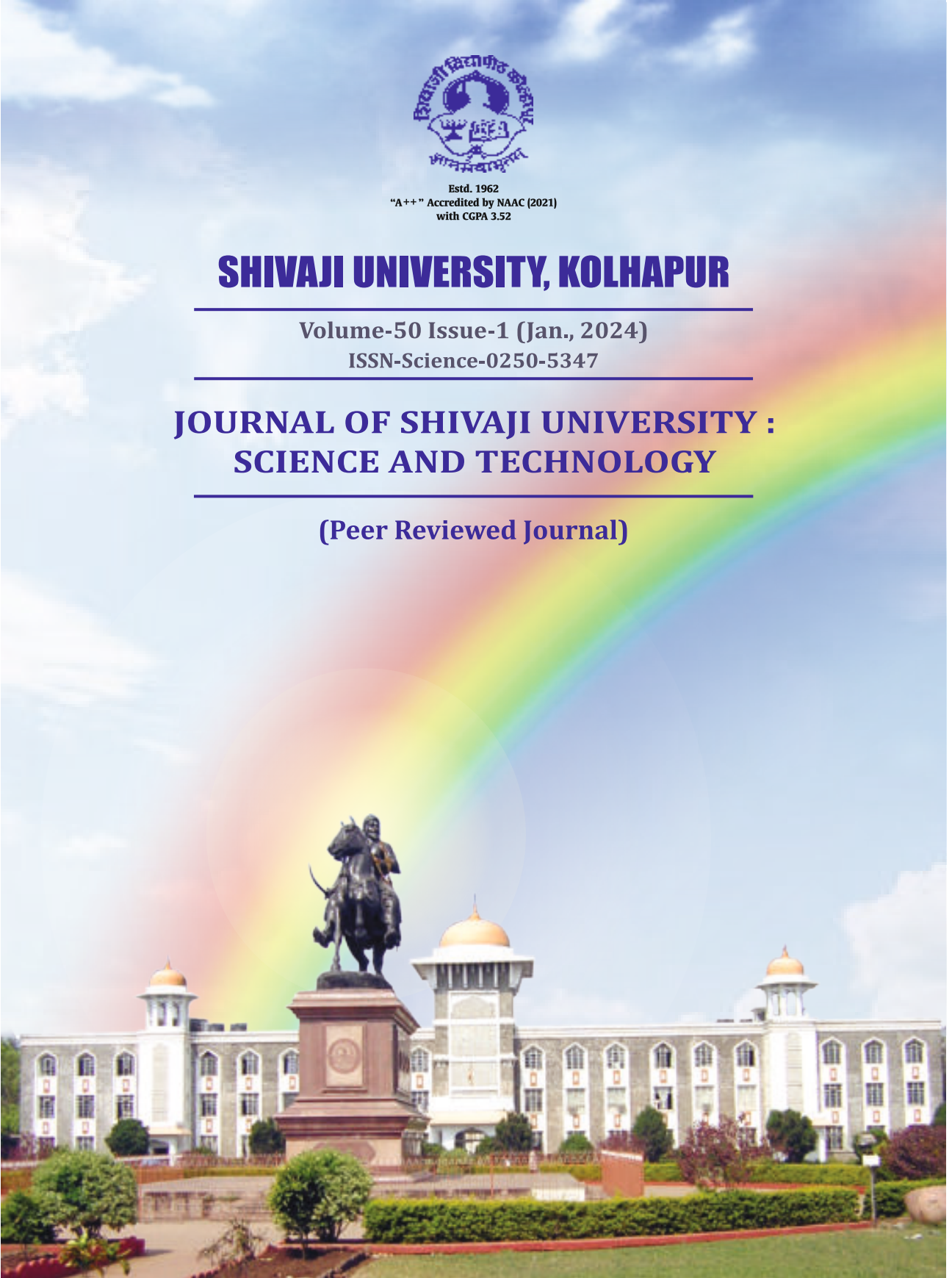
ISSN-Science-0250-5347

---

## JOURNAL OF SHIVAJI UNIVERSITY : SCIENCE AND TECHNOLOGY

---

(Peer Reviewed Journal)



# JOURNAL OF SHIVAJI UNIVERSITY : SCIENCE AND TECHNOLOGY

(Peer Reviewed Journal)

Volume-50, Issue-1 (Jan., 2024)

ISSN Science-0250-5347

## EDITORIAL BOARD OF THE JOURNAL

**Prof. (Dr.) D. T. Shirke**

Chairman

Hon'ble Vice Chancellor, Shivaji University, Kolhapur

**Prof. (Dr.) P. S. Patil**

Hon'ble Pro Vice Chancellor, Shivaji University, Kolhapur

**Dr. V. N. Shinde**

Registrar, Shivaji University, Kolhapur

**Prof. (Dr.) Smt. S. H. Thakar**

Dean, Faculty of Science & Technology, and  
Head, Department of Mathematics, Shivaji University, Kolhapur

**Prof. (Dr.) S. D. Delekar**

Editor,

Department of Chemistry, Shivaji University, Kolhapur

## MEMBERS OF THE EDITORIAL BOARD

<b>Prof. (Dr.) R. G. Sonkawade</b>	Head, Dept. of Physics, Shivaji University, Kolhapur
<b>Prof. (Dr.) Smt. J. P. Jadhav</b>	Head, Dept. of Bio-technology, Shivaji University, Kolhapur
<b>Prof. (Dr.) K. D. Sonawane</b>	Head, Dept. of Biochemistry, Shivaji University, Kolhapur
<b>Dr. S. N. Sapali</b>	Director, Dept. of Technology, Shivaji University, Kolhapur
<b>Prof. (Dr.) R. V. Gurav</b>	Head, Dept. of Botany, Shivaji University, Kolhapur
<b>Prof. (Dr.) S. B. Mahadik</b>	Head, Dept. of Statistics, Shivaji University, Kolhapur
<b>Dr. Smt. K. S. Oza</b>	Head, Dept. of Computer Science, Shivaji University, Kolhapur
<b>Prof. (Dr.) A. A. Deshmukh</b>	Head, Dept. of Zoology, Shivaji University, Kolhapur
<b>Prof. (Dr.) K. K. Sharma</b>	Head, Dept. of Nano Science & Technology, Shivaji University, Kolhapur
<b>Prof. (Dr.) S. D. Powar</b>	Head, Dept. of Geography, Shivaji University, Kolhapur
<b>Dr. Smt. A. S. Jadhav</b>	Head, Dept. of Environmental Science, Shivaji University, Kolhapur
<b>Prof. (Dr.) P. K. Gaikwad</b>	Head, Dept. of Electronics, Shivaji University, Kolhapur



Estd. 1962  
"A++" Accredited by NAAC (2021)  
with CGPA 3.52

---

---

**Shivaji University**

Kolhapur 416 004 (INDIA)

**JOURNAL OF SHIVAJI UNIVERSITY :  
SCIENCE AND TECHNOLOGY**

(Peer Reviewed Journal)

.....  
**Volume-50, Issue-1 (Jan., 2024)**  
.....

ISSN Science-0250-5347  
.....

- Contact Details -

**Prof. (Dr.) S. D. Delekar**

Editor, Journal of Shivaji University : Science and Technology  
and

Department of Chemistry

Shivaji University, Kolhapur 416 004 (India)

E-mail : [editor,jscitech@unishivaji.ac.in](mailto:editor,jscitech@unishivaji.ac.in)

website : <http://www.unishivaji.ac.in/journals/>

---

---

===== Shivaji University, Kolhapur =====

**JOURNAL OF SHIVAJI UNIVERSITY :  
SCIENCE AND TECHNOLOGY**

(Peer Reviewed Journal)

.....  
**Volume-50, Issue-1 (Jan., 2024)**  
.....

.....  
**ISSN Science-0250-5347**  
.....

- Editor -

**Prof. (Dr.) S. D. Delekar**

Journal of Shivaji University :  
Science and Technology

- Published by -

**Dr. V. N. Shinde**

Registrar,  
Shivaji University, Kolhapur 416004.

- Printed by -

**Shri. B. P. Patil**

Superintend  
Shivaji University, Kolhapur 416004.

The Editor, on behalf of the Editorial Board of the Journal of Shivaji University : Science and Technology, Vol. No. 49 (2) wishes to express his thanks to the contributing authors and the experts for acting as referees for the papers included in the issue.

**Published : Jan., 2024**

=====

**Journal of Shivaji University : Science and Technology**  
**Volume-50, Issue-1 (January, 2024)**

**INDEX**

<b>Sr. No.</b>	<b>Title of Research Article with Name of Author/s</b>	<b>Page No.</b>
1.	<b>Electrochemical Energy Storage Application of Chemical Bath Deposited Nanoporous Nickel Oxide</b> Radhika S. Desai, Pramod S. Patil, Uttam E. Mote, Dhanaji S. Dalavi	1
2.	<b>A Mini Review on Fe<sub>3</sub>O<sub>4</sub> for Microwave and Supercapacitor Application</b> Shital J. Shinde, Satyashila D. Ghongade, Pradnya G. Raje, Azeem M. Bagwan, Rajendra G. Sonkawade	14
3.	<b>Supercapacitive Behavior of Cobalt Oxide Thin Films by Successive Ionic Layer Adsorption and Reaction Method</b> Gayatri R. Chodankar, Suman A. Sawant, Sunny R. Gurav, Rajendra G. Sonkawade	31
4.	<b>A Review on Flexible Ferrite Composite Based Gas Sensors</b> Azeem M. Bagwan, Satyashila D. Ghongade, Pradnya G. Raje, Sheetal J. Shinde, Rakesh K. Sonkar, Rajendra G. Sonkawade	44
5.	<b>Growth of Grain Like Morphology of Metals Chalcogenide via Successive Ionic Layer Adsorption and Reaction Method</b> B. M. Patil, V. L. Patil, N. L. Tarwal, S. R. Bhosale, R. R. Bhosale, P. D. Kamble, P. S. Patil, S. A. Vanalakar	53
6.	<b>Gas Sensor Based on Metal Oxide-Polymer Composites</b> Satyashila D. Ghongade, Pradnya G. Raje, Shital J. Shinde, Azeem M. Bagwan, Rajendra G. Sonkawade	66
7.	<b>Perovskite Oxide Based Resistive Switching Devices for Non-Volatile Memory: A Mini-Review</b> Lahu. D. Namade, Tukaram. D. Dongale, Amitkumar. R. Patil, Namrata. A. Narewadikar, Keshav. Y. Rajpure	76

---

8.	<b>Supercapacitive Performance of Chemically Deposited CuO Thin Film</b> Suman A. Sawant, Sunny R. Gurav, Gayatri R. Chodankar, Pradnya G. Raje, Rajendra G. Sonkawade	90
9.	<b>Successive Ionic Layer Adsorption and Reaction Method Prepared Mn<sub>3</sub>O<sub>4</sub> Thin Film for Supercapacitor Application</b> Sunny R. Gurav, Gayatri R. Chodankar, Suman A. Sawant, Rajendra G. Sonkawade	101
10.	<b>Effect of Artificial Negative Ions on the Nutrition and Growth of Wheat (Triticum Aestivum) using Negative Air Ion Generator</b> Subhash D. Pawar, Pratima S. Sankpal, Satvashila B. Nalawade, Mamata S. Singh, Nilesh S. Shinde, P.H. Mangsule, S. B. Jogdand	109
11.	<b>Synthesis and Characterization of Copper Oxide Nanoparticles via Chemical Route for Antibacterial Activity</b> Shweta M. Pawar, Vithoba L. Patil, Sumit D. Korade, Sarika B. Dhavale, Satyajeet S. Patil, Pramod S. Patil	120
12.	<b>Hydrothermally Prepared WO<sub>3</sub>-Nanostructure as an Efficient Electrode Material for Supercapacitor</b> U. V. Shembade, S. D. Dhas, M. D. Patil, T. T. Bhosale, N. B. Chougale, M. G. Magadum, S. V. Jadhav, S. R. Ghatage, A. V. Moholkar	130

---

**Department of Physics**  
**Shivaji University, Kolhapur**  
**Journal of Shivaji University : Science & Technology**  
**Volume-50, Issue-1 (January, 2024)**  
**Departmental Editorial Board**

<b>Sr. No.</b>	<b>Name of the Faculty</b>	<b>Editorial Board Designation</b>
1.	Prof. (Dr.) R. G. Sonkawade	Chairman
2.	Prof. (Dr.) V. J. Fulari	Member
3.	Prof. (Dr.) K. Y. Rajpure	Member
4.	Dr. A. V. Moholkar	Member
5.	Dr. R. S. Vhatkar	Member
6.	Dr. N. L. Tarwal	Member
7.	Dr. M. V. Takale	Member
8.	Dr. J. B. Yadav	Member

---

---

# Electrochemical Energy Storage Application of Chemical Bath Deposited Nanoporous Nickel Oxide

Radhika S. Desai <sup>a</sup>, Pramod S. Patil <sup>b</sup>, Uttam E. Mote<sup>c</sup>, Dhanaji S. Dalavi\*<sup>a</sup>

<sup>a</sup>Department of Physics, Krishna Mahavidyalaya, Rethare Bk 415108, MS, India

<sup>b</sup>Department of Physics, Shivaji University, Kolhapur 416004, MS, India

<sup>c</sup>Shrimant Babasaheb Deshmukh Mahavidyalaya, Atpadi 415301 MS, India

\*Corresponding author: dhanuphysics@gmail.com (Dr.Dalavi D. S.)

---

---

## ABSTRACT

*Nickel oxide with a nanoporous rose petal-like network has been synthesized by the chemical bath deposition (CBD) method. Its film formation mechanism is investigated and it was confirmed that the thickness and morphology of synthesized nanoporous NiO, is influenced by variation in the deposition times. The SEM and AFM analysis displayed a nanoporous rose petal-like structure network comprising wide cracks. As the deposition time increases, the network becomes denser or more packed as the width of the crack decreases. The XRD patterns of annealed NiO films indicated low intense peaks, confirming cubic phase of NiO crystals. The fabricated electrode delivers the specific capacitance  $142 \text{ F g}^{-1}$  at a  $10 \text{ mV sec}^{-1}$  scan rate. It maintains 90 % of its initial capacitance after 1000 charge/discharge cycles, demonstrating one of the most promising electrode materials for high energy storage performance.*

## KEYWORDS

*NiO, metal oxide, chemical bath deposition, supercapacitor, energy storage, rose-petal*

.....

## 1. INTRODUCTION

In electrochemical energy storage systems (EESs), supercapacitors (SCs) or electrochemical capacitors (ECs) are always the focus of attention due to their ability to deliver energy very quickly, rapid charge/discharge process, and excellent cycle stability.[1] Based on the charge-storage mechanisms, ECs are categorized into two fundamental types, electrochemical double-layer capacitor (EDLC) and pseudocapacitor (PSC). During the electrostatic (non-faradic) charge storage process in EDLC, ions/electrons accumulate on the electrode surface. Electrochemical

(faradic) charge storage in PSCs occurs at the surface and near-surface of electrode material. Carbon and its derivatives are suitable as EDLC electrodes, while transition metal oxides (TMOs) and conducting polymers are appropriate for use as PSCs electrodes.[2] The high specific capacitance of TMOs compared to that of carbon-based materials makes them more appropriate for SC applications and therefore they are being widely studied.

Various low-cost high surface area EDLC materials ex. Carbonaceous materials, then high capacitance and easy to construct TMOs such as ruthenium dioxide ( $\text{RuO}_2$ ), manganese oxide ( $\text{MnO}_2$ ), iridium oxide ( $\text{IrO}_2$ ), Nickel oxide ( $\text{NiO}$ ), and highly conducting polymers (CPs) such as Polyaniline (PANI), polythiophene, Polypyrrole (PPy), etc. are being widely studied for energy storage applications.[3][4] Generally, metal oxides have high theoretical capacitance, but it suffers from poor  $\text{Li}^+$  storage/release properties and low electrical conductivities.[5] The design and synthesis of nanostructured TMOs have attracted significant interest and have made a great impact in many applications such as electrochromism, energy storage, gas sensors, and many more, due to their highly exposed active crystal planes with many promising properties.[6–8]

Nickel oxide ( $\text{NiO}$ ) has drawn increasing attention with a wide variety of applications such as an electrode in lithium-ion micro-batteries[9], electrochromic coatings[10], gas and temperature sensing [11], water splitting [12], plasmonic photocatalyst for solar  $\text{H}_2$  evolution [13], as hole transporting layers in organic solar cells [14] etc. Among the numerous low-cost oxides investigated, nickel oxide is a promising material with its theoretical capacitance of  $2573 \text{ F g}^{-1}$ , high thermal and chemical stability, excellent redox behavior, and environmentally friendly properties. But its poor electrical conductivity and small potential window limit their applications.[15] Up to now, remarkable progress has been made in the formation of various nanostructures of  $\text{NiO}$  for electrochemical applications. Patil and coworkers demonstrated a CBD approach for the fabrication of cubic  $\text{NiO}$  thin films on a glass substrate. The resulting films showed a specific capacitance of  $167 \text{ F g}^{-1}$  at  $20 \text{ mV s}^{-1}$  in a  $2 \text{ M KOH}$  electrolyte.[16] Salokhe et al reported the physical properties of 2D  $\text{NiO}$  nanosheets developed via the CBD method for various applications. They investigated that adhesion property depends on the contact interface between the substrate and deposited film [17]. Higher packing density indicates better adhesion.[18] Afterward, a hierarchical porous  $\text{NiO}$  superstructure with a specific capacitance of  $710 \text{ F g}^{-1}$  at  $1 \text{ A g}^{-1}$  and 98 % capacitance retention after 2000 charge-discharge cycles was reported by Yuan et al.[19] Hydrothermally synthesized  $\text{NiO}$  nanoflakes resulted in a capacitance of  $137.7 \text{ F g}^{-1}$  at  $0.2 \text{ A g}^{-1}$  current density.[20] Yan et al synthesized the porous  $\text{NiO}$  hollow spheres with the template-free CBD method. The synthesized film exhibited a specific capacitance of  $346 \text{ F g}^{-1}$  at  $1 \text{ A g}^{-1}$  after the 2000 cycle.[21] A variety of methods including sol-gel

process [22], electrochemical deposition [23], hydrothermal synthesis [20], electrospinning [24], hot-filament metal-oxide vapor deposition (HFMOVD) technique [25] and chemical bath deposition (CBD) [21] have been developed to fabricate NiO nanostructures.

Using the chemical bath deposition method (CBD) thickness, morphology, and porosity of the synthesized film can be easily controlled with the help of preparative parameters such as deposition time, and concentration of the solution.[26] Nanoporous structures provide a large surface area that can assist in a fast ion/electron transfer path and consequence into electrodes with enhanced electrochemical properties.[27] Herein, we present the simple CBD approach to developing nanoporous nickel oxide (NiO) network with interconnected rose petals-like morphology including wide cracks. The resulting network was developed on an ITO glass substrate. The influences of deposition time on the morphologies and its consequence on the specific capacitance of as-synthesized NiO thin film have been investigated. The synthesis strategy reported here may provide an effective route to develop a unique architecture for efficient energy storage applications.

## **2. EXPERIMENTAL SECTION**

### **2.1. Materials**

Nickel sulphate ( $\text{NiSO}_4 \cdot 6\text{H}_2\text{O}$ ) with 99 % purity, Potassium pyrosulfate ( $\text{K}_2\text{S}_2\text{O}_8$ ), and ammonia (25-28%) purity were purchased from Loba Chemie and Sd. Fine respectively. All chemicals were used as received without further purification. Indium-doped tin oxide (ITO) with a sheet resistance of 25-30  $\Omega/\text{cm}^2$  was purchased from Kintec Corp. Ltd, Hong Kong is used for the current study.

### **2.2. Preparation of nanoporous NiO**

NiO thin films were grown on ITO substrate via the CBD method followed by annealing. Firstly, a precursor solution was prepared by using 1M  $\text{NiSO}_4 \cdot 6\text{H}_2\text{O}$ , 0.25M  $\text{K}_2\text{S}_2\text{O}_8$ , and aqueous ammonia in a 4:3:1 proportion in a 250 ml beaker. Indium-doped tin oxide (ITO) coated transparent conducting glass substrates were ultrasonically cleaned in acetone and de-ionized water. These samples were immersed vertically in the prepared solution and then extracted after a time interval of 20, 40, and 60 min. Then the films were washed with deionized water and after that, the targeted NiO nanopetals were obtained by annealing at 300°C in the air for 90 min. The obtained nanopetals synthesized at different deposition times of 20, 40, and 60 min were denoted as NP<sub>20</sub>, NP<sub>40</sub>, and NP<sub>60</sub> respectively.

### **2.3. Characterizations**

The structural properties and surface morphology of the films were examined from an X-ray diffractometer (Philips, PW 3710, Almelo, Holland) operated at 25 kV, 20 mA with Cu  $\alpha$  radiation ( $\lambda=1.54\text{\AA}$ ) and scanning electron microscopy (SEM)

(Model JEOL-JSM-6360, Japan), operated at 20 kV respectively. The infrared (IR) spectrum was examined with a Perkin-Elmer IR spectrophotometer (model-100) of the powder collected from all NiO samples in 400-4000  $\text{cm}^{-1}$  the spectral range. The pellets were prepared, by mixing KBr with NiO powder (300:1 ratio) and then pressing the powder into two pieces of polished steel. The electrochemical performance was analyzed at different scan rates using cyclic voltammetry (CV) in a 1M KOH electrolyte in a conventional three-electrode arrangement that included NiO thin film, graphite, and saturated calomel electrode (SCE) as the working, counter, and reference electrode respectively using electrochemical quartz crystal (EQCM) measurements (model-CHI-400A) made by CH Instrument, USA.

### 3. RESULTS AND DISCUSSION

The x-ray diffraction (XRD) patterns of as-synthesized NP<sub>20</sub>, NP<sub>40</sub>, and NP<sub>60</sub> samples are shown in **Figure-1**. The XRD pattern exhibits three peaks indexed approximately at  $2\theta = 37.24^\circ$ ,  $43.29^\circ$  and  $62.87^\circ$ , along (111), (200), and (220) planes, corresponding to a cubical crystalline NiO phase (ICDD 04-002-0665) respectively, which reveals that NiO has successfully grown on the ITO glass substrate.[28]

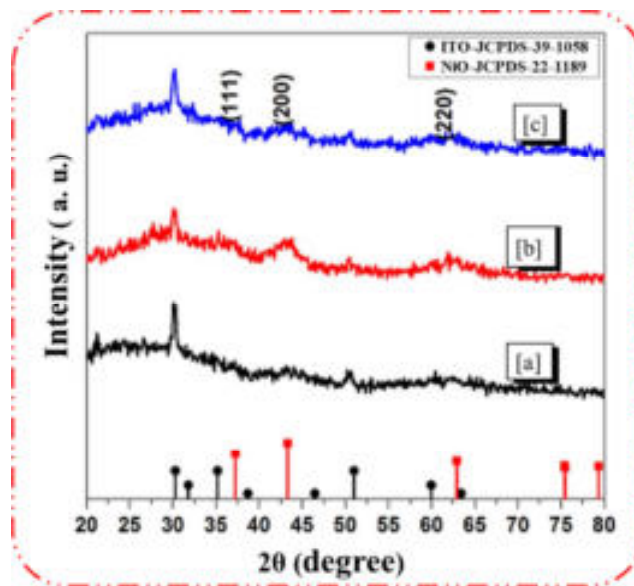


**Figure 1** XRD pattern of the (a) NP<sub>20</sub> (b) NP<sub>40</sub> and (c) NP<sub>60</sub> thin film samples. The vertical red lines represent the standard ICDD data (ICDD 04-002-0665) for NiO

Due to the highly porous network of synthesized film, the low peak intensity arises in the XRD.[29] The ITO substrate peaks are denoted by vertical black lines (ICDD-00-

039-1058).[30] The particle size (D), micro strain ( $\epsilon$ ), dislocation density ( $\delta$ ) and distortion parameters (g) for all three samples NP<sub>20</sub>, NP<sub>40</sub>, and NP<sub>60</sub> from XRD spectra was calculated by using the formulae given below,

$$D = \frac{k\lambda}{\beta \cos \theta} \dots \dots \dots (1)$$

$$\epsilon = \frac{\beta \cos \theta}{4} \dots \dots \dots (2)$$

$$\delta = \frac{n}{D^2} \dots \dots \dots (3)$$

$$g = \frac{\beta}{\tan \theta} \dots \dots \dots (4)$$

Where,  $k$  is Scherrer constant is shape factor usually taken as 0.9 for spherical crystallites,  $\lambda$  is the X-rays wavelength (here for Cu-K $\alpha$  = 1.542 Å,  $\theta$  is the angle of diffraction,  $\beta$  is the Full Width at Half Maxima (FWHM) obtained from XRD pattern [31][32] and  $n$  is a factor, which is almost equal to unity for minimum dislocation density. The Williamson–Hall equation interrelate the particle size (D), micro strain ( $\epsilon$ ) by the following relation and partially originates from the Debye– Scherrer equation (1) given above [30],

$$\beta \cos \theta = \frac{k\lambda}{D} + 4 \epsilon \cos \theta \dots \dots \dots (5)$$

The particle size (D), micro strain ( $\epsilon$ ), dislocation density ( $\delta$ ) and distortion parameters (g) of all the samples were calculated using above formulas, which are mentioned in Table-1 below. It can be easily noticed from the analyzed data that crystalline size increase with the deposition time.

Table 1 The observed average crystalline size, micro strain, dislocation density and distortion parameters of the NP<sub>20</sub>, NP<sub>40</sub>, and NP<sub>60</sub>.

Sample	Average Crystalline size (nm) (D)	micro strain ( $\epsilon$ )	dislocation density ( $\delta$ )( $\times 10^{22}$ )	distortion parameters (g)
NP <sub>20</sub>	16.20	0.041	77.59	0.311
NP <sub>40</sub>	18.23	0.037	59.24	0.245
NP <sub>60</sub>	37.34	0.033	65.63	0.240

The IR transmission spectra of without and with annealing treatment for NP<sub>20</sub> sample is recorded in the range of 400–4000 cm<sup>-1</sup> as shown in **Figure-2a & 2b** respectively. The broadband centered around 3400 cm<sup>-1</sup> and 1630 cm<sup>-1</sup> are attributed to the O-H

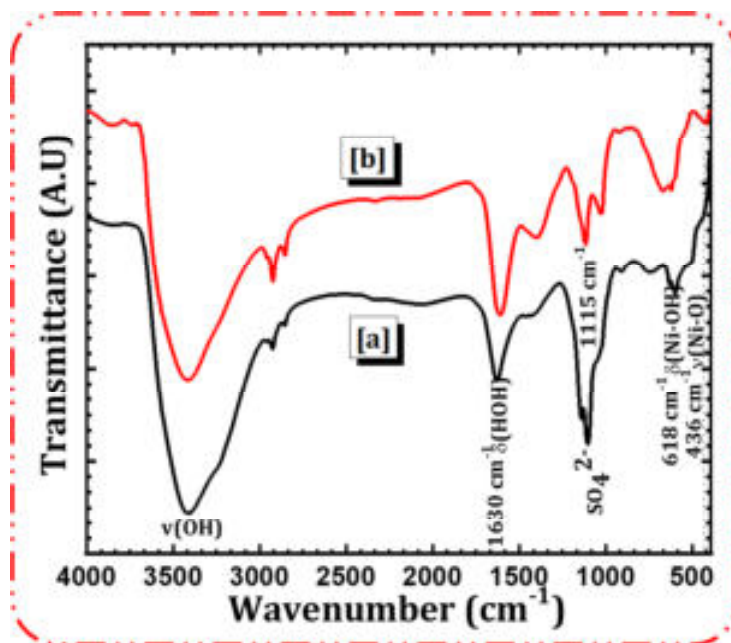


**Figure 2** FT-IR transmittance spectra of the (a) without annealing and (b) after annealing NP<sub>20</sub> thin film sample.

stretching vibrations and H-O-H bending vibrations.[33] The peak positioned at  $1115\text{ cm}^{-1}$  corresponds to stretching vibrations of sulphate ions. The peaks around  $618\text{ cm}^{-1}$  and  $436\text{ cm}^{-1}$  correspond to the Ni-OH and Ni-O stretching vibrations respectively and they confirm the formation of nanostructured NiO.[34] FTIR spectra show that annealing leads to the formation of hydrated NiO.

XPS study investigates the chemical composition and electronic states of NP<sub>20</sub> sample deposited on ITO substrate. The survey spectrum of NP<sub>20</sub> as shown in **Figure- 3(a)** confirms the presence of Ni, O, and C (from surrounding) elements and assures the surface is clean [35]. **Figure-3b and 3c** display the highly resolved scans of Ni 2p core-level spectra and O-1s spectra. The Ni-2p comprises two peaks of Ni-2p<sub>3/2</sub> and Ni-2p<sub>1/2</sub> at 855.62 eV and 873.24 eV respectively with binding energy separation of 17.62 eV.[36] The shake-up processes lead to the two Ni satellite peaks, which are located at 861.03 eV and 879.18 eV. The Ni-OH bonds developed mainly from NiOOH groups attached to the NiO surface.

This indicates that the product is mainly NiO and the existence of a small amount of NiOOH on the surface of the NiO film layer.[37] The O-1s XPS spectrum of the NP<sub>20</sub> sample is shown in **Figure-3c**, including three peaks at 529.13 eV, 531.16 eV, and 532.90 eV. As reported by Oswald et al. the 529.13 eV and 531.16 eV binding energy peaks of O-1s core level correspond to O<sup>2-</sup> anions of NiO and Ni<sub>2</sub>O<sub>3</sub> respectively.[38]

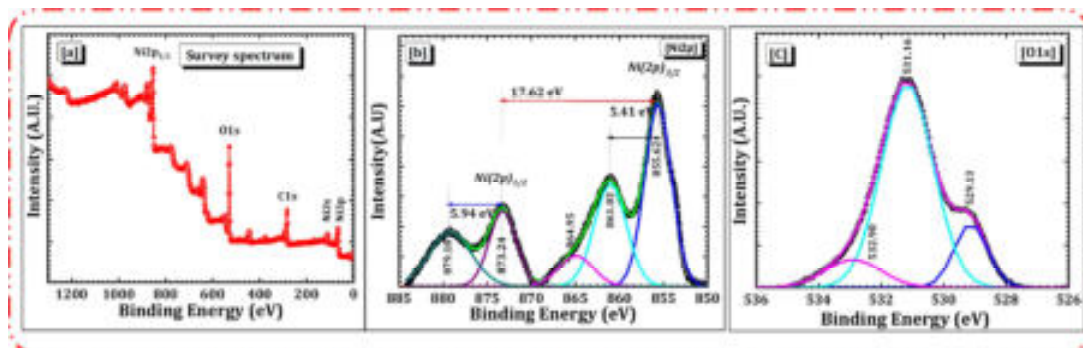


**Figure 3** XPS spectra of NP<sub>20</sub> thin film sample (a) Survey spectra (b) Ni 2p core-level spectra and (c) highly resolved O-1s spectra.

SEM images of as-grown nickel oxide films developed at different deposition times are shown in **Figure-4 (a-c)**. SEM study reveals that the synthesized samples exhibit a porous architecture, that comprises interconnected rose-petal-like structures with wide cracks which have been grown on the ITO glass substrate. Careful observation of SEM images also confirms that, as the deposition time increases, the network becomes denser or more packed as the width and number of the crack decreases. Deposition time affects the growth mechanism and the film thickness. Such highly dense and thick structures will lower the electron transfer velocities and electrolyte diffusion efficiency.[39] The wide channels and a relatively large number of channels exist in the NP<sub>20</sub> sample. The highly porous interpenetrating and connected petal structures may assist to acquire a high surface area that enables active-site accessibility to encourage effective ion transport in the redox process, which affects the specific capacitance of the synthesized electrode.

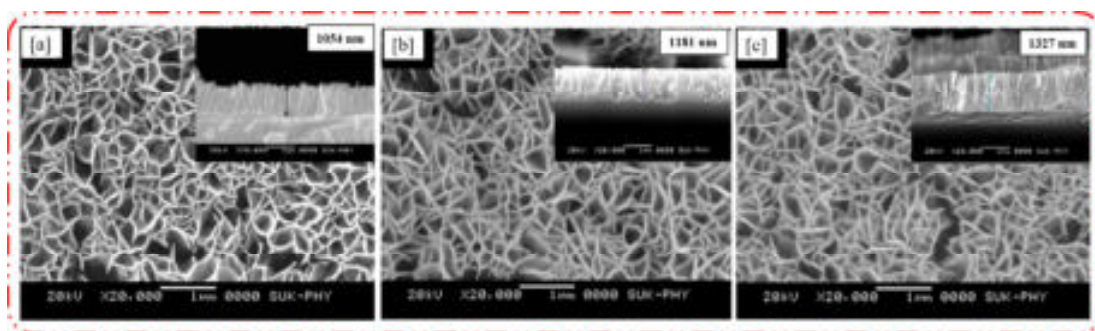


**Figure 4** Scanning electron microscopy (SEM) images of (a) NP<sub>20</sub> (b) NP<sub>40</sub> and (c) NP<sub>60</sub> annealed thin film samples at  $\times 20,000$  magnification (inset displays the cross-section images  $\times 20,000$  magnification.)

Here the highly porous interpenetrating and interconnected petals via deep channels, help to increase the mobility of the ions through the easily accessible sites in the network. [40] The more detailed structure information is illustrated by taking the cross-section of the all the samples as shown in the inset of **Figure-4 (a-c)**. The SEM cross sectional analysis as a function of deposition time indicates that the film thickness can be easily tuned by controlling the deposition time. As deposition time increases from 20 to 60 minutes, the film thickness increases from 1054 nm to 1327 nm.

Such nanoporous networks facilitate control over the available surface area to enable active-site accessibility and porosity structure, influencing ion transport kinetics in the redox process. **Figure-5 (a-b)** shows 2D and 3D atomic force microscopy (AFM) surface topographic images of NP<sub>20</sub> film. 2D image shows the interconnected rose-petals network and the 3D image shows a nano thorn-like

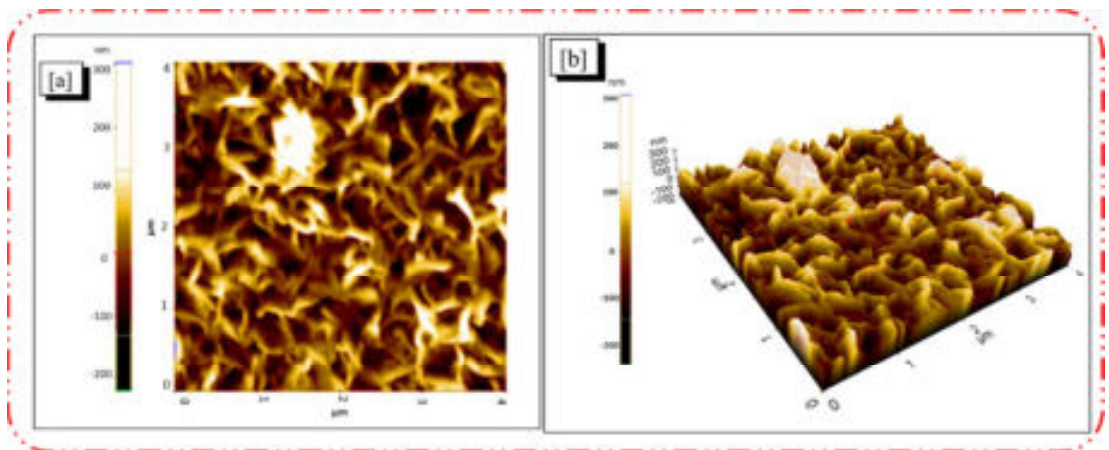


**Figure 5 (a-b) 2D and 3D AFM surface topographic image of NP<sub>20</sub> sample**

structure on the top edge of the petals.[41]

Electrochemical properties of synthesized porous NiO thin films were studied with cyclic voltammograms (CVs) as shown in **Figure-6**. To calculate the specific capacitance all the samples were recorded within a potential window of -0.33 V to 0.3 V (SCE) at a 10 mV s<sup>-1</sup> scan rate in 1 M KOH electrolyte. The specific capacitance was calculated by using the equation given below,

$$\text{Specific Capacitance} = C_s = \frac{\int_{V_f}^{V_i} I(V)dV}{2 v m V} \text{ --- (6)}$$

where  $C_s$  is the specific capacitance of the electrode per unit mass of the active materials (in  $F \cdot g^{-1}$ );  $\int_{V_f}^{V_i} I(V)dV$  is the integral area of CV curve;  $V$  is the potential window (in V),  $v$  is scan rate in  $mV \cdot sec^{-1}$ ;  $m$  is the mass of the active electrode materials (in grams). Specific capacitance for these developed NP<sub>20</sub>, NP<sub>40</sub>, and NP<sub>60</sub> films were calculated based on CV analysis and found to be  $142 F g^{-1}$ ,  $75 F g^{-1}$ , and  $54 F g^{-1}$ , respectively at a  $10\text{-}mV s^{-1}$  scan rate.

These values are comparatively higher than the NiO film developed by the CBD method and studied in two different electrolytes by Inamdar et al. [42] As the deposit time increases, the specific capacitance decreases, which may be due to the following reasons. As the deposition time increases, the thickness of the film increases (from 1054 nm to 1327 nm), and from SEM we can notice that the film becomes dense and compact. This results in increased equivalent series resistance, as it prevents easy ion transport through the network which is the combined effect of the reduced pore size

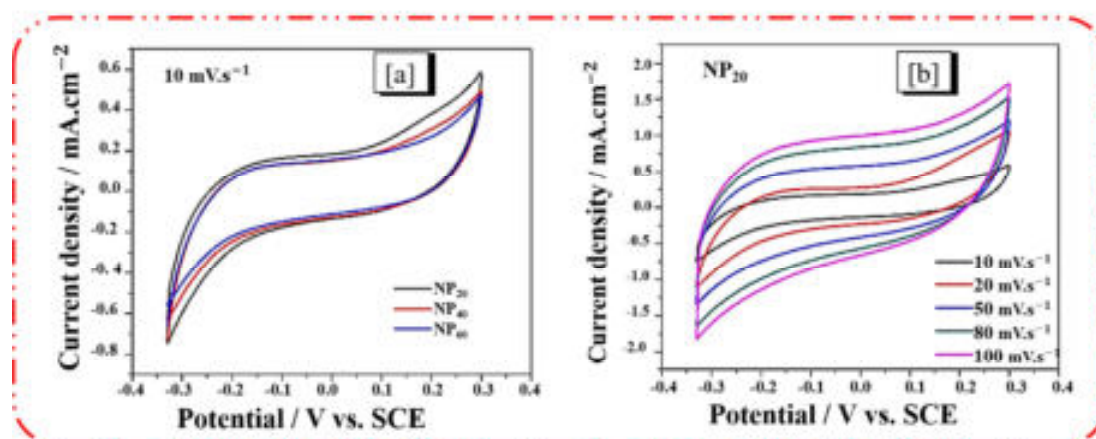


**Figure 6** Cyclic voltammograms (CV) of the NP<sub>20</sub>, NP<sub>40</sub>, and NP<sub>60</sub> samples, within a potential window of  $-0.33$  to  $+0.3$  V vs. SCE at  $10 mV s^{-1}$  scan rate. CVs curves performed at scan rates from  $10$  to  $100 mV s^{-1}$  in  $1M$  KOH electrolyte for NP<sub>20</sub> film within the potential window of  $-0.33$  to  $+0.3V$  vs. SCE

and pore-clogging.

**Figure-6** demonstrates the redox mechanism of the NP<sub>20</sub> sample at  $10 mV \cdot s^{-1}$  to  $100 mV \cdot s^{-1}$  scan rate. The CV profile appears as an almost rectangular shape. As the scan rate increases, both the anodic and cathodic peaks of the CV profile are shifted to more negative and positive values respectively, which indicates that the capacitance of the synthesized film is due to the pseudocapacitive mechanism.[43]

As the scan rate increased, the area under the curve gradually increased and the capacitance was found to decrease. The redox reactions between  $\text{Ni}^{2+}$  and  $\text{Ni}^{3+}$  give rise to the pseudocapacitive behavior and the electrochemical reaction is given by the equation[36],



As shown in **Figure-7**, the porous  $\text{NP}_{20}$  film exhibits long-term cycle stability, maintaining 90% of its initial capacitance (from 142 to 129  $\text{F.g}^{-1}$ ) after 1000 charge/discharge cycles is significantly higher than those reported for NiO synthesized by direct and pulse potentiostatic methods [33]. The excellent electrochemical activity and ion kinetics of the synthesized film was illustrated with the well-defined sharp peaks at a high scan rate.

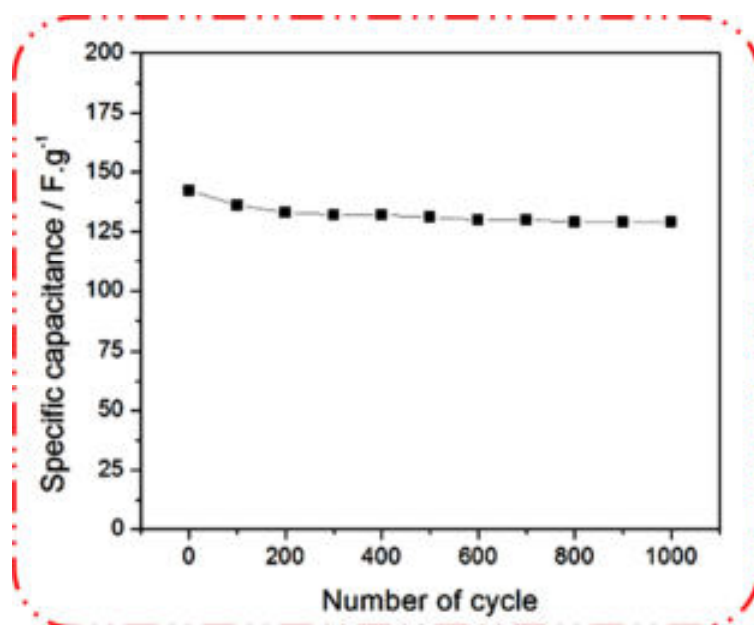


**Figure 7** Capacitance retention as a function of cycle number of  $\text{NP}_{20}$  sample at  $10 \text{ mV.s}^{-1}$  scan rate

#### CONCLUSION:

A very simple and low-cost chemical bath deposition approach has been successfully utilized to synthesize NiO thin films. This study has revealed the influence of different deposition times on the structural, morphological, and electrochemical properties of as-synthesized NiO films. SEM study shows that, as the deposition time increases, the thickness of the film increases, and simultaneously the width of the

cracks between the rose petals decreases, and thus the film becomes packed (or porosity decreases). The NP<sub>20</sub> film exhibited a specific capacitance of 142 F g<sup>-1</sup> which is 2.5 times higher than that of NP<sub>60</sub>, also it retains 90 % of its initial capacitance after 1000 charge/discharge cycles. Its superior specific capacitance and cycle stability, represent it as the best electrode material for supercapacitor applications.

## ACKNOWLEDGMENT

One of the authors Dr. Dhanaji S. Dalavi would like to thank DST-SERB, New Delhi for financial support through Major Research Project File No. EEQ/2021/000984.

## REFERENCES

- [1] H. Sun, J. Zhu, D. Baumann, L. Peng, Y. Xu, I. Shakir, Y. Huang, X. Duan, (2019), *Nat. Rev. Mater.* ,4 , 45–60.
- [2] D.S. Dalavi, R.S. Desai, P.S. Patil, (2022), *J. Mater. Chem. A.*, **10**, 1179-1226.
- [3] Q. Meng, K. Cai, Y. Chen, L. Chen, (2017), *Nano Energy*, 36, 268–285.
- [4] P. Simon, Y. Gogotsi, (2020), *Nat. Mater.*, 19, 1151–1163.
- [5] A. Singh, S.K. Gupta, A. Garg, (2017), *Sci. Reports* 2017 71. 7, 1–12.
- [6] S. Moon, N.M. Vuong, D. Lee, D. Kim, H. Lee, D. Kim, S.K. Hong, S.G. Yoon, (2016), *Sensors Actuators, B Chem.* 222, 166–172.
- [7] C.G. Granqvist, (2000), *Sol. Energy Mater. Sol. Cells.* 60, 201–262.
- [8] S. Sagadevan, A.R. Marlinda, M.R. Johan, A. Umar, H. Fouad, O.Y. Alothman, U. Khaled, M.S. Akhtar, M.M. Shahid, (2019), *J. Colloid Interface Sci.* 558, 68–77.
- [9] S.H. Choi, Y.N. Ko, J.K. Lee, Y.C. Kang, (2014), *Sci. Reports* 2014 41. 4, 1–7.
- [10] H. Liu, W. Zheng, X. Yan, B. Feng, (2008), *J. Alloys Compd.* 462, 356–361.
- [11] I. Hotovy, V. Rehacek, P. Siciliano, S. Capone, L. Spiess, (2002), *Elsevier*, 418, 9–15.
- [12] B.J. Rani, G. Ravi, R. Yuvakkumar, S. Ravichandran, F. Ameen, A. Al-Sabri, (2019), *J. Sol-Gel Sci. Technol.* 89, 500-510.
- [13] Z. Lin, C. Du, B. Yan, C. Wang, G. Yang, (2018), *Nat. Commun.* 9, 1–11.
- [14] A.C. Nkele, A.C. Nwanya, N.M. Shinde, S. Ezugwu, M. Maaza, J.S. Shaikh,

- F.I. Ezema, (2020), *Int. J. Energy Res.* 44, 9839–9863.
- [15] X. Liu, J. Wang, G. Yang, (2018), *Chem. Eng. J.* 347, 101–110.
- [16] U.M. Patil, R.R. Salunkhe, K. V. Gurav, C.D. Lokhande, (2008), *Appl. Surf. Sci.* 255, 2603–2607.
- [17] R.B. Patil, R.K. Puri, V. Puri, (2008), *J. Alloys Compd.* 462, 235–239.
- [18] P.K. Salokhe, S.S. Shetti, V.D. Patil, T.R. Patil, R.M. Nille, A.B. Chougale, K.T. Gurav, R.B. Sutar, A.A. Jatratar, G.G. Chougale, J.B. Yadav, B.M. Mohite, S.M. Bargir, R.B. Patil, S.H. Tamboli, (2021), *Today Proc.*, Elsevier Ltd., 43, 2810–2813.
- [19] C. Yuan, X. Zhang, L. Su, B. Gao, L. Shen, (2009), *J. Mater. Chem.* 19, 5772–5777.
- [20] Y. zhen Zheng, H. yang Ding, M. lin Zhang, (2009), *Mater. Res. Bull.* 44, 403–407.
- [21] X. Yan, X. Tong, J. Wang, C. Gong, M. Zhang, L. Liang, (2013), *Mater. Lett.* 95, 1–4.
- [22] M. Wu, J. Gao, S. Zhang, A. Chen, (2006), *J. Porous Mater.* 13, 407–412
- [23] M. Wu, J. Gao, S. Zhang, A. Chen, (2006), *J. Power Sources.* 159, 365–369.
- [24] B. Vidhyadharan, N.K.M. Zain, I.I. Misnon, R.A. Aziz, J. Ismail, M.M. Yusoff, R. Jose, (2014), *J. Alloys Compd.* 610, 143–150.
- [25] R.A. Patil, C.P. Chang, R.S. Devan, Y. Liou, Y.R. Ma, (2016), *ACS Appl. Mater. Interfaces.* 8, 9872–9880.
- [26] C.D. Lokhande, A.M. More, J.L. Gunjekar, (2009), *J. Alloys Compd.* 486, 570–580.
- [27] P.W. Chen, C. Te Chang, T.F. Ko, S.C. Hsu, K.D. Li, J.Y. Wu, (2020), *Sci. Reports* 10, 1–12.
- [28] Z. Wang, G.M. Kale, Q. Yuan, M. Ghadiri, (2012), *RSC Adv.* 2, 9993–9997.
- [29] D.S. Dalavi, M.J. Suryavanshi, D.S. Patil, S.S. Mali, A. V. Moholkar, S.S. Kalagi, S.A. Vanalkar, S.R. Kang, J.H. Kim, P.S. Patil, (2011), *Appl. Surf. Sci.* 257, 2647–2656.
- [30] S. Khalid, M.A. Malik, D.J. Lewis, P. Kevin, E. Ahmed, Y. Khan, P. O'Brien, (2015), *J. Mater. Chem. C.* 3, 12068–12076.
- [31] R.G. Sonkawade, I. V. Bagal, N.R. Chodankar, M.R. Waikar, P.S. Shinde, A.A. Shaikh, (2018), *J. Mater. Sci. Mater. Electron.* 29, 11151–11158.

- [32] M.R. Waikar, A.A. Shaikh, R.G. Sonkawade, (2019), *Vacuum*. 161 , 168–175.
- [33] Y. Ghalmi, F. Habelhames, A. Sayah, A. Bahloul, B. Nessark, M. Shalabi, J.M. Nunzi, (2019), *Ionics (Kiel)*. 25 , 6025–6033.
- [34] A. Šurca, B. Orel, B. Pihlar, P. Bukovec, (1996), *J. Electroanal. Chem.* 408 , 83–100.
- [35] Z. Lin, C. Du, B. Yan, C. Wang, G. Yang, (2018), *Nat. Commun.* 9, 4036.
- [36] Y. Chen, Y. Wang, P. Sun, P. Yang, L. Du, W. Mai, (2015), *J. Mater. Chem. A*. 3 (2015) 20614–20618.
- [37] G. Cai, X. Wang, M. Cui, P. Darmawan, J. Wang, A.L.S. Eh, P.S. (2015), *Nano Energy*. 12, 258–267.
- [38] S. Oswald, W. Brückner, (2004), *Surf. Interface Anal.* 36, 17–22.
- [39] Y. Wang, H. Xia, L. Lu, J. Lin, (2010), *ACS Nano*. 4 , 1425–1432.
- [40] X.H. Xia, J.P. Tu, J. Zhang, X.L. Wang, W.K. Zhang, H. Huang, (2008) *Electrochim. Acta*. 53 , 5721–5724.
- [41] S. Mishra, P. Yogi, S.K. Saxena, J. Jayabalan, P. Behera, P.R. Sagdeo, R. Kumar, (2017), *J. Mater. Chem. C*. 5 , 9611–9618.
- [42] A.I. Inamdar, Y. Kim, S.M. Pawar, J.H. Kim, H. Im, H. Kim, (2011), *J. Power Sources*. 196 , 2393–2397.
- [43] L. Zhu, C.K. Nuo Peh, T. Zhu, Y.F. Lim, G.W. Ho, (2017), *J. Mater. Chem. A*. 5,8343–8351.

# A Mini Review on Fe<sub>3</sub>O<sub>4</sub> for Microwave and Supercapacitor Application

Shital J. Shinde<sup>a</sup>, Satyashila D. Ghongade<sup>a</sup>, Pradnya G. Raje<sup>a</sup>, Azeem M. Bagwan<sup>a</sup>, Rajendra G. Sonkawade<sup>a, b\*</sup>

<sup>a</sup>Department of Physics, Shivaji University, Kolhapur, Maharashtra, 416 004, India

<sup>b</sup>SAIF-DST Center, Shivaji University, Kolhapur, Maharashtra, 416004, India

\*Corresponding author: rgs\_phy@unishivaji.ac.in

---

## ABSTRACT

*Iron oxide is a common material. The use of iron oxide-based nanoparticles in numerous disciplines has attracted a great deal of scientific attention. Due to its accessibility, adaptability, biocompatibility, biodegradability, and unique magnetic characteristics, magnetite has received significant attention. In order to produce high-quality products for the specified end applications, precise control over the nanoparticle manufacturing process is crucial. This is because the functionality of nano-scale magnetite is directly related to its form, size, and surface chemistry. Many chemical, physical, and biological techniques are used in laboratories and in industry today. These can be found in the literature. To achieve hitherto unheard-of synthesis results in terms of better-controlled morphologies, sizes, and size distribution, unconventional strategies have however arisen in recent years. Especially, microfluidic methods are a potential technology for overcoming some of the fundamental disadvantages of traditional bulk methods, such as lower reagent volume consumption, waste reduction, precise control of fluid mixing, and simplicity of automation. The major goals of this review are to present magnetite's features, uses, and synthesis processes as well as the most recent developments in this area.*

## KEYWORDS

*Fe<sub>3</sub>O<sub>4</sub>, Magnetic, Hydrothermal Synthesis, Microwave.*

.....

## 1. INTRODUCTION

The world is currently concerned about the fast-expanding use of fossil fuels and global warming, which has led to a focus on developing and promoting renewable energy. So, in order to meet the needs of our society and economy, highly efficient energy storage systems must be developed. Throughout the previous decade, a number of research projects were carried out to develop supercapacitor applications and energy storage [1, 2]. Many techniques, including micro emulsion, laser ablation, arc discharge, mechanical grinding, and high temperature breakdown of chemical precursors have been used to create magnetic nanoparticles. The need to manufacture

well-dispersed magnetic nanoparticles led to the development of a variety of techniques including co-precipitation, hydrothermal, the sol-gel method, electrodeposition, chemical bath deposition, and electro-spinning [3].

Despite the fact that there are various forms of iron oxides, the term "iron oxides" most frequently refers to three:  $\text{Fe}_2\text{O}_3$  (hematite),  $\text{Fe}_3\text{O}_4$  (magnetite), and  $\text{Fe}_2\text{O}_3$  (maghemite). Usually iron oxide nanoparticles, which are one of the most often employed compounds for various applications can be generated in three natural forms: hematite ( $\alpha\text{-Fe}_2\text{O}_3$ ), maghemite ( $\gamma\text{-Fe}_2\text{O}_3$ ), and magnetite ( $\text{Fe}_3\text{O}_4$ ) [1]. Hematite ( $\alpha\text{-Fe}_2\text{O}_3$ ), maghemite ( $\gamma\text{-Fe}_2\text{O}_3$ ), and magnetite ( $\text{Fe}_3\text{O}_4$ ) are the three main types used in industrial applications. Due to its exceptional magnetic characteristics,  $\text{Fe}_3\text{O}_4$  has garnered the most interest among all iron oxides.  $\text{Fe}_3\text{O}_4$  NP research has advanced significantly over the past 20 years, not only in the synthesis of homogeneous core magnetic  $\text{Fe}_3\text{O}_4$  NPs but also in the formation of advanced nanoarchitectures (core-shell, composites, functionalized surfaces, etc.) and the use of these nanomaterials in a variety of fields [4, 5]. The indirect charge transfer bandgap of hematite, an n-type semiconductor oxide with a more stable structural makeup was 1.9-2.0 eV. It has a weak magnetic field.  $\alpha\text{-Fe}_2\text{O}_3$  has demonstrated numerous significant uses at the nanoscale in fields such as photonics, gas sensors, Li-ion batteries, and water purification [6]. Ferromagnetic materials  $\gamma\text{-Fe}_2\text{O}_3$  and  $\text{Fe}_3\text{O}_4$  are widely employed in the biomedical sector and media recording industries respectively.

$\text{Fe}_3\text{O}_4$  is utilized in a variety of applications including microwave absorption, memristor, supercapacitor, glucose sensor, water splitting, and biomedical use.  $\text{Fe}_3\text{O}_4$  possesses higher magnetic saturation value than other metal oxide such as  $\text{Co}_3\text{O}_4$  [7–9], NiO [10–12],  $\text{TiO}_2$  [13–15]. Thus,  $\text{Fe}_3\text{O}_4$  became more prominent material than other metal oxide. Further  $\text{Fe}_3\text{O}_4$  has effective absorbing bandwidth and microwave absorption capabilities in the 2–18 GHz range. It has outstanding cole-cole interaction, permittivity, permeability, magnetic loss, and dielectric loss. Because of its high-power density, great reversibility, and cyclability, supercapacitors are widely used. This can be used for a variety of purposes including those requiring high power pulses, such as electric vehicles, burst power generation, memory backup systems, and others. Massive interest in the invention of novel electrode materials for cutting-edge energy storage technologies like batteries and electrochemical capacitors is driven by the rising demand for effective, long-lasting, safe, and sustainable energy sources.  $\text{Fe}_3\text{O}_4$  film produced hydrothermally was used as an electrode in supercapacitor applications. The  $\text{Fe}_3\text{O}_4$  film displayed a specific capacitance of 118.2  $\text{F g}^{-1}$  between 1 and 0.1 V at 6 mA current [16]. In this way, Author will discuss  $\text{Fe}_3\text{O}_4$  synthesis methods as well as microwave and supercapacitor application in this minireview.

## 2. MAGNETITE ( $\text{Fe}_3\text{O}_4$ )

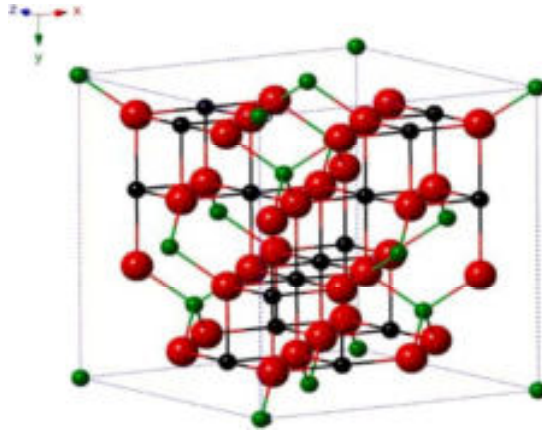


**Figure-1.** Crystal structure of magnetite. Green spheres –  $\text{Fe}^{3+}$ ; black spheres –  $\text{Fe}^{2+}$ ; red spheres –  $\text{O}^{2-}$  [17]

$\text{Fe}_3\text{O}_4$  is the chemical formula for magnetite. There are iron oxides in nature. It has an inverse spinel cubic crystal structure. Half-octahedral ferrous ion lattice sites, half-octahedral ferric ion lattice sites and all-tetrahedral lattice sites compose up the structure of magnetite [17]. Many characteristics of magnetite include electric and magnetic characteristics that are related to magnetic and dielectric loss. Magnetite exhibits superparamagnetism.

## 3. MAGNETITE SYNTHESIS TECHNIQUES

Magnetite can be prepared by several methods. Some of the methods are mentioned as follows.

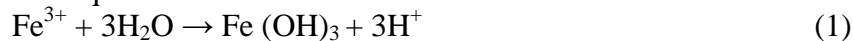
### 3.1 Chemical bath deposition method

Popular low temperature chemical methods include chemical bath deposition and chemical solution deposition. Chemical methods often require particle development and nucleation in two steps and solution growth in general. These techniques involve a number of factors, including deposition duration, solution pH, concentration molarity, temperature, substrate type, complexing agent, and Cation and Anion concentration. Furthermore, the several advantages of chemical bath deposition routes are 1) regulating growth factor 2) broad and consistent deposition 3) Ternary and quaternary compound deposition is discovered to be taking place. 4) doesn't require a complex instrument 5) CBD prevents substrate oxidation and corrosion. 6) It is inexpensive 7) The greater reaction time of the CBD technique results in good crystallite orientation [18].

### 3.2 Sol-gel Method

A simple and affordable approach to create perfect nanostructures with a vast surface area, great optical quality, purity, and homogeneity is the sol-gel process. There are two deposit processes used in the sol-gel procedures. Spin coating is followed by dip coating. Moreover, the sol-gel process parameters such as reaction temperature, reaction time, solvent, electrolyte composition, current density, and solution pH have an impact on obtaining the structure with the best possible electrochemical performance. The sol-gel process typically entails four steps: 1) creating the precursor solution, 2) creating the deposition products as sol, 3) converting from sol to gel, and 4) finally, applying thermal treatment. This sol-gel process has various benefits, including 1) generating high quality materials, 2) large area and high purity at reduced temperature. There are a few downsides to this environmentally friendly procedure, including 1) a lengthy processing time. 2) It still has adhesion issues. 3) The price of the raw materials 4) Large volume shrinkage and cracking are frequent during drying [19, 20]

A common wet chemical technique for producing metal oxides with nanoscale dimensions is called sol-gel synthesis. In sol-gel processing, the molecular precursor is hydroxylated and condensed to create a "sol" of nanometric particles [21]. The nano dispersed "sol" will continue to age, causing particles to expand and eventually form a three-dimensional metal oxide network known as "gel." To get the 'gel' to its final crystalline condition, more heating must be applied. Based on the chemical mechanism depicted in Eqs. (1) and (2), respectively,  $\text{Fe}^{3+}$  ions of the precursor are hydrolysed and condensed to produce  $\text{Fe}_3\text{O}_4$  nanoparticles.  $\text{Fe}^{3+}$  ions are easily hydrolysed and condensed to create ferrous hydroxides or oxides, according to the equation



Historically, the metal alkoxides of the desired metal oxides were used as the initial chemical solution or precursor for sol-gel synthesis. Metal alkoxides are highly resistant to hydrolysis and produce nanoparticles of metal oxides that are highly crystalline and homogeneous in size. Unfortunately, due to the intricate synthetic processes and the expensive and toxic usually employed chemicals, this alkoxides sol-gel synthesis approach is not suitable for large-scale and cost-effective manufacturing. Metal salts like chlorides, nitrates, and acetates are employed as the precursor in the subsequent sol-gel synthesis process in order to overcome the drawbacks of the alkoxides sol-gel synthesis method.

Sol-gel synthesis is the most recent synthetic method that is coupled. Pure  $\text{Fe}_3\text{O}_4$  nanoparticles have been produced by annealing in a vacuum. successfully

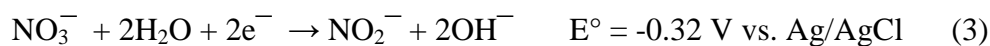
made utilizing affordable, nontoxic ferric nitrate and ethylene glycol serves as a precursor. Vacuum annealing is a further heat treatment applied to the nanoparticles that produces nanosized Fe<sub>3</sub>O<sub>4</sub> powders while preventing the oxidation of magnetite to iron (III) oxides like maghemite and hematite. The phases created and the particle volume percentage as well as the particle size distribution and dispersion, all have a significant impact on the magnetic ordering of Fe<sub>3</sub>O<sub>4</sub> nanoparticles produced via sol-gel synthesis. As a result many researchers are interested in the factors that affect the size distribution and dispersion of particles such as the precursor concentration used, the annealing period, and the temperature.

### 3.3 Electrodeposition

One of the most effective, non-vacuum based, and cost-effective processes is electrochemical deposition. The following elements including 1) temperature, affect the electrodeposition parameters, 2) The amount of current, 3) the period of deposition, 4) the solution's pH, 5) Crystallography, 6) The metal's nature, 7) contaminants in the solution, 8) electrolyte composition. There are two primary categories for the electrodeposition technique: Analogous Electrodeposition and cathodic Electrodeposition [22–24]. Moreover electrochemical atomic layer epitaxy and anodization are included in the cathodic deposition process. Pulsed potential, anodization, cathodic deposition, and the production of additional materials such carbonaceous material, metal, and metal oxide are the modes in which the deposition process takes place. The many benefits of electrodeposition include: 1) its rapid deposition rate and composition control, 2) It covers a huge area and doesn't require any vacuuming at all, 3) It requires little equipment, 4) It is a simple, scalable, pricey, and accurate procedure.

The growth mechanism of Fe<sub>3</sub>O<sub>4</sub> nanoparticles are explained as follows [25]. The Fe<sub>3</sub>O<sub>4</sub> (magnetite) formation can be explained by two step electrochemical-chemical (EC) mechanism, which includes:

The possible reduction reactions during the electrochemical phase are:



the product deposits on the cathode electrode when the pH of the solution rises close to the steel electrode surface due to an increase in the OH<sup>-</sup> content.

The chemical step:



Given the observed potential throughout the deposition process, which was -1.21 V vs Ag/AgCl at a current density of 2 A cm<sup>-2</sup>, it is widely acknowledged that the reduction of water (**Equation-4**) plays a significant part in the electro production of base (OH<sup>-</sup>) at the current conditions. In actuality, the electrochemical action was encouraged by the reduction of water molecules. Significantly, during the deposition process, gas bubbles were seen flowing over the cathode surface, further supporting the idea that OH<sup>-</sup> ions were produced by electrolysis of water. The OH<sup>-</sup> ions generated by the electrochemical step can react with the Fe<sup>3+</sup> and Fe<sup>2+</sup> cations in the chemical step. The chemical process leads to the deposit of Fe<sub>3</sub>O<sub>4</sub>.

### 3.4 Electrospinning

Modern effective ways for creating nanostructured materials include electrospinning. It is typically used to continuously and directly prepare polymer nanofibers with sizes ranging from submicron to nanoscale. Additionally, a variety of materials, including polymers, composites, and ceramics, have shown an interest in the electrospinning of nanofibers from polymer solutions for a number of possible uses. Many factors including viscosity, concentration molecular weight, deposition time, solution pH, and deposition rate have an impact on electrospinning. The electrospinning process has so far drawn more study attention in recent years due to a number of potential characteristics such as its high surface area, accessibility, special mechanical qualities, cheap production costs, high-voltage power supply, convenience, affordability, and environmental friendliness [26]. The method can also be applied to a variety of nanostructures including hollow and porous multilayers, hollow nanotubes, hollow nanowires, and core-shell nanostructures. In addition, a number of significant parameters including size distribution, morphologies, concentrations of metal precursors, types of polymers, metal precursors, and solution viscosities of the precursors might affect the preparation process. The electrode materials electrospinning technique produced electrodes with a large surface area, long cycle stability, and high capacitance.

### 3.5 Co-precipitation

The cost efficient and simple method is co-precipitation. In the co-precipitation approach, an alkaline solution combines with a stoichiometric mixture of ferrous and ferric precursors in aqueous solution to produce superparamagnetic nanoparticles as the iron source. The type of salts such as chlorides, sulphates, and nitrates, the Fe<sup>2+</sup>/Fe<sup>3+</sup> ratio, reaction temperature, the type of stabilising agent, pH level, and ionic strength of the reaction fluid all affect the size, shape, and composition of the magnetic nanoparticles. Nucleation and particle growth are both present and

competing in the coprecipitation process. Co-precipitation however, is commonly utilised since it has the potential to lead to industrialization [28].

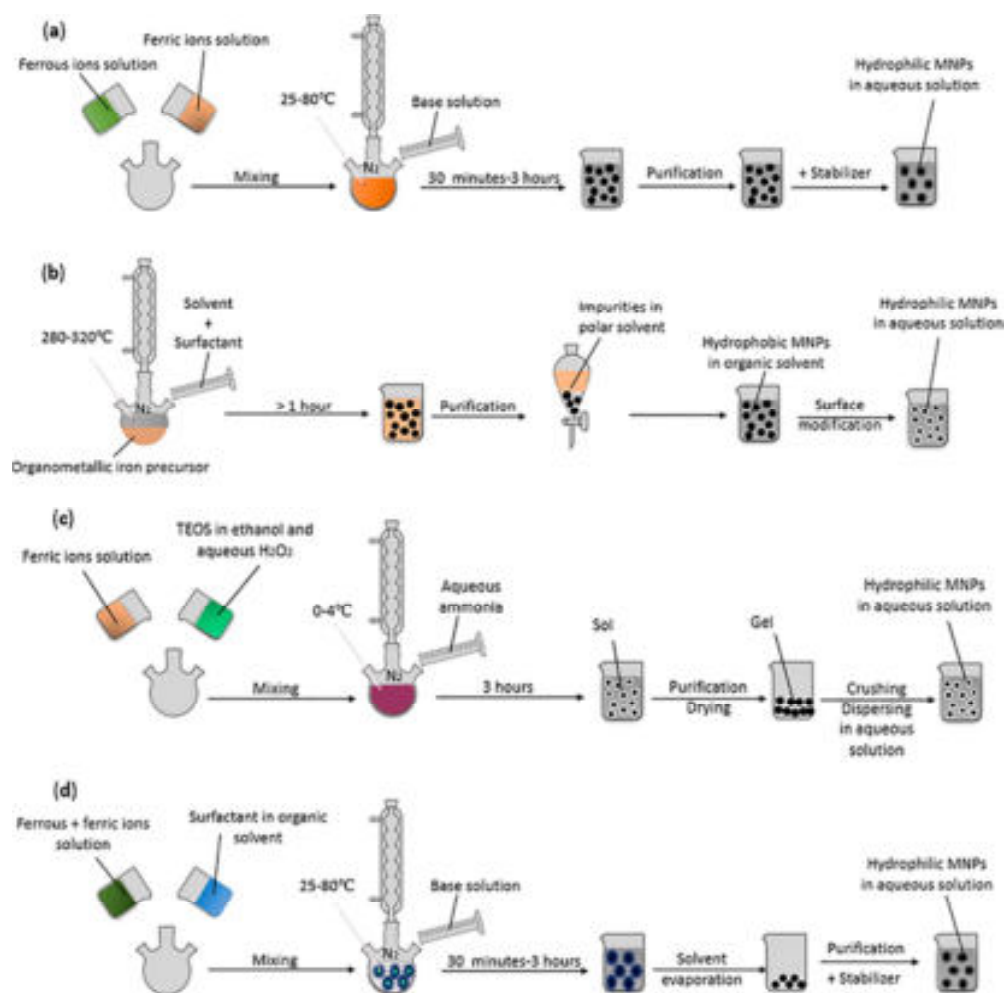


**Figure-2.** Schematic representation of commonly used chemical methods for MNPs synthesis. (a) co-precipitation; (b) thermal decomposition; (c) sol-gel; (d) microemulsion [27].

The usage of iron oxide nanoparticles (IONPs) in biomedicine, magnetic storage, water treatment, and catalysis is widespread. The co-precipitation method, which is applied in aqueous solutions containing ferric ( $\text{Fe}^{3+}$ ) and ferrous ( $\text{Fe}^{2+}$ ) salts as precursors and a base is added at moderate temperatures ( $100^\circ\text{C}$ ) has been the most widely utilised synthetic technique to date to create IONPs. Further Lagrow et

al. [29] explained growth mechanism of  $\text{Fe}_3\text{O}_4$  nanoparticles. Green rust is a form of iron hydroxide carbonate, or  $[\text{Fe}_6(\text{OH})_{12}\text{CO}_3]$ . Green rust is a mixed valent 2-dimensional structure that can be stabilised by a variety of counter ions, including  $\text{CO}_3^{2-}$ ,  $\text{SO}_4^{2-}$ ,  $\text{Cl}^-$ , and  $\text{Br}^-$  in either a hexagonal or rhombohedral crystal structure. It shares structural similarities with amorphous  $\text{Fe}(\text{OH})_2$  sheets.  $\text{Fe}^{3+}$  hydroxide tetrahedral centres are partially or completely incorporated into the framework through oxidation of  $\text{Fe}^{2+}$  hydroxide tetrahedra and incorporation. Author used TEM and Mössbauer to track the linear rise in ferrihydrite particle size over time, starting with initially generated 0.5 nm particles. When the particles are around 4 nm in size, researchers see a size-dependent transition between the ferrihydrite and the magnetite. In the X-ray diffraction pattern, this transition is marked by the absence of peaks from the iron hydroxide carbonate phase. The ferrihydrite phase disappears at 4 minutes, which is when the ferrihydrite phase is no longer visible by TEM. As the reaction develops, the iron hydroxide carbonate pattern becomes less intense. Before and after the creation of iron oxide, the amount of iron hydroxide carbonate decreases over time. The ions are integrated into the ferrihydrite, giving a supply of  $\text{Fe}^{2+/3+}$ , leading it to expand and transform into magnetite. This suggests that as the process advances, the iron hydroxide carbonate structure is re-dissolved. The ferrihydrite and later the magnetite slowly increases over time as a result of the iron hydroxide carbonate acting as a reservoir for  $\text{Fe}^{2+}$  and  $\text{Fe}^{3+}$  ions. Figure 3 depicts a schematic of this growth mechanism which deviates from traditional nucleation and growth ideas.

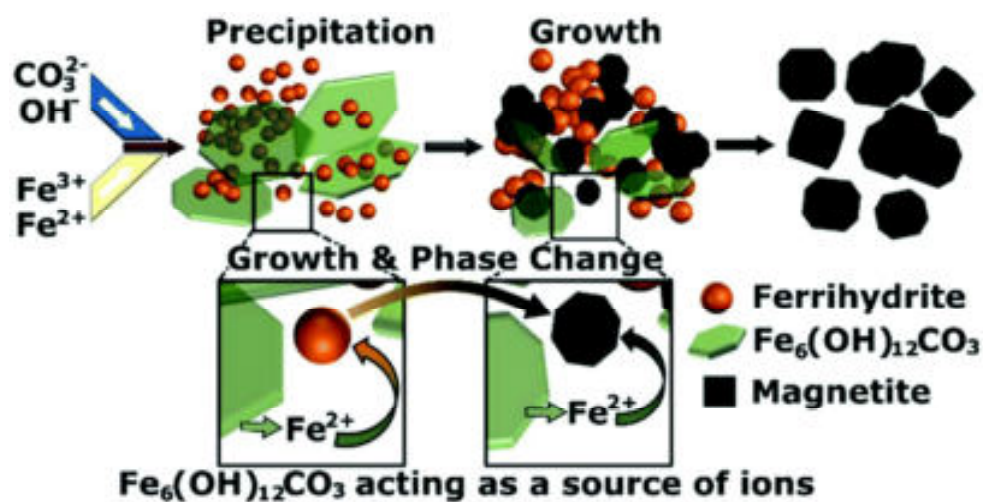


**Figure-3.** Diagram of the growth process demonstrating the initial precipitation of ferrihydrite and iron hydroxide carbonate ( $\text{Fe}_6(\text{OH})_{12}\text{CO}_3$ ) and the growth of

ferrihydrite through the re-dissolution of iron hydroxide carbonate to generate the magnetite phase [29].

### 3.6 Hydrothermal Method

Uniform magnetic nanoparticles are synthesized using the hydrothermal technique. In a hydrothermal reaction, iron precursors are dissolved in an aqueous solution under high pressure and high temperature. For hydrothermal reaction, a Teflon-sealed stainless-steel autoclave is utilized. The autoclaves water is in either a supercritical or sub-supercritical condition. The hydrolysis of the ferrous ions results in intermediate hydroxide products (Fe(OH)<sub>n</sub>), which are then converted to iron oxide by dehydration. High-crystalline, well-regulated particles can be produced through hydrothermal synthesis [30]. In order to manufacture magnetic nanoparticles, hydrothermal preparation is the most efficient way.

The growth mechanism of Fe<sub>3</sub>O<sub>4</sub> nanoparticles in this method as follows [31–34] Initially Fe<sup>2+</sup>, Fe<sup>3+</sup> and KOH precursors are dissolved in double distilled water. The reaction of this precursors are as follows:



The formation of Fe<sub>3</sub>O<sub>4</sub> as a pre-product at the beginning of the hydrothermal process (also known as the prehydrothermal process) can be attributed to these reactions (7) and (8). A portion of the Fe<sup>2+</sup> were oxidised to produce Fe<sup>3+</sup>, and this resulted in the creation of FeOOH, an intermediate product, as demonstrated in both reactions (9). Nevertheless, the process was carried out at high concentrations of KOH (pH > 12) and in the presence of pure oxygen (10). As a result of reaction (11) and both reactions (12) and (13), Fe<sub>3</sub>O<sub>4</sub> nanocrystals can develop in the hydrothermal process at high temperatures:



The pre-hydrothermal method produces the precipitate germs iron hydroxide and iron oxyhydroxide, which provide a favourable environment for the growth of Fe<sub>3</sub>O<sub>4</sub> nanocrystals.

## 4. Fe<sub>3</sub>O<sub>4</sub>: VARIOUS APPLICATIONS

Iron oxide may be a good choice for a variety of applications, due to its simple redox reaction, low price, simple production, and minimal environmental impact. Iron

oxide has a charge-storage capacity that can be increased by boosting the surface area that is actually active. Greater magnetic saturation and lower coercivity in magnetic nanoparticles lead to improved complex permeability. As a result, they have a large magnetic loss and are well-known microwave absorbers.

#### 4.1 Microwave application

Fe<sub>3</sub>O<sub>4</sub> exhibits exceptional performance at ultrafine dimensions and has a key role that cannot be easily substituted by any other magnetic material since it is highly stable, economical for a wide range of applications, and capable of fabricating complicated shapes. Iron-containing polycrystalline materials called ferrites which typically have a hard, brittle consistency and unique features are made of iron oxide and other metals like copper, nickel, and magnesium. Ferrite is useful in many electronic devices because of its magnetic and electric characteristics. Due to their extremely low eddy current loss, ferrite cores used in transformers, electromagnets, and inductors have high magnetic permeability and useful for antennas and electrical resistance.

A type of ferrite called Fe<sub>3</sub>O<sub>4</sub> has an anti-spinel structure and a Curie temperature of 585 °C. Since Fe<sub>3</sub>O<sub>4</sub> has an AB<sub>2</sub>O<sub>4</sub> structure, where Fe<sup>3+</sup> is located in the A position (a tetrahedral position), and Fe<sup>2+</sup> and Fe<sup>3+</sup> are both essentially disordered in the B site, electrons can move quickly between the two oxidation states of the iron. This has a significant impact on the dielectric loss of the iron oxide solids [35]. At high frequencies, Fe<sup>2+</sup> is also readily polarised and this polarisation can result in EM wave loss which has a certain additive influence on the absorption of EM radiation. Ji et al. [35] investigated electromagnetic wave absorption properties of Fe<sub>3</sub>O<sub>4</sub> nanoparticles. Ethylene glycol (MEG) was used as a reducing agent and DEG served as an additional reducing agent and surfactant during the hydrothermal preparation of Fe<sub>3</sub>O<sub>4</sub> nano-crystallines. The Fe<sub>3</sub>O<sub>4</sub> generated in the optimum solution (MEG 3.58 mol/l, DEG 2.10 mol/l) has a maximum reflection loss of -42 dB at 2.1 mm thickness and the largest reflection loss peak at 11.8 GHz. The microwave absorption band width is 3.2 GHz (9.5 GHz-12.7 GHz) and the reflection loss peak is smaller than -10 dB in these frequencies. The effective microwave absorption band width at 10 GHz is 3.9 GHz (7.29 GHz-11.2 GHz) when the thickness is 2.5 mm and the centre maximum reflection loss peak is -19 dB. In this way, Author reported Fe<sub>3</sub>O<sub>4</sub> nanoparticles excellent microwave absorption properties.

As a popular ferromagnetic EMW absorber, Fe<sub>3</sub>O<sub>4</sub> particle primarily relies on the synergistic effects of magnetic loss, particularly natural resonance, exchange resonance, and eddy current loss to absorb and attenuate incident EMWs. Shao et al. [36] reported microwave absorption properties of Fe<sub>3</sub>O<sub>4</sub> nanoparticles. In parallel the coercivity and saturation magnetization both enhanced. Vector network analysis was used to determine the permeability  $\mu_r$  and complex permittivity  $\epsilon_r$  of the Fe<sub>3</sub>O<sub>4</sub> and paraffin mixture. Using values of  $\epsilon_r$  and  $\mu_r$  and a model of a microwave absorbent

layer supported by a metal plate, the reflection loss at different sample thicknesses was calculated. With increasing thickness, the dip or least reflection loss changes to a lower frequency band. The minimum reflection loss of Fe<sub>3</sub>O<sub>4</sub> formed with a 6:1 molar ratio and paraffin wax composites reached -35.1 dB at 5.2 GHz and -30.2 dB at 17.6 GHz, respectively, when the thickness was 5 mm. Liang et al. [37] demonstrated Ball millings impact on the Fe<sub>3</sub>O<sub>4</sub> microwave absorption properties. Mechanical ball-milling was used to synthesize Fe<sub>3</sub>O<sub>4</sub> with various particle sizes by varying the milling period. The impact of milling time on Fe<sub>3</sub>O<sub>4</sub> structure, morphology, and electromagnetic parameters was investigated and the materials absorption characteristics and mechanism were examined for various milling times. The results showed that as the ball milling time increased, the integrity of the initial tiny spherical structure diminished. When the milling period was 2 hours, Fe<sub>3</sub>O<sub>4</sub> had excellent microwave absorptions and when the thickness was 6.55 mm, the maximum reflection loss was -21.19 dB at 4.64 GHz.

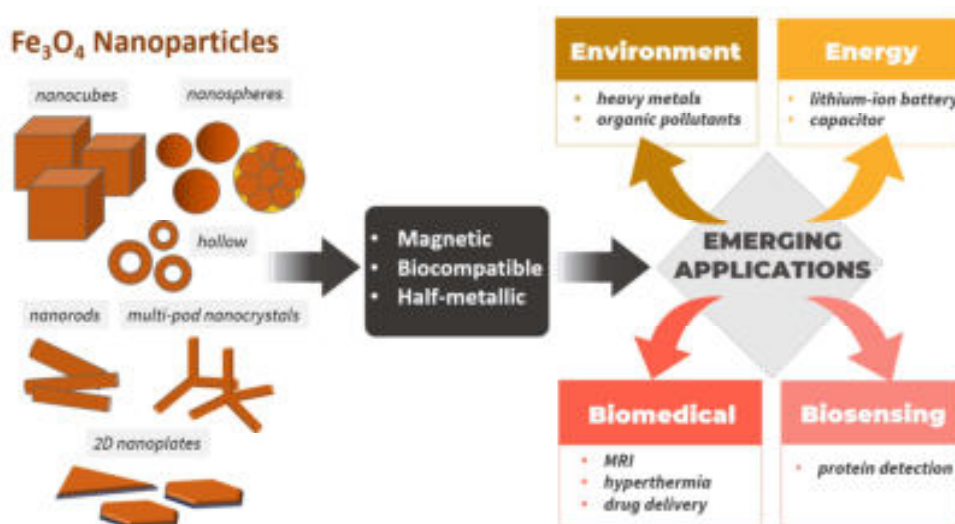


**Figure-4.** Fe<sub>3</sub>O<sub>4</sub> nanoparticles various applications with different nanostructure and size [23]

## 4.2 Supercapacitors

Supercapacitors often referred to as ultracapacitors or electrochemical capacitors, store electrical charges as electric energy on conducting materials. Due to their advantages such as their quick charge and discharge rates, long cycle lives, excellent energy densities, high power densities, self-operation, and environmental friendliness based on charge storage principles, supercapacitors have closed the gap between batteries and conventional capacitors. Electrical double-layer capacitors (EDLCs), pseudo capacitors (PCs), and hybrid capacitors (HCs) are the three types of

supercapacitors. At the junction of the electrode surface and the electrolyte ions, EDLCs store energy by electrostatic adsorption. Through the development of a second layer of electrolyte ions, EDLCs store energy on the surface of conducting electrodes. Hence EDLCs have very high discharge and charge rates and have lifetimes of over a million cycles. Although these SCs have low specific capacitance. Among EDLC components, carbon nanotubes, activated carbon, graphene oxide, graphene, nano-architecture carbon, and carbon aerogels are quite important. High-rate pseudo capacitors can provide greater power and energy densities as compared to EDLCs. The surface redox reactions of active materials which have more active sites are principally responsible for pseudo capacitance [38]. Supercapacitors (SCs) which have a higher power density than batteries and dielectric capacitors have attracted attention as the next-generation energy storage technology [39, 40]. SCs are divided into two classes: EDLC and PC, depending on the energy storage technique. Electric double-layer (EDLCs) and pseudo-capacitance are two different ways that SCs store charges [41]. The most prevalent and most researched type of SC is an EDLC, where the capacitance is caused by electrolyte ions adsorbing at the electrode-electrolyte interface. The surface properties of the materials such as their consequent surface area and pore architecture are what really determine the capacitance value for EDLCs. In EDLCs, during the charging process the anions and cations travel towards the positive and negative electrodes respectively which causes the electron flow in the external circuit to be induced in the opposite direction. The ions direction would be reversed throughout the discharge process. Because to their high specific surface area and excellent conductivity, carbon-based porous materials such activated carbon, xerogels, carbon nanotubes (CNTs), carbon nanofibers (CNFs), graphene, and carbide-derived carbons frequently exhibit EDLC-type behaviour. Because to its association with entirely non-Faradaic processes, the charge/discharge process in EDLCs reacts quickly to potential alterations. Whereas, Conway and Gileadi first used the term "pseudocapacitance" to refer to the electrochemical properties of materials that are connected to the surface coverage- and potential-dependent activation energy for electrolyte ion adsorption. The pseudocapacitive reactions which differ from EDLC in that they are of faradic origin store electrical energy at the electrode surface through quick and reversible electrochemical redox processes. In other words, pseudocapacitive materials reflect their electrochemical characteristics by exhibiting battery-like redox processes that occur at extremely high rates, akin to a capacitor (quasi-rectangular CVs and quasi-triangular GCD curves). In pseudocapacitive materials, the charge storage mechanisms can either involve i) redox reactions at or near the surface or ii) intercalation-type reactions

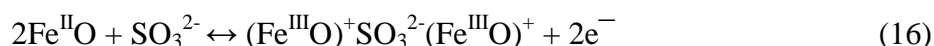
In this mini-review, Supercapacitor is the most demanding application in ongoing projects as we discuss  $\text{Fe}_3\text{O}_4$ 's numerous applications. There was an inverse spinel structure in magnetite ( $\text{Fe}_3\text{O}_4$ ).  $\text{Fe}_3\text{O}_4$  is a semiconductor material with a 0.1

eV band-gap. The electron (and hole) hopping between the  $\text{Fe}^{2+}$  and  $\text{Fe}^{3+}$  ions at the octahedral sites is the source of the conductivity of  $\text{Fe}_3\text{O}_4$  materials. In light of magnetite's known band-gap and octahedral site density, its carrier density which is equal to the product of the  $\text{Fe}^{2+}$  density and  $\exp(-0.1 \text{ eV}/2kT)$  is predicted to be no more than  $2 \times 10^{21} \text{ cm}^{-3}$ . Following the Mott-Schottky relation and assuming a dielectric constant of 7.0 for the compact  $\text{H}_2\text{O}$  film at the interface and a voltage of 1.0 V, a maximum space-charge capacitance at the magnetite side is calculated to be  $10 \mu\text{F cm}^{-2}$  of real surface. According to the Mott-Schottky relation, a maximum space-charge capacitance at the magnetite side is calculated to be  $10 \mu\text{F cm}^{-2}$  of actual surface, assuming a voltage of 1.0 V and a dielectric constant of 7.0 for the compact  $\text{H}_2\text{O}$  layer at the interface. As magnetite, which has a lower carrier concentration and lower conductivity is expected to be able to achieve this value which is similar to the experimentally determined capacitance of highly conductive Sb-doped  $\text{SnO}_2$ , it is anticipated that this value will serve as the upper limit. For instance, the magnetite particles utilised in the mixed electrode have a BET specific surface area of  $34 \text{ m}^2 \text{ g}^{-1}$ . As a result,  $3.4 \text{ F g}^{-1} \text{ Fe}_3\text{O}_4$  is calculated to be the specific capacitance. Its value is close to those in NaCl and  $\text{Na}_2\text{SO}_4$  but much smaller than those in the other electrolytes, especially in  $\text{Na}_2\text{SO}_3$ . Supercapacitors (SCs) are among the most promising energy storage technologies due to their high-power density, lengthy cycle lifetimes, and quick charge/discharge rates. SCs are widely desired in applications where large power densities are necessary such as peak power support and emergency power supply [42]. The electrochemical properties were calculated through working electrode. In order to generate the working electrode, 80 weight percentage of the iron oxide nanocrystals were combined with 10 weight percent of acetylene black and 10 weight percent of polyvinylidene difluoride (PVDF) in the presence of N-methyl pyrrolidinone (NMP). The components were combined, and the slurry was then applied on nickel foam [16]. The prepared electrode was vacuum-dried overnight at  $60 \text{ }^\circ\text{C}$ . The electrochemical tests were carried out in a typical three electrode cell with a working electrode made of manufactured  $\text{Fe}_3\text{O}_4$  nanocrystals on nickel foam and a reference electrode made of a saturated calomel electrode. The electrolyte was an aqueous solution containing 3 M KOH. Galvanostatic charge-discharge techniques and cyclic voltammetry (CV) were used to assess the performance of the supercapacitor. A Versastat 4-500 electrochemical workstation was used to conduct the electrochemical measurements. Aghazadeh et al. [42] investigated the electrochemical testing of cathodically produced ultra-fine magnetite nanoparticles capabilities as an electrode material for supercapacitor applications. Cyclic voltammetry (CV), continuous charge-discharge (GCD), and electrochemical impedance spectroscopy (EIS) techniques were used to assess the electrochemical performance of the prepared ultra-fine nanoparticles. By having a specific capacitance of up to  $195.8 \text{ F g}^{-1}$ , the produced  $\text{Fe}_3\text{O}_4$  nanoparticles were shown by the electrochemical data to have enough charge storage ability. After

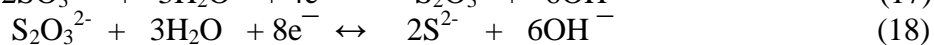
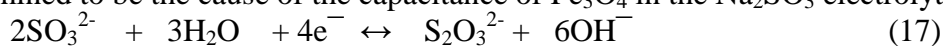
3000 cycles under a current load of  $0.5 \text{ A g}^{-1}$ , they still retain roughly 94% of their initial capacity. Further the charge storage mechanism of  $\text{Fe}_3\text{O}_4$  were explained by the author Nithya et al. [43]. For that several aqueous electrolytes including sodium sulphite (1 M  $\text{Na}_2\text{SO}_3$ ), sodium sulphate (1 M  $\text{Na}_2\text{SO}_4$ ), sodium chloride (1 M  $\text{NaCl}$ ), sodium phosphate (sat.  $\text{Na}_3\text{PO}_4$ ), and potassium hydroxide (1 M  $\text{KOH}$ ), were used to study the electrochemical performance of  $\text{Fe}_3\text{O}_4$ . A higher capacitance of  $510 \text{ F g}^{-1}$  with an operating potential of 1.2 V which was almost 5-7 times more than those of other electrolytes was offered by  $\text{Fe}_3\text{O}_4$  in the  $\text{Na}_2\text{SO}_3$  electrolyte. As a result, two pseudocapacitive mechanisms for  $\text{Fe}_3\text{O}_4$  in the  $\text{Na}_2\text{SO}_3$  electrolyte were demonstrated and are represented by



This results from the redox reaction of sulphur on its surface which produces sulphate and sulphite anions.



The oxidation/reduction reaction between Fe (II) and Fe (III) is described in Equation (16), with the potential intercalation of sulphite ions to counteract the additional charge in the iron oxide layers. According to the relationship between the rest potential and anion concentration, the electrochemical performance of  $\text{Fe}_3\text{O}_4$  in different electrolytes is discovered to be a potential determining process [44].  $\text{Fe}_3\text{O}_4$  is highly reactive to anion species in a variety of aqueous media but not to alkaline cations or electrolytes with a  $\text{pH} < 11$ . Later in 2006, the electrochemical quartz crystal microbalance and X-ray photoelectron spectroscopy were used to establish the capacitance mechanism of  $\text{Fe}_3\text{O}_4$  in  $\text{Na}_2\text{SO}_3$ ,  $\text{Na}_2\text{SO}_4$ , and  $\text{KOH}$  electrolytes. The specific capacitance of  $\text{Fe}_3\text{O}_4$  was 170, 25, and  $3 \text{ F g}^{-1}$  in 1 M  $\text{Na}_2\text{SO}_3$ ,  $\text{Na}_2\text{SO}_4$ , and  $\text{KOH}$  electrolytes respectively. The combination of the EDLC and pseudocapacitor which involves the reduction/oxidation of specifically adsorbed sulphite anions was determined to be the cause of the capacitance of  $\text{Fe}_3\text{O}_4$  in the  $\text{Na}_2\text{SO}_3$  electrolyte.



While double layer formation was responsible for the capacitive performance observed in the  $\text{Na}_2\text{SO}_4$  solution. The surface oxidation of the oxide electrode was responsible for a minor amount of capacitance in the  $\text{KOH}$  electrolyte.  $\text{Fe}_3\text{O}_4$  electrodes have so far been shown to have lower specific capacitances than expected and their low electronic conductivity has prevented them from reaching their high theoretical capacitance. Further, we can enhance  $\text{Fe}_3\text{O}_4$  electrochemical characteristics by combining with other materials.

## 5. CONCLUSION

Since the last two decades, there has been an increase in interest in the study, development and usage of magnetic nanoparticles for a variety of purposes including drug delivery systems, contrast agents, and hyperthermia therapy for the treatment of cancer. Magnetite is given particular attention since it is the most adaptable and readily available iron oxide type. Co-precipitation, solvothermal, ultrasonic irradiation, laser ablation, chemical reduction, and even plant-based processes are just a some of the techniques that can be used to produce it synthetically. However the transition from research to practical applications is typically hampered by such techniques high prices, slow response times, enormous amounts of waste, and utilisation of dangerous chemicals. In conclusion, unconventional magnetite synthesis techniques are still in the early stages of development but the early results are encouraging and motivate more research into increasing synthesis options and addressing pressing global issues. While more cost-effective strategies of recycling iron-based waste contaminants into magnetite nanostructures are anticipated, the methods currently under investigation may be scaled for industrial production.

## ACKNOWLEDGMENT

This research is supported by the PIFC, the physics department of Shivaji University in Kolhapur, and the DST-SAIF-CFC centre here at all. Author Pradnya G. Raje thanks BARTI for providing financial assistance for their research work.

## REFERENCES

1. Teja, A.S., Koh, P.Y. (2009) Progress in Crystal Growth and Characterization of Materials, 55, 22–45.
2. Mahmoud, W.E., Al-Ghamdi, A.A., Al-Agel, F. (2011) Polymers for Advanced Technologies, 22, 2055–2061.
3. Gu, W., Quan, B., Liang, X. (2019) ACS Sustainable Chemistry & Engineering, 7, 5543–5552.
4. Phan, M.H., Alonso, J., Khurshid, H. (2016) Nanomaterials, 6, <https://doi.org/10.3390/nano6110221>
5. Ce, Y., Jiajia, W., Yanglong, H. (2011) Chemical Communications, 47, 5130–5141.
6. Jayanthi, S.A., Nathan, D., Jayashainy, J., Sagayaraj, P. (2015) Materials Chemistry and Physics, 162, 316–325.
7. Liu, J., Liang, H., Zhang, Y. (2019) Composites Part B: Engineering, 176, 107240.
8. Li, Y., Li, S., Zhang, T. (2019) Journal of Alloys and Compounds, 792, 424–431.

9. Ai, L.H., Jiang, J. (2009) *Powder Technology*, 195, 11–14.
10. Karthik, K., Shashank, M., Revathi, V., Tatarchuk, T. (2018) *Molecular Crystals and Liquid Crystals*, 673, 70–80.
11. Liu, T., Pang, Y., Xie, X. (2016) *Journal of Alloys and Compounds*, 667, 287–296.
12. Liu, P., Ng, V. M. H., Yao, Z., Zhou, J., Lei, Y., Yang, Z., Kong, L. B. (2017) *ACS Applied Materials Interfaces*, 9(19), 16404-16416.
13. Xia, T., Zhang, C., Oyler, N. A., Chen, X. (2013) *Advanced Materials*, 25(47), 6905-6910.
14. Dong, J., Ullal, R., Han, J., Wei, S., Ouyang, X., Dong, J., Gao, W. (2015) *Journal of Materials Chemistry A*, 3(10), 5285-5288.
15. Wan, G., Yu, L., Peng, X., Wang, G., Huang, X., Zhao, H., Qin, Y. (2015) *RSC advances*, 5(94), 77443-77448.
16. Mitchell, E., Gupta, R. K., Mensah-Darkwa, K., Kumar, D., Ramasamy, K., Gupta, B. K., Kahol, P. (2014) *New Journal of Chemistry*, 38(9), 4344-4350.
17. Wu, W., Xiao, X., Zhang, S., Zhou, J., Fan, L., Ren, F., Jiang, C. (2010) *The Journal of Physical Chemistry C*, 114(39), 16092-16103.
18. Purbia, R., Paria, S. (2015) *Nanoscale*, 7(47), 19789-19873.
19. Khan, F., Khattak, N. S., Khan, U. S., Rahman, A. (2011) *Journal of the Chemical Society of Pakistan*, 33(6), 793.
20. Hu, P., Chang, T., Chen, W. J., Deng, J., Li, S. L., Zuo, Y. G., Volinsky, A. A. (2019) *Journal of Alloys and Compounds*, 773, 605-611.
21. Zhang X., Hao L., Wang H., (2017) *J Wuhan Univ Technol Mater Sci Ed*, 32, 42–46.
22. Wang, C. Y., Zhu, G. M., Chen, Z. Y., Lin, Z. G. (2002) *Materials research bulletin*, 37(15), 2525-2529.
23. Lim, J. H., Min, S. G., Malkinski, L., Wiley, J. B. (2014) *Nanoscale*, 6(10), 5289-5295.
24. Wang, C. Y., Zhu, G. M., Chen, Z. Y., Lin, Z. G. (2002) *Materials research bulletin*, 37(15), 2525-2529.
25. Karimzadeh, I., Dizaji, H. R., Aghazadeh, M. (2016) *Materials Research Express*, 3(9), 095022.
26. Li, Y., Ye, D., Li, M., Ma, M., Gu, N. (2018) *ChemPhysChem*, 19(16), 1965-1979.
27. Dadfar, S. M., Roemhild, K., Drude, N. I., von Stillfried, S., Knüchel, R., Kiessling, F., Lammers, T. (2019) *Advanced drug delivery reviews*, 138, 302-325.
28. Suppiah, D. D., Abd Hamid, S. B. (2016) *Journal of Magnetism and Magnetic Materials*, 414, 204-208.
29. LaGrow, A. P., Besenhard, M. O., Hodzic, A., Sergides, A., Bogart, L. K., Gavriilidis, A., Thanh, N. T. K. (2019) *Nanoscale*, 11(14), 6620-6628.

30. Mizutani, N., Iwasaki, T., Watano, S., Yanagida, T., Tanaka, H., Kawai, T. (2008) *Bulletin of Materials Science*, 31, 713-717.
31. Long, L. Q., Hue, T. T. B., Hoan, N. X., Cuong, L. V., Thang, P. D., Hoang, T., Truc, T. A. (2016) *Journal of Nanoscience and Nanotechnology*, 16(7), 7373-7379.
32. Gong, J., Li, S., Zhang, D., Zhang, X., Liu, C., Tong, Z. (2010) *Chemical Communications*, 46(20), 3514-3516.
33. Wu, W., Xiao, X., Zhang, S., Zhou, J., Fan, L., Ren, F., Jiang, C. (2010) *The Journal of Physical Chemistry C*, 114(39), 16092-16103.
34. Huang, J. H., Parab, H. J., Liu, R. S., Lai, T. C., Hsiao, M., Chen, C. H., Hwu, Y. K. (2008) *The Journal of Physical Chemistry C*, 112(40), 15684-15690.
35. Ji, J., Huang, Y., Yin, J., Zhao, X., Cheng, X., He, J., Liu, J. (2018) *The Journal of Physical Chemistry C*, 122(6), 3628-3637.
36. Shao, X., Dai, B., Zhang, X., Ma, Y. (2012) *Journal of nanoscience and nanotechnology*, 12(2), 1122-1127.
37. Liang, Y., Yuan, Y., Huang, Y., Wang, Y., Wei, S., Wang, B., Wang, X. (2020) *Materials*, 13(4), 883.
38. Chen, S., He, S., Hou, H. (2013) *Current Organic Chemistry*, 17(13), 1402-1410.
39. Chmiola, J., Yushin, G., Gogotsi, Y., Portet, C., Simon, P., Taberna, P. L. (2006) *science*, 313(5794), 1760-1763.
40. Tipsawat, P., Wongpratrat, U., Phumying, S., Chanlek, N., Chokprasombat, K., Maensiri, S. (2018) *Applied Surface Science*, 446, 287-292.
41. Chodankar, N. R., Pham, H. D., Nanjundan, A. K., Fernando, J. F., Jayaramulu, K., Golberg, D., Dubal, D. P. (2020) *Small*, 16(37), 2002806.
42. Aghazadeh, M., Karimzadeh, I., Ganjali, M. R. (2017) *Journal of Materials Science: Materials in Electronics*, 28, 13532-13539.
43. Nithya, V. D., Arul, N. S. (2016) *Journal of Materials Chemistry A*, 4(28), 10767-10778.
44. Zhan, H., Bian, Y., Yuan, Q., Ren, B., Hursthouse, A., Zhu, G. (2018) *Processes*, 6(4), 33.

# Supercapacitive Behavior of Cobalt Oxide Thin Films by Successive Ionic Layer Adsorption and Reaction Method

Gayatri R. Chodankar<sup>a</sup>, Suman A. Sawant<sup>a</sup>, Sunny R. Gurav<sup>a</sup>, Rajendra G. Sonkawade<sup>a\*</sup>

<sup>a</sup>Department of Physics, Shivaji University, Kolhapur 416004 (MS) India.

\*Corresponding author: rgs\_phy@unishivaji.ac.in

---

---

## ABSTRACT

*In this work, the Cobalt oxide electrode is made up of successive ionic layer adsorption and reaction (SILAR) method. Also, the effect of different SILAR cycles on supercapacitive properties was studied. CoO exhibits a single, stable phase with a cubic crystal structure and a porous, sheet-like morphology that is helpful for the intercalation of the electrolyte. The CoO electrode shows a maximum specific capacitance of 367 F/g measured in KOH electrolyte at a scan rate of 10 mV/s. Additionally, the CoO electrode has a power density of 133 W/kg and an energy density of 14 Wh/kg at 1 mA/cm<sup>2</sup> with 70.6% cyclic retention. Due to its hydrophilicity and porous agglomerated surface, CoO is a suitable electrode material for supercapacitor application.*

## KEYWORDS

*Aqueous Electrolyte, Chemical Method, Cobalt Oxide, Supercapacitive Properties, Thin Film*

.....

## 1. INTRODUCTION

Nowadays, nobody can even imagine a world without portable/wearable electronic devices, including laptops, mobiles, cameras, smartwatches, activity trackers, and many more, which have greatly changed our lifestyles and brought significant convenience to us. However, the increased demand for this smart electronic equipment requires superior energy storage devices [1]. Supercapacitors have been considered one of the potential energy storage systems [2]. Generally, they are classified based on their mode of energy storage mechanism, i.e., (i) the redox electrochemical capacitors and (ii) the electrochemical double-layer capacitors, respectively. In most cases, carbonaceous materials are used in the fabrication of supercapacitors due to their excellent cyclic stability and high specific capacitance. However, they suffer from poor specific energy density and limited cell voltage. These difficulties could be minimized with transition metal oxides, which play a major role in supercapacitor technology because of their good efficiency, long-term

performance, corrosion stability, and higher oxidation states [3]. Because of the higher transition and oxidation, there is a higher capacity for storing energy in them [4]. Metal oxides like ruthenium oxide ( $\text{RuO}_2$ ) [5], cobalt oxide ( $\text{CoO}$ ) [6], nickel oxide ( $\text{NiO}$ ) [7], and manganese oxide ( $\text{MnO}_2$ ) [8] have been reported as electrode materials in supercapacitors. Among these metal oxides, cobalt oxide/hydroxides are the most prominent electrode materials for supercapacitors owing to their attractive properties like high conductivity and good cyclic stability. According to a literature survey, it has been found that cobalt oxide electrodes have good efficiency and long-term performance. They have good corrosion stability, high specific area, low cost, and high reversible redox reactions.  $\text{Co}_3\text{O}_4$  and  $\text{CoO}_x$  are promising phases of cobalt oxide for supercapacitors due to their intercalative pseudocapacitance properties [9]. The cobalt oxide electrode has been found to have good efficiency and long-term performance, as well as good corrosion stability [10]. Hence, developing electroactive materials with high specific surface area, low cost, and high reversible redox reactions is an investigative object for electrochemists.  $\text{CoO}$  films have been synthesized by many different methods, including thermal oxidation, electrodeposition, dip coating, chemical vapour deposition, chemical bath deposition (CBD) and Successive Ionic Layer Adsorption and Reaction (SILAR) [11]. Each deposition method offers different advantages. Among these techniques, SILAR is a promising technique because it is simple, safe, environmentally friendly, suitable for mass production, low-temperature and cost-effective solution method [12].

In the present work, the electrochemical performance of  $\text{CoO}$  electrode for supercapacitors using a 1 M  $\text{KOH}$  electrolyte solution is investigated. The sheet-like  $\text{CoO}$  electrode is prepared by the cost-effective SILAR method, which is simple, convenient, and favourable for obtaining porous structured electrodes. The electrochemical performance of the supercapacitor is evaluated using cyclic voltammetry (CV), galvanostatic charge/discharge, and electrochemical impedance spectroscopy (EIS) techniques. The  $\text{CoO}$  electrode shows a maximum specific capacitance of 367 F/g in  $\text{KOH}$  electrolyte at a scan rate of 10 mV/s. With 133 W/kg power density at 1 mA/cm<sup>2</sup> and an energy density of 14 Wh/kg.

## **2. EXPERIMENTAL SECTION**

### **2.1. Materials**

Reagents Cobalt chloride ( $\text{CoCl}_2 \cdot \text{H}_2\text{O}$ ), Ammonia solution ( $\text{NH}_4\text{OH}$ ), and hydrogen peroxide ( $\text{H}_2\text{O}_2$ ) were bought from Thomas baker (AR grade) without including any chemical treatment.

### **2.2. Preparation of cobalt oxide (CoO) electrode**

The schematic representation of the  $\text{CoO}$  electrode deposited onto the stainless steel (SS) substrates is shown in **Figure-1**. The SS substrate is polished with fine-grade polish paper and washed with double-distilled water.  $\text{CoO}$  films were deposited from the cationic precursor of 0.1M  $\text{CoCl}_2$  complexed with liquid ammonia solution to make pH~12 and 0.4%  $\text{H}_2\text{O}_2$  as an anionic precursor. Double-distilled water (DDW)

is alternately placed in between the beakers containing cationic and anionic precursor solutions. Previously cleaned SS was immersed into the cationic solution of  $\text{CoCl}_2$  for 20s, where Co ions are absorbed on the substrate surface, then rinsed with DDW for 10s to remove loosely bound or excess cobalt ions from the substrate. Then the substrate was immersed in an anionic precursor (0.4%  $\text{H}_2\text{O}_2$ ) solution for 30s. Where the oxygen ions reacted with pre-adsorbed Co ions on the SS to form  $\text{CoO}$  electrode. Several SILAR cycles were repeated to get the final thickness of the  $\text{CoO}$ .

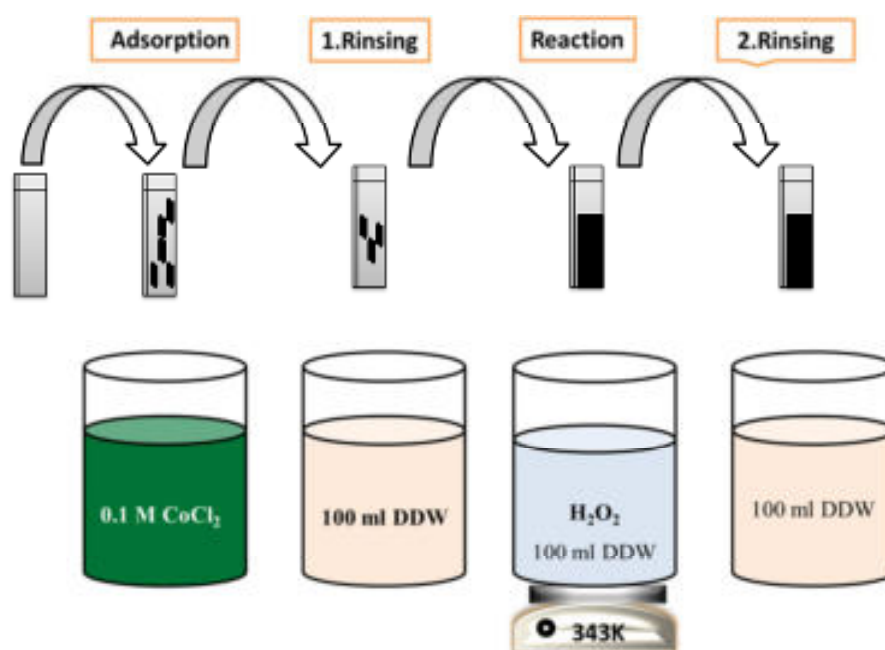


**Figure-1. Schematic of  $\text{CoO}$  electrode deposited by SILAR method.**

### 2.3. Characterizations

The Bruker AXS (Diffractometer D8) with  $\text{Cu-K}_\alpha$  radiation (wavelength 1.54 Å) X-ray diffraction (XRD) instrument was used to analyze the phase purity and crystallinity of the sample. ECO-ATR alpha instrument (ATR) adapted for detecting functional groups. Where JEOL-6360 Scanning Electron Microscope (SEM) is used for surface morphological analysis. The surface wettability was studied with contact angle (Rame-hart 500-F1) measurement and a CT meter used for thermal analysis measurement.

### 2.4. Electrochemical characterization

The electrochemical characteristics of the electrode were investigated using a traditional three-electrode system on electrochemical impedance spectroscopy (EIS) (Model: BioLogic vmp3 Potentiostat) utilizing synthesized  $\text{CoO}$  electrode as

working electrode (WE), platinum foil, and saturated calomel electrode as a counter electrode (CE), and reference electrode respectively.

### 3. RESULTS AND DISCUSSION

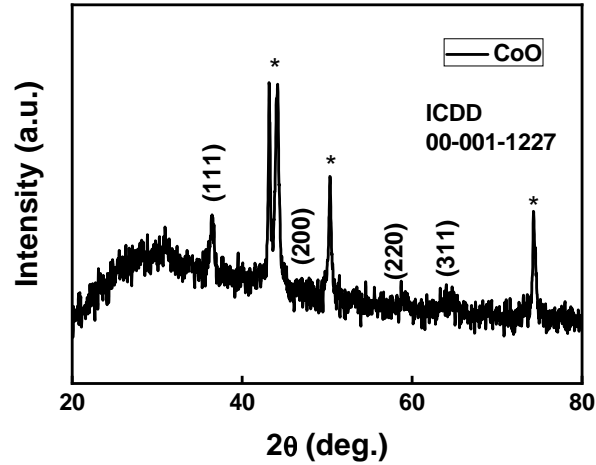


Figure-2. XRD pattern of CoO thin film.

The structural study of CoO thin films is carried out by the XRD. **Figure-2** shows the XRD patterns of CoO thin film. It is observed that the entire sample exhibits polycrystalline nature along with a crystalline phase. According to the *ICDD card, No. 00-001-1227* patterns belong to cubic crystal structure along with (111) plane at angle of 36.5° relatively. The peak of SS represented by \*.

The crystallite size was calculated by the X-ray line broadening method using Scherrer’s formula [13]. **Table-1** shows the values of crystalline parameters obtained from the XRD measurement,

$$D = \frac{0.9\lambda}{\beta \cos\theta} \quad (1)$$

**Table-1. Crystallographic parameters obtained from XRD measurement.**

SAMPLE	PLANES	β	2θ (°)	D (nm)
CoO	(111)	0.39	36.5	3.8

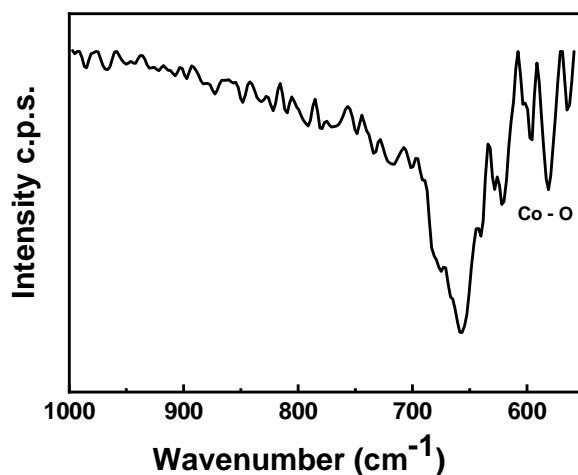


**Figure-3. FT-IR graph of CoO thin film.**

FT-IR spectroscopy is used for the identification of functional groups of CoO electrodes. As shown in **Figure-3**, the FT-IR spectrum of CoO is in the range of 3500-550 /cm. The peaks arising between 500-600 /cm are representative peaks that appear due to the metal-oxygen (Co-O) bonding [14]. The peak arises in the range of 1000 to 3500 due to the bending vibration of molecular water and OH-stretching vibration [15].

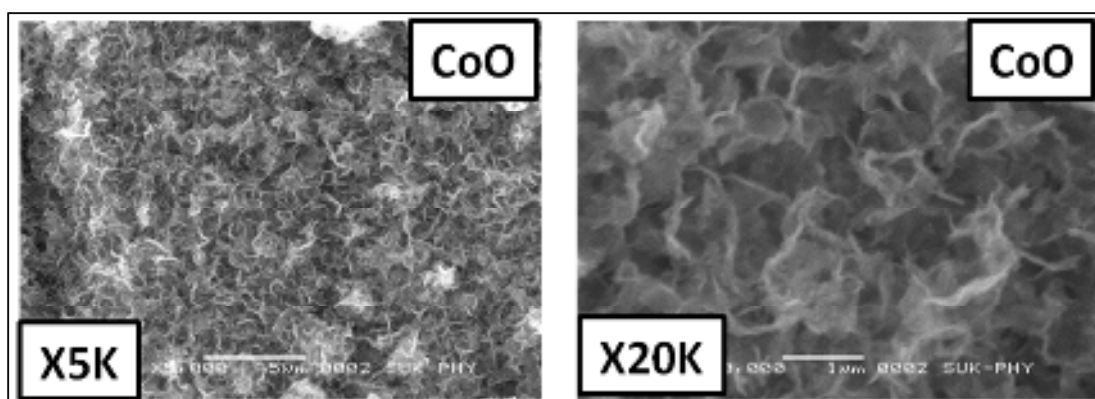


**Figure-4. SEM images of CoO thin films at 5K and 20K magnification.**

**Figure-4** shows the SEM of CoO, indicating agglomerate smooth sheet-like morphology and particles connected on the surface. In the case of a supercapacitor, the surface morphology of the active material of the electrode plays an important role in electrochemical reactions that occur near the surface of the electrode [16]. The film surface is well covered without any pinholes and cracks. Such a surface

morphology offers increased surface area, feasible for supercapacitor application [14]. The film surface is well-covered without any pinholes and cracks.

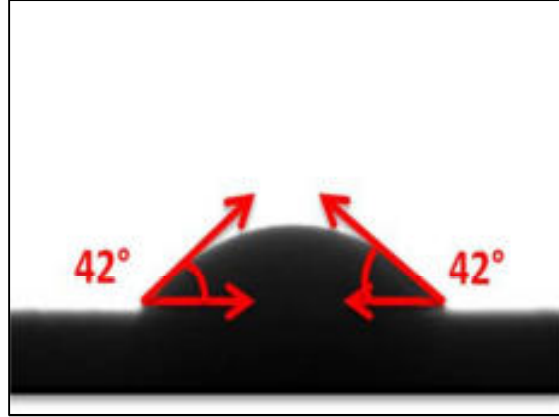


**Figure-5. Surface wettability test of CoO thin film.**

A wettability test is carried out to investigate the interaction between liquid and CoO thin film. If the wettability is high, the contact angle ( $\theta$ ), will be small and the surface is hydrophilic. On the contrary, if the wettability is low,  $\theta$  will be large and the surface is hydrophobic. A contact angle of  $0^\circ$  means complete wetting and a contact angle of  $180^\circ$  corresponds to complete non-wetting. Super-hydrophilic surfaces are important for supercapacitor applications. **Figure-5.** shows the water contact angle of the CoO electrode. The observed contact angle is  $42^\circ$  which is nearly hydrophilic in nature [17].

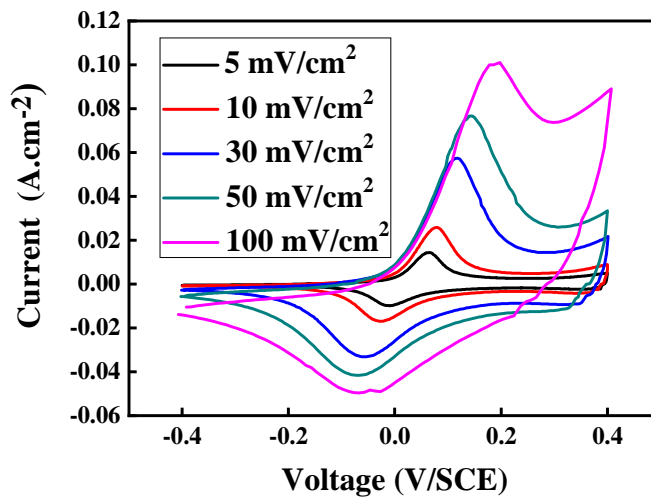


**Figure-6a. CV curves of different CoO thin electrode in 1 M KOH electrolyte.**

The electrochemical performance of SILAR-deposited CoO thin film was tested using the cyclic voltammetry (CV) technique. **Figure-6a.** shows CV of the CoO in the aqueous electrodes viz. 1M KOH electrolyte in the different scan rates. The area under the curve increases slowly with the scan rate. This shows that voltammetric current is directly proportional to the scan rate of CV.

The capacitance(C) of the CoO the electrode can be found by using the following relation [18],

$$C = \frac{\int Idt}{dv/dt} \quad (1)$$

Where ‘I’ is the average current in amperes, and ‘dv/dt’ is the voltage scan rate. The specific capacitance ( $C_s$ ) of electrode was obtained by dividing its respective weight using the relation,

$$C_s = \frac{C}{W} \quad (2)$$

Where ‘W’ is the weight of active material on the substrate. The interfacial capacitance ( $C_i$ ) was calculated using the relation,

$$C_i = \frac{C}{A} \quad (3)$$

Where ‘A’ is an area of active material dipped into the electrolyte.

**Table-2. Specific capacitance and interfacial capacitance of CoO electrode at 10 mV/s in 1M KOH electrolyte.**

Sample ID	Interfacial capacitance ( $C_i$ ) ( $F/cm^2$ )	Specific capacitance ( $F/g$ )
CoO	0.37	367

To avoid the oxidation and dissolution of a substrate during the measurement of capacitance by CV, the area of the working electrode was chosen to be  $1cm^2$ . The cyclic voltammograms of these films were conducted in 1 M KOH electrolyte in the voltage range of -0.4 to 0.4 V vs. SCE for CoO film. In this case, the KOH electrolyte exhibited symmetric CV characteristics in forward and reverse sweeps. Therefore, KOH was found to be a suitable electrolyte for CoO. **Table-2** shows the obtained result of the interfacial capacitance and the specific capacitance of CoO electrode. **Table-2** shows the obtained result of the interfacial capacitance and the specific capacitance of CoO electrode.

**Figure-6b.** shows the relation between specific capacitance and the scan rate of the electrode in 1 M KOH electrolyte. This shows the decrease in capacitance with an increasing scan rate. It has been attributed to the presence of inner active sites that

cannot sustain the redox transitions completely at higher scan rates. This is probably due to the diffusion effect of protons within the electrode [19]. The decreasing trend of the capacitance suggests that parts of the surface of the electrode are inaccessible at high charging–discharging rates [20]. **Table-3** shows the obtained results of CoO electrode with various scan rates.

The charge-discharge behavior of the CoO electrodes was studied by galvanometric charge-discharge method at different currents  $1 \text{ mA/cm}^2$ ,  $4 \text{ mA/cm}^2$ , and  $8 \text{ mA/cm}^2$  between  $-0.4$  to  $0.4 \text{ V}$  potential window depicted in **Figure-7**.

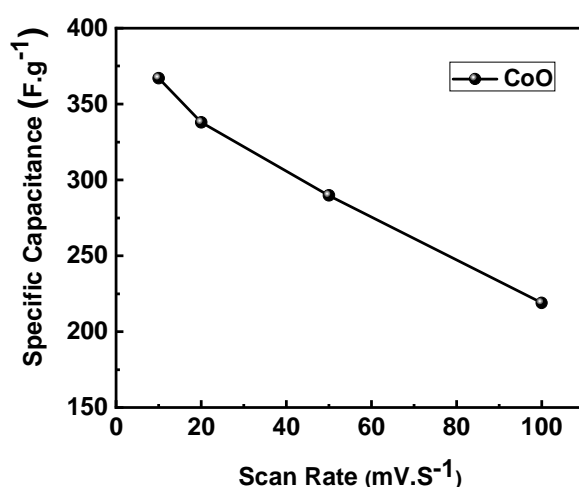


**Figure-6b. Specific capacitance with different scan rates.**

**Table-3. Specific capacitance at various scan rates of CoO thin film electrode in 1 M KOH electrolyte.**

Scan rate (mV/s)	Specific capacitance (F/g)
10	367.0
20	337.9
50	289.8
100	219.0

The discharge profile contains usually two parts, first, a resistive component arising from the sudden voltage drop due to the internal resistance and a capacitive component related to the voltage change due to a change in energy within the capacitor [21].

The electrical parameter such as specific power (SP) and specific energy (SE) was calculated using the following relations [22].

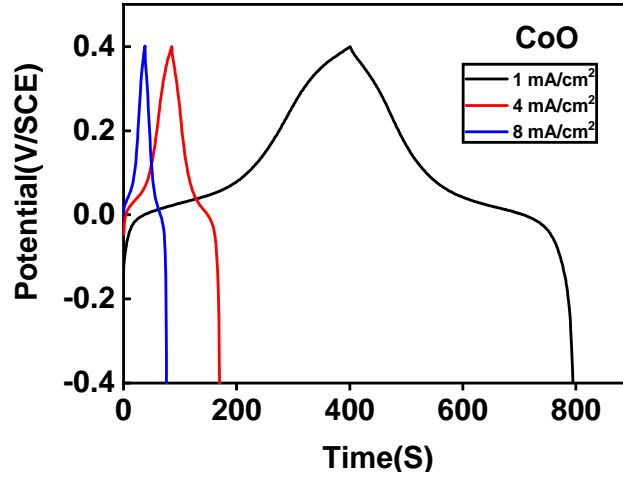


**Figure-7. The charge–discharge curve of cobalt oxide electrode in 1M KOH electrolyte.**

The electrical parameter such as specific power (SP) and specific energy (SE) was calculated using the following relations [22]

$$SP = \frac{I \times V}{m} \quad (4)$$

$$SE = \frac{I \times t \times V}{m} \quad (5)$$

Where, SP specific power is in kW/Kg and SE is specific energy in Wh/Kg. The above expressions show the discharge current (I) in amperes, voltage range (V) in volts, discharge time (t) in seconds, and mass of the electroactive material (m) in kilograms. The coulombic efficiency is calculated using the following equation [23],

$$\eta = \frac{t_d}{t_c} \times 100 \quad (6)$$

Where,  $t_c$  and  $t_d$  represent the time of charging and discharging, respectively.

**Table-4. The specific power (SP), specific energy (SE), and coulombic efficiency ( $\eta$ ) of CoO.**

Sample ID	I (mA/cm <sup>2</sup> )	Cs (F/g)	SE (Wh/Kg)	SP (kW/Kg)	$\eta$ (%)
CoO	1	164.6	14	133	98.7

	4	138.5	12	533	95.2
	8	133.2	11	1066	90.3

The value of specific capacitance ( $C_s$ ), specific power (SP), specific energy (SE), and coulombic efficiency are summarized in **Table-4**. The value of SE reduces and the value of SP increases with increasing current. The CoO electrode shows very good coulombic efficiency.

The charge transfer study of the CoO electrode was carried by EIS at frequency range of 0.1 Hz to 1 MHz. The EIS spectrum of CoO electrodes is shown in **Figure-8**. The equivalent solution resistance ( $R_s$ ) of the electrode/electrolyte interface is represented by the beginning of the semicircle in the high-frequency region, and the diameter of the semicircle in the low-frequency region is represented by the charge transfer resistance ( $R_{ct}$ ) of the electrode/electrolyte interface.

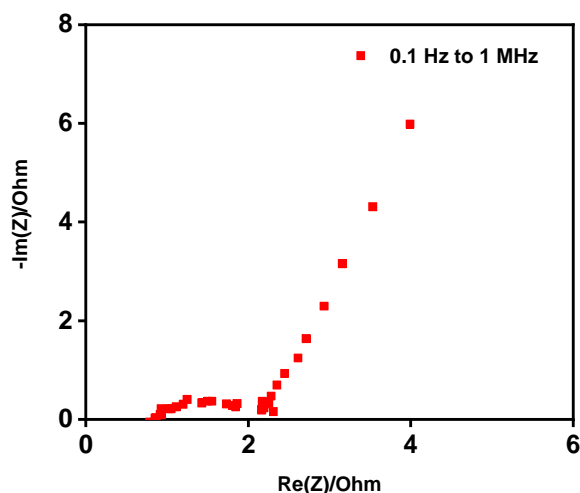


**Figure-8. The electrochemical impedance spectra of cobalt oxide electrode in 1M KOH electrolyte.**

The obtained values of  $R_s$  and  $R_{ct}$  for CoO electrode in KOH solutions is  $0.82 \Omega/\text{cm}^2$  &  $2.16 \Omega/\text{cm}^2$  respectively.

One of the key characteristics of the electrode is stability, which is necessary for a successful long-term energy storage system. In order to further verify the stability of CoO, GCD was done for 2500 cycles at a  $15 \text{ mA}/\text{cm}^2$ . **Figure-9** depicts the 1st and 2500<sup>th</sup> CD curves are stable. It can be seen that the 2500<sup>th</sup> CD's area is smaller than the 1<sup>st</sup> CD, suggesting electrode degradation into KOH. After 2500 cycles, it is estimated that 70.5% of capacity is still usable based on the area under the CD curve.

One of the key characteristics of the electrode is stability, which is necessary for a successful long-term energy storage system. To further verify the stability of CoO, GCD was done for 2500 cycles at a 15 mA/cm<sup>2</sup>.

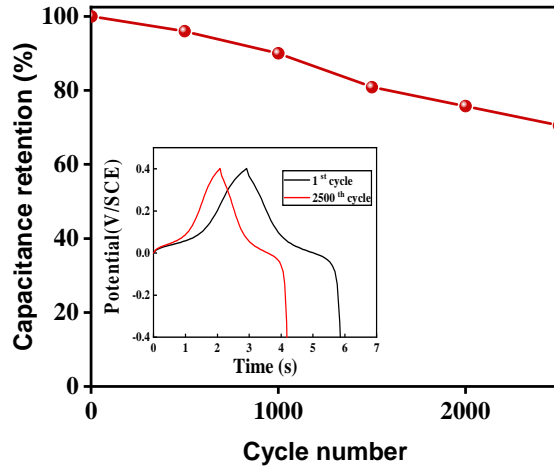


**Figure-9. The electrochemical stability of cobalt oxide electrode in 1M KOH electrolyte.**

**Figure-9** depicts the 1<sup>st</sup> and 2500<sup>th</sup> CD curves are stable. It can be seen that the 2500<sup>th</sup> CD's area is smaller than the 1<sup>st</sup> CD, suggesting electrode degradation into KOH. After 2500 cycles, it is estimated that 70.5% of capacity is still usable based on the area under the CD curve.

#### 4. CONCLUSION

It is concluded that Cobalt oxide film has been successfully deposited on the SS substrate and employed as a supercapacitor. The presence of characteristic bonds of cobalt oxide was confirmed by FT-IR studies. The sheet-like morphology of CoO offers more active sites for electrochemical reaction. The CoO electrode showed a maximum specific capacitance of 367 F/g at 10 mV/s. The energy density (E) and power density (P) were 133 W/kg, 14 Wh/kg, and columbic efficiency ( $\eta$  %) 98.7 % with 70.5% retention. CoO sheet-like electrode exhibits good performance at room temperature, which suggests potential application as an effective and high-performance supercapacitor.

#### ACKNOWLEDGMENT

The authors gratefully acknowledge Mahatma Jyotiba Phule Research Fellowship, Nagpur for providing funding through MJPRF and PIFC (Physics Instrumentation Facility Centre), Department of Physics for providing characterization facilities for

the present research work. Financial support provided by DST PURSE-Phase II (2018-2022), UGC DSA-Phase II (2018-2023), and UGC-DAE-CSR (2018-2021) is greatly appreciated.

## REFERENCES

1. Dubal, D.P., Chodankar, N.R., Kim, D.H., Gomez-Romero, P., (2018) *Chemical Society Review*, 47, 2065–2129.
2. Wang, Y., Song, Y., Xia, Y., (2016) *Chemical Society Review*, 45, 5925–5950.
3. Jagadale, A.D., Kumbhar, V.S., Dhawale, D.S., Lokhande, C.D., (2013) *Electrochimica Acta*, 98, 32–38.
4. Brousse, T., Bélanger, D., Chiba, K., (2017) *Springer Handbook of Electrochemical Energy*, edited by Brousse T. Springer, pp. 495–561.
5. Conway B.E. (1991) *Power Sources Symposium*, 138, 319–327.
6. Wang, T., Chen, H.C., Yu, F., Zhao, X.S., (2018) *Energy Storage Materials*, 6, 545-573
7. Jahromi, S.P., Pandikumar, A., Goh, B.T., (2015) *Royal society of chemistry advance*, 5, 14010-14019
8. Shaikh, A.A., Waikar, M.R., Sonkawade, R.G., (2019) *Journal of Electronic Materials*, 48, 8116–8128.
9. Uke, S.J., Akhare, V.P., Bambole, D.R., (2017) *Materials Science for Energy Technologies*, 4, 2–7.
10. Patil, V., Joshi, P., Chougule, M., Sen, S., (2012) *Soft Nanoscience Letters*, 02, 1–7.
11. Pawar, S.M., Pawar, B.S., Kim, J.H., (2011) *Current Applied Physics*, 11, 117–161.
12. Bayansal, F, Gülen, Y., (2015) *Journal of Alloys and Compounds journal*, 619, 378–382.
13. Najib, S. Emre, E., (2019) *Nanoscale advances*, 1, 2817-2827.
14. Kandalkar, S.G., Dhawale, D.S., Kim, C.K., Lokhande, C.D., (2010) *Synthetic Metals*, 160, 1299–1302.

15. Waikar, M.R., Rasal, A.S., Shinde, N.S., (2020) *Material Science in Semicondor Processing* 120, 105291.
16. Pal, B., Yang, S., Ramesh, S., (2019) *Nanoscale Advance*, 1, 3807–3835.
17. Vadiyar, M.M., Bhise, S.C., Patil, S.K., (2016) *Chemical Communications*, 52, 2557–2560.
18. Chodankar, N.R., Pham, H.D., Nanjundan, A.K., (2020) *Small*, 16, 1–35
19. Waikar, M.R., Shaikh, A.A., Sonkawade, R.G., (2019) *Polymer Bulletin*, 76, 4703–4718.
21. Espinoza, E.M., Clark, J.A., Soliman, J, (2019) *Journal of Electrochemical Society*, 166, H3175–H3187.
22. Shinde, S.K., Dubal, D.P., Ghodake, G.S., (2014) *J Electroanalytical Chemistry*, 732, 80–85.
23. Jadhav, P.R., Shinde, V.V., Navathe, G.J., (2013) *American Institute of physics Conference Processing*, 1536, 679–680.

# A Review on Flexible Ferrite Composite Based Gas Sensors

Azeem M. Bagwan<sup>a</sup>, Satyashila D. Ghongade<sup>a</sup>, Pradnya G. Raje<sup>a</sup>,  
Sheetal J. Shinde<sup>a</sup>, Rakesh K. Sonkar<sup>b</sup>, Rajendra G. Sonkawade<sup>a\*</sup>

a. Department of Physics, Shivaji University, Kolhapur 416 004 (MS) India.

b. Department of Physics, Acharya Narendra Dev College, University of Delhi, New Delhi 110019 India.

\*Corresponding author: rgs\_phy@unishivaji.ac.in

---

## ABSTRACT

*This review article includes a thorough discussion of Composite Ferrite gas sensors. It enables a thorough comparison of Composite Ferrite gas sensors with other gas sensors, particularly for the detection of Hazardous gases. The following section discusses many factors that can impact the responsiveness, selectivity, and stability of Composite Ferrite gas sensors. The changes in Composite Ferrite materials used for gas sensing caused by dopants or impurities are also discussed in this research. Conclusion: Dopants alter the geometry, topology, activation energy, electrical structure, or band structure of Ferrites to improve the characteristics of Ferrites for gas sensing applications. Dopants can sometimes produce oxygen vacancies or solid solutions, which lead to defects in Ferrites. These defects improve the gas detecting capabilities. In addition to nanopowders, several nanostructures have also been researched in this study. Examples of Composite Ferrites are provided in the conclusion to show how various Ferrite Composite materials may be used for gas sensing.*

## KEYWORDS

*Ferrite Materials, Ferrite Composites, Gas Sensing.*

## 1. INTRODUCTION

A few of the numerous diverse uses for which gas detection is becoming increasingly important including environmental protection, safety (sensing dangerous gases), managing fermentation in the food sector, diagnosing and monitoring patients, as well as household usage to detect flammable gases. The fluctuation of the material's electrical, acoustic, optical, mass, or calorimetric characteristics provides the basis for gas sensor detection. The most focus is being given to detection based on electrical property variations since it is easy, quick, and less expensive. As the need for sensors in smart devices for remote sensing increases, their portability and operating system compatibility are helping to accelerate the development of electrical detection-based sensors. Gas sensors with modified electrical properties primarily operate on changes in electrical resistance. Conducting polymers, single- or polycrystalline metal oxide semiconductors, and carbons are the basis of one of the most widely used gas sensors [1]. Among a

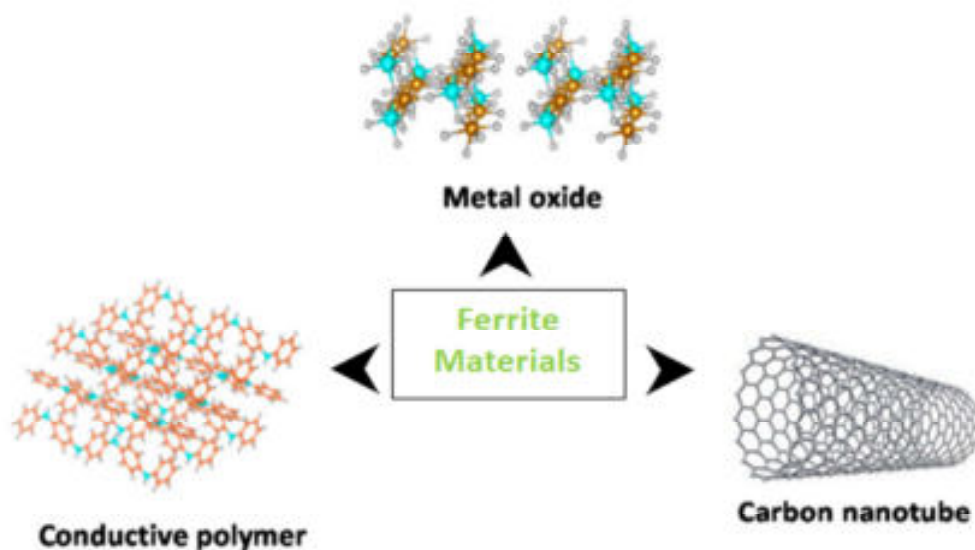


**Figure-1. Ferrite materials with different composites.**

variety of gas sensing materials, Metal oxide semiconductors (MOSs) are high performance sensors in terms of other materials because of their exceptional physical and chemical characteristics and distinctive structural design. Due to their broad band gap, these materials can exhibit the whole range of electronic characteristics. The material size usually has a significant impact on the MOSs' characteristics [2]. The ferrite-based compound is among the most researched and used materials in the nanomaterials area because of its exceptional qualities. Ferrite materials and the fabrication of ferrite gas sensing materials has been the subject of several investigations through. The high-temperature solid-state reaction approach, the sol-gel method, the co-precipitation method, the high-energy ball milling method, and the hydrothermal technique may all be used to synthesize ferrites in powder and thin/thick film formation [3][4]. Crystalline structure, optoelectronic, magnetic, and electrical conductivity qualities, as well as the flexibility to design heterojunction and doped systems, are the main characteristics of Ferrite composites. Because of its small particle size, presence of numerous surface active sites, strong adsorption capability, ease of separation, adjustable chemical composition, nonconductive nature, and high surface area to volume ratio, ferrite is one of the best possibilities for many composites. Spinel, garnets, hexagonal ferrites, and orthoferrites are the several types of ferrites that can be categorised based on their crystal structure. For gas sensing applications, spinel ferrites with the  $AB_2O_4$  composites are particularly promising complex oxides. **Figure-1** shows the Ferrite Materials with different Composites.

## 2. MOS-FERRITE COMPOSITE MATERIALS

MOS-Ferrite Composite sensors are generally based on tin oxide semiconductor change resistance in response to gases  $H_2S$  and other flammable gases are commonly measured with MOS-Ferrite sensors. MOS-Ferrite sensors are among the best sensors for  $H_2S$  gas monitoring when sensitivity to low concentrations (ppm range) is required. However,

non-specificity interferences present difficulties for the monitoring of flammable hydrocarbons [5]. According to reports, there are significant variances in performance amongst sensor manufacturers, with significant discrepancies frequently coming from a single company [6]. A MOS-Ferrite substance is applied on a non-conducting substrate in between two electrodes to form MOS-Ferrite sensors. The substrate is heated to a point where the monitored target gas can affect the MOS-Ferrite material's conductivity in a reversible manner. Without the target gas, oxygen atoms or other electron acceptors adsorb on the surface of the MOS-Ferrite material, trapping free electrons from the MOS-Ferrite conduction band. When introduced to gas with the oxygen atom that has been adsorbed, releasing the trapped electrons and lowering the material's resistance. Electrical measurements are used to determine this change in resistance, which is proportional to the gas concentration being assessed. The sensors can be doped or the operating temperature can be altered to affect the resistance of the sensor when particular gases react with the adsorbed oxygen in order to obtain some specificity. MOS-Ferrite sensors operate for a considerable amount of time (3-5 years). They are very sensitive to NO and CO, the majority of flammable gases. Fast reaction times, excellent mechanical strength, good stability, resistance to corrosive gases, and inexpensive cost of production are all characteristics of MOS-Ferrite sensors [7]. When an oxygen-containing material, such as  $\text{NiFe}_2\text{O}_4$ , is exposed to it, oxygen molecules adhere to the surface and get ionised into oxygen elements. By grabbing electrons near the  $\text{NiFe}_2\text{O}_4$  surfaces, ( $\text{O}^-$ ,  $\text{O}_2^-$  and  $\text{O}^{2-}$ ) is produced. In this method, particles were prohibited from accumulating additional free electrons by the building of a theoretically high barrier near to the  $\text{NiFe}_2\text{O}_4$  surface, while the sensor's resistance was decreased by the existence of a dense layer of holes

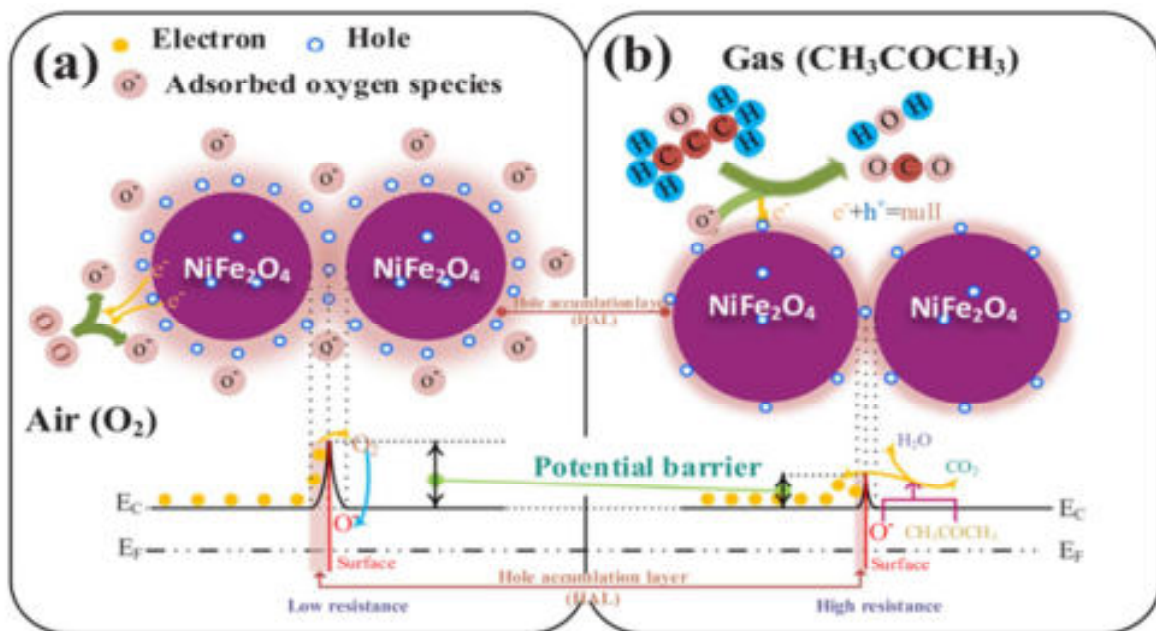


**Figure-2. Gas Sensing Mechanism of  $\text{NiFe}_2\text{O}_4$ . Adapted with Permission From. Copyright (2018) Elsevier**

accumulation close to the  $\text{NiFe}_2\text{O}_4$  surface. When exposed to a reducing gas, such as acetone, the reducing gas particles were oxidised with oxygen anions and the electrons

were injected back into the conduction band and mixed with holes. This increased the depth of the holes accumulation layer and decreased the level of the barrier layer, which is shown in **Figure-2** [8]. The capacity of ferrites to identify both reducing and oxidising gases has been thoroughly studied. Because ferrite can have its electrical properties fine-tuned, it is perfect for gas detection [5]. Additionally, ferrites include oxygen vacancies, which change the conduction properties and, consequently, the electrical response of the sensor. The primary advantage of ferrite over other single MOS sensor materials is its ability to alter the kind of conductivity and resistance value by modifying the position of the positive ions and their calcination state [9]. AgFeO<sub>2</sub> nanoparticles were synthesized by Wang et al. [10] using a straightforward hydrothermal method, and then they were exposed to gamma radiation. Gas detectors that can detect ethanol were created using pure and irradiated AgFeO<sub>2</sub> nanomaterial. In comparison to a pure AgFeO<sub>2</sub> nanoparticle-based detector, the gamma-irradiated AgFeO<sub>2</sub> nanomaterial sensor showed a greater response (S=36.8) and a lower optimal operating temperature (140°C). The irradiation AgFeO<sub>2</sub> nanomaterial sensor also has remarkable ethanol selectivity. By using a conventional molten-salt process, Khandekar et al. [11] created undoped and Ce doped CuFe<sub>2</sub>O<sub>4</sub> Nanocrystalline, which was subsequently effectively employed as a component of a reducing gas detector. Investigated were the effects of doped Ce on the structural, morphological, and gas response capabilities of copper ferrite. The size of the nanoparticles in the doped Ce composite was decreased. At a working temperature of 350°C, an undoped Ce sample at 2000 ppm had a 74% selective response to LPG. However, the sensitivity was raised to 86% after consuming cerium. Therefore, the current study investigated the potential applications of cerium-doped CuFe<sub>2</sub>O<sub>4</sub> pellets for LPG sensing.

Surface morphology plays a significant role in sensing response. The response qualities of porous composites can be significantly improved. MgFe<sub>2</sub>O<sub>4</sub> was developed by Godbole et al. [12] using a heating-free auto-combustion technique. The auto-combusted porous MgFe<sub>2</sub>O<sub>4</sub> composite has lower magnetization compared to other samples because more ions are concentrated in the octahedral locations. The auto-combusted MgFe<sub>2</sub>O<sub>4</sub> detector's sensitivity to alcohol vapours is boosted by small particle size, decreased magnetism from cation redistribution, and therefore greater catalytic activity of Mg<sup>2+</sup> ions. Due to the quicker rate of electron transport, the reaction with ethanol vapour is stronger than the one with methanol vapour. The sample's pores also helped with the quick adsorption and desorption of gases, which led to incredibly quick reaction and recovery times for alcohol vapours and increased the sensor's ability to detect gases.

### **3. CARBON-FERRITE COMPOSITE MATERIALS**

Carbon materials are excellent candidates for gas-sensing applications due to their intrinsic qualities, such as the nanoscale shape and the high surface area-to-volume ratio. MWCNTs are more desirable as sensors because they have stronger chemical resistance than single-walled carbon nanotubes (the property is important for surface-functioned). CNTs also have several drawbacks, including limited sensitivity and a slow recovery rate. Operating CNTs at high temperatures and adding metal (Au, Pt, Pd) or metal oxide NPs to them are two popular strategies to enhance their gas-sensing capabilities. In comparison to bare MWCNTs, Chen et al. developed SnO<sub>2</sub>/MWCNT hybrid structures

through physical vapour deposition that were more sensitive to gas-phase  $\text{NH}_3$  and  $\text{NO}_2$ . However, these nanocomposites' poor selectivity is a significant issue. Ferrites have played a key role in gas sensor technology over the past ten years because they exhibit greater selectivity and chemical stability than semiconductor oxides. The gas-sensing capabilities of spinel-type ferrites, an essential member of the ferrite family, have been studied. It has been discovered that by replacing the A-site or B-site ions in spinel-type ferrites with carbon materials, rare- earth and transition metal ions, the gas sensitivity can be adjusted.

Tang et al. [16] successfully fabricated ferrite/MWCNTs nanocomposites by using an in situ solvothermal method that directly deposited clusters of ferrite NPs onto the MWCNTs. The nanocomposites demonstrated a strong selectivity toward ammonia when evaluated against gas-phase ammonia, ethanol, methanol, toluene, benzene, and methanol. The hybrid structure of ferrite NPs dispersed on the surface of MWCNTs not only enhances the reaction area but also permits electron transfer between the NPs and the MWCNTs, which explains why nanocomposites exhibit increased sensitivity to ammonia vapours. Through a change in the electrical conductivity of the CNT component, the electronic interaction between the NPs and MWCNTs makes it easier to detect gas molecules. Negatively charged chemisorbed oxygen ( $\text{O}^{2-}$  or  $\text{O}^-$ ) is formed when oxygen forms oxygen adsorbates on the surface of ferrite nanoparticles (NPs) and carbon material captures electrons from the bulk of the nanocomposites. As a result, the nanocomposites electron density drops, increasing the material's resistance. The trapped electron is released to the conduction band and the resistance of the nanocomposite decreases when a reducing gas R, such as ammonia, is supplied.

In conclusion, two different gas sensing methods might be used with ferrite. NPs/CNT nanocomposites, 1) Target gas molecules like ammonia catalytically react with oxygen adsorbates to decompose into gaseous  $\text{NO}_2$  and water vapour, releasing electrons back to the nanocomposites surface and changing their surface properties. 2) Target gas molecules like ethanol directly adsorb onto the surface of the CNTs through hydrogen bonding. Here the nanocomposites gas-sensing abilities have been enhanced in comparison to bare MWCNTs and ferrite NPs. Also reduced graphene oxide (rGO)- $\text{CuFe}_2\text{O}_4$  nanocomposite was made by Achary et al. to monitor  $\text{NH}_3$  gas, and they discovered that the sensor could do so at low concentrations of 5 ppm at ambient temperature. In this rGO- $\text{CuFe}_2\text{O}_4$  composite sensing mechanism firstly, oxygen molecules from the air are initially adsorbed on the surface of the nanocomposite by trapping electrons from the material's conduction band. As a result, the concentration of vacancies grows, decreasing its resistance in the ambient air. The impedance spectra of the rGO- $\text{CuFe}_2\text{O}_4$  composite show a minor arc as a result of such a decrease in resistance. When analyte gas ( $\text{NH}_3$ ) comes into contact with the sensing material surface, chemisorbed oxygen molecules react with the analyte gas ( $\text{NH}_3$ ), supplying electrons to the sensing material's conduction band. As a result, the resistance rises and the charge carrier concentration (hole) drops. The resistance of the sensor returns to its initial condition as soon as the analyte gas ( $\text{NH}_3$ ) breaks the bond during the desorption process. Finally, rGO- $\text{CuFe}_2\text{O}_4$  nanocomposite exhibited increased activity and selectivity when compared to GO and  $\text{CuFe}_2\text{O}_4$  nanoparticles [17]. The gas sensing properties of Ferrite composites reported in literature is listed in **Table-1**.

**Table-1. Different composite Ferrite Materials based gas sensor.**

Sr. No.	Ferrite Composite Materials	Target Gas	Temperature (°C)	Concentration (ppm)	Sensitivity %	Ref.
1	CuFe <sub>2</sub> O <sub>4</sub>	Acetone	250	10	20.1	[13]
2	ZnFe <sub>2</sub> O <sub>4</sub>	Ethanol	300	100	29.1	[14]
3	NiFe <sub>2</sub> O <sub>4</sub>	LPG	25	2000	2.1	[15]
4	MWCNTs/Co-NiFe <sub>2</sub> O <sub>4</sub>	Ammonia	--	4000	6.2	[16]
5	rGO-CuFe <sub>2</sub> O <sub>4</sub>	Ammonia	25	200	25	[17]
6	$\alpha$ -Fe <sub>2</sub> O <sub>3</sub> -PANI	NO <sub>2</sub>	25	20	229	[18]
7	PANI/ CuFe <sub>2</sub> O <sub>4</sub>	Ammonia	25	5	4.7	[19]

#### 4. POLYMER-FERRITE COMPOSITE MATERIALS

Conducting polymers like polyaniline, polypyrrole, and polythiophene have received a lot of attention as potential chemical sensor materials. Polyaniline (PANI), one of the conducting polymers, is frequently employed due to its simplicity in synthesis, environmental stability, and inherent redox response. But these conducting polymers have a processing capability issue, a mechanical strength issue, and a chemical stability issue. Combining organic materials with their inorganic equivalents to develop composite materials is an excellent method for improving the mechanical strength and properties of sensors. Due to their potential for a variety of uses, heterogeneous conducting polymer nanocomposites, particularly organic-inorganic nanocomposites, have captured the interest of scientists in recent years. Conducting polymer/Ferrite nanocomposites are particularly difficult to make because they combine the flexibility and improved processability of polymers with the desirable modulus, transparency, surface hardness, and thermal resistance properties of Ferrite components. Ferrite nanoparticles represent a class of novel materials with promising applications in a wide range of areas [20]. In recent years, a variety of composites of polymers with Ferrite nanoparticles have been manufactured, and several research groups have also developed polymer/Ferrite nanocomposite sensors to provide materials with synergetic or complementary behaviour. Ferrite oxide-polyaniline ( $\alpha$ -Fe<sub>2</sub>O<sub>3</sub>-PANI) films were synthesized by Sonkar et al. [18]

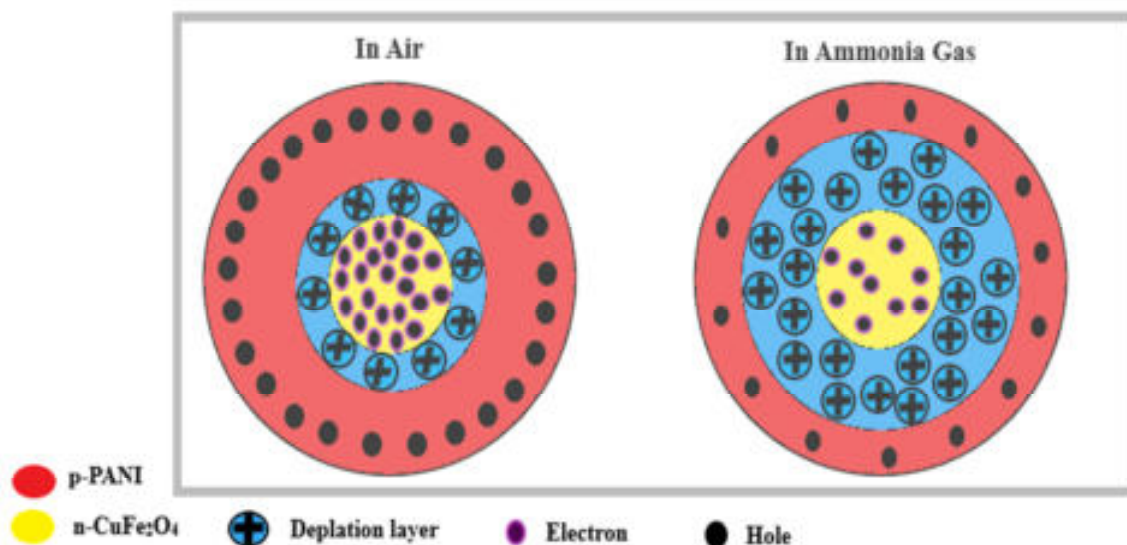


**Figure-3. Gas Sensing Mechanism of PANI/CuFe<sub>2</sub>O<sub>4</sub>.**

using the spin coating technique over Pt inter-digital electrodes on a variety of corning glass substrates. A ferric oxide-polyaniline composite thin film sensor structure with a sensitivity of  $2.29 \times 10^2$ , a moderate response time of 2.35 min, and a recovery time of 3.80 min has been developed for the trace level (20 ppm) sensing of NO<sub>2</sub> gas at ambient temperature. For achieving the improved response qualities, nanoporous spherical surface shape with nanocrystalline grains were discovered to be of great significance. In situ polymerization was used by Wang et al. to develop a Polyaniline/Copper Ferrite heterostructure, and the heterostructure was then coated on to substrate with staggered electrodes to create a high-performance NH<sub>3</sub> sensor. According to the mechanism, a p-n junction is formed when the p-type PANI nanocapsules are securely fastened to the n-type CuFe<sub>2</sub>O<sub>4</sub> nanospheres. In the depletion layer, the PANI/CuFe<sub>2</sub>O<sub>4</sub> heterojunction creates an electric field. When the sensor is exposed to NH<sub>3</sub> gas, the holes in CuFe<sub>2</sub>O<sub>4</sub> migrate in the opposite direction from the PANI electrons, which causes a drop in the depletion layer at the equilibrium point and a reduction in resistance. The ammonia concentration is converted to resistive variations in this process via the electrical sensitivity of the PANI/CuFe<sub>2</sub>O<sub>4</sub> p-n junction. As a result, it is simpler to detect ammonia gas at low concentrations using the PANI/CuFe<sub>2</sub>O<sub>4</sub> nanocomposite [19]. The concentration of PANI holes is reduced as a result of the adsorption of Ammonia as a reducing gas, and p-n junction depletion zones are expanded, as demonstrated in Fig.-3.

## 5. CONCLUSION

MOS, Carbon nanoparticles, and Polymers increase the sensitivity of Ferrite gas detectors. An analysis of the related literature shows that the preparative method, annealing temperature, concentration, and type of gas all influence the sensitivity, selectivity, operating temperature, and reaction time of ferrite gas sensors. It is discovered that composite ferrites have a higher gas response than pure ferrites. Doping reduces both the operating temperature and the reaction time. The creation of new materials that will allow for durable responsive and selective devices is the goal of ferrite composite gas sensors. In order to promote the use of various novel techniques for the development of novel sensor materials, there is a clear trend toward the search for new

Ferrite Composite nanostructures, such as nanobelts, nanowires, and nanorods. The future use of different Ferrite composites in biomedical devices such as biosensors, bioimaging, and gas sensors, electronic devices such as memory devices and semiconductor devices, magnetic recording, energy devices such as solar cells, electrocatalytic and photocatalytic based chemical storages, and many other fields is possible due to these properties.

### ACKNOWLEDGEMENT

Author Pradnya G. Raje would like to thank Dr. Babasaheb Ambedkar Research and Training Institute (BARTI), Pune, an autonomous Institute of Government of Maharashtra, for financial support under BARTI Fellowship. All Authors are thankful to UGC-DSA Phase II (2018-2023) and DST-PURSE Phase-II (2018-2023) Department of Physics, Shivaji University, Kolhapur (M.S.), India.

### REFERENCES

1. Šutka, A., Gross, K.A. (2016) *Sensors and Actuators B: Chemical* 222 95–105.
2. Wu, K., Li J., Zhang, C. (2019) *Ceramics International*. 45 11143–11157.
3. Singh, V.R., (2005) *Indian Journal of Pure and Applied Physics*. 43 7–16.
4. Dey, A., (2018) *Materials Science and Engineering B: Solid-State Materials for Advanced Technology* 229 206–217.
5. Kapse, V.D., Ghosh S.A., Raghuvanshi F.C., Kapse S.D., (2009) *Materials Chemistry and Physics* 113 638–644.
6. Gadkari, A.B., Shinde, T.J., Vasambekar, P.N., (2011) *IEEE Sensors Journal* 11 849–861.
7. Dalawai, S.P., Shinde, T.J, Gadkari, A.B., Vasambekar, P.N., (2015) *Journal of Materials Science: Materials in Electronics* 26 9016–9025.
8. Ma, Y., Lu, Y., Gou, H., Zhang, W., Yan, S., Xu, X., (2018) *Ceramics International*.. 44 2620–2625.
9. Kim, H., Pak, Y., Jeong, Y., Kim, W., Kim, J., Jung, G.Y., (2018) *Sensors and Actuators B: Chemical* 262 460–468.
10. Wang, X., Shi, Z., Yao, S., Liao, F., Ding, J., Shao, M., (2014) *Journal of Solid State Chemistry* 219 228–231.
11. Khandekar, M.S., Tarwal, N.L., Patil, J.Y., Shaikh, F.I., Mulla, I.S., Suryavanshi, S.S., (2013) *Ceramics International*. 39 5901–5907.
12. Godbole, R., Rao, P., Bhagwat, S., (2017) *Materials Research Express* 4 0–11.
13. Yang, X., Zhang, S., Yu, Q., Sun, P., Liu, F., Lu, H., Yan, X., Zhou, X., Liang, X., Gao, Y., Lu, G., (2018) *Sensors and Actuators B: Chemical* 270 538–544.
14. Cao, Y., Qin, H., Niu, X., Jia, D., (2016) *Ceramics International*. 42 10697–10703.
15. Singh, A., Singh, A., Singh, S., Tandon, P., Yadav, B.C., (2016) *Journal of Materials Science: Materials in Electronics* 27 8047–8054.
16. Tang, Y., Zhang, Q., Li, Y., Wang, H., (2012) *Sensors and Actuators B: Chemical* 169 229–234.
17. Achary, L.S.K., Kumar, A., Barik, B., Nayak, P.S., Tripathy, N., Kar, J.P., Dash, P., (2018) *Sensors and Actuators B: Chemical* 272 100–109.
18. Sonker, R.K., Yadav, B.C., (2017) *Journal of the Taiwan Institute of Chemical Engineers* 77 276–281.

19. Wang, X., Gong, L., Zhang, D., Fan, X., Jin, Y., Guo, L., (2020) Sensors and Actuators B: Chemical 322 128615.
20. Tai, H., Jiang, Y., Xie, G., Yu, J., Chen, X., (2007) Sensors and Actuators B: Chemical 125 644–650.

# Growth of grain like morphology of metals chalcogenide via successive ionic layer adsorption and reaction method

B. M. Patil<sup>a,b</sup>, V. L. Patil<sup>c,d</sup>, N. L. Tarwal<sup>c</sup>, S. R. Bhosale<sup>e</sup>, R. R. Bhosale<sup>f</sup>, P. D. Kamble<sup>g</sup>, P. S. Patil<sup>c\*</sup>, S. A. Vanalakar<sup>b\*</sup>

<sup>a</sup>Department of Physics, R. B. Madhkholkar Mahavidyalay, Chandgad, M. S. India

<sup>b</sup>Department of Physics, Karmaveer Hire Arts, Commerce, Science and Education College, Gargoti, Dist: Kolhapur-416 209, India

<sup>c</sup>Thin Film Materials Laboratory, Department of Physics, Shivaji University, Kolhapur-416 004, India

<sup>d</sup>School of Nanoscience and Biotechnology, Shivaji University Kolhapur, India-416004

<sup>e</sup>Medicinal Chemistry Research Laboratory, Department of Chemistry, Shivaji University Kolhapur, India-416004

<sup>f</sup>Analytical Chemistry and Material Science Research Laboratory, Department of Chemistry, Shivaji University Kolhapur, India-416004

<sup>g</sup>Department of Physics, The New College Kolhapur, India-41601

\*Corresponding author: sharad.vanalakar@gmail.com (S. A. Vanalakar)

---

## Abstract

*In this report, we have prepared the Cu<sub>2</sub>S, SnS<sub>2</sub> and ZnS thin films by a simple and cost effective successive ionic layer adsorption and reaction (SILAR) technique. Herein, we have reported the layer by layer deposition of metal chalcogenide on conducting substrate. The number of SILAR cycles was optimized to get uniform, good quality deposition of thin films. Meanwhile, the different physico-chemical characterization tools such as XRD, FT-Raman spectroscopy, UV- visible spectroscopy and SEM were used for the analysis of thin films. XRD study confirmed the development of crystalline forms of the thin films. The SEM analysis showed that the as synthesized Cu<sub>2</sub>S thin films were dense and homogeneous spherical in shape while ZnS thin film showed the porous film surface. The chemical composition and microstructures of material plays vital role in exotic applications based on metal chalcogenides.*

**KEYWORDS:** CZTS; Thin Films; SILAR; PEC

.....

## 1. INTRODUCTION

Today's rapidly developing nanomaterials worlds, Copper sulphide (CuS) is an important semiconductor material due to its excellent optical, electronic physical and chemical properties. Cu<sub>2</sub>S has potential applications in solar energy conversion, catalysis, and sensing. Cu<sub>2</sub>S facilitates various stoichiometric structural (5) phases and form stability at room temperature. The stable crystal forms like covellite (CuS), anilite (Cu<sub>1.75</sub>S), digenite (Cu<sub>1.8</sub>S), djurlite (Cu<sub>1.95</sub>S), and chalcocite (Cu<sub>2</sub>S) are present in copper sulphate [1]. Researchers have undertaken efforts to develop a facile synthesis strategy of copper sulphide at micro/nano level with modulated morphologies and architectures [2-5].

Similarly, Tin Sulfide (SnS<sub>2</sub>) is promising "alternative" material because of its indirect and direct band gap 1.0 eV and 1.3 eV, respectively [6, 7], and absorption coefficient exceeded upto 10<sup>4</sup>cm<sup>-1</sup> in visible range [8-9]. The solar cells fabricated using SnS<sub>2</sub> found to be 20% efficient as per simulation [10]. Also, it is revealed that the short circuit current will not pass higher than 30 mA/cm<sup>2</sup> [7]. Synthesized SnS<sub>2</sub> mostly form in orthorhombic nature which is ascribed to the space group of Pn-ma [11]. The unit cell of SnS<sub>2</sub> exhibits double layers of atoms stacked with a weak van der Waals force and shows coupling along the a-axis. The atomic bonding between Sn and S found covalent with Sn attached with 3 neighbors of sulphur [12]. The DFT simulation of SnS<sub>2</sub> advice the p-type nature of conductivity developed due to the Quick formation of Sn vacancies (V<sub>Sn</sub>), which finally act as shallow acceptors [13]. Few years back, thin film formation of nanostructured SnS<sub>2</sub> for the application of energy conversion has been reported. The preparation and utilization of SnS<sub>2</sub> have been carried out using physical as well as chemical deposition methods like evaporation, sputtering, chemical bath deposition (CBD), electrochemical deposition, spray pyrolysis method, and atomic layer deposition [14-20].

From vast research, it is found that tin interacts with sulphur atom to form numerous binaries such as orthorhombic form of SnS, trigonal form of SnS<sub>2</sub>, rhombic form Sn<sub>2</sub>S<sub>3</sub>, tetragonal forms of Sn<sub>3</sub>S<sub>4</sub> and Sn<sub>4</sub>S<sub>5</sub> [21]. Furthermore, these binary phases of crystallites affects adversely on the properties of SnS<sub>2</sub>. An inadequate change in elementary composition results to the enormous change in the type of conductivity [22]. Till date, the enormous work has been undertaken for SnS<sub>2</sub> based solar cells devices. The bottom neck numerous articles with wide range of deposition methods have been selected and listed in table.

**Table 1 show prominent results of SnS<sub>2</sub> based solar cell**

Sr. No.	Method	Buffer layer	Voc mV	Jsc mA/cm <sup>2</sup>	FF (%)	Efficiency (%)	Ref.
1	Spray Pyrolysis	CdS: In	260	9.6	53	1.3	[23]
2	Thermal Evaporation	CdS	208	17.9	38	1.6	[6]
3	RF Sputtering	Zn <sub>1-x</sub> Mg <sub>x</sub> O	..	..	..	2.1	[24]
4	Pulsed CVD	Zn (O,S)	..	..	..	2.9	[25]
5	Vaccum Evaporation	Zn (O,S)	..	..	..	3.8	[8]
6	ALD	Zn	..	..	..	4.3	[9]

Also, Zinc sulfide (ZnS) has numerous applications due to it's a wide band gap of 3.7 eV and consequent low absorption in the visible range. ZnS is widely used as filter and lens materials to UV photodiodes and other compound semiconducting devices [26–31]. ZnS nanostructured thin films can be developed with help of numerous synthetic methods namely chemical bath deposition (CBD), physical and chemical vapour deposition (PVD &CVD) [28-30, 32-33]. In this typical work, we

introduced a facile synthesis ZnS based thin films using SILAR method. The typical characterizations were carried out to study to evaluate the quality of ZnS thin films.

This work focuses the simplistic SILAR method for the synthesis of metal chalcogenides thin films. We have selected SILAR methods because of its possible advantages like (a) Large area device preparation through SILAR proves simplicity and economically cheaper. (b) The growth rate of the film prohibits thickness of deposition. (c) Doping and composition of various elements can be easily carried through this method. (d) Room temperature reaction can also be carried out. (e) Any kind of substrates can be used for the adsorption of ions. After successful deposition we have characterized these thin films by various characterization techniques. Also, to study the effect of layer by layer deposition of different metals chalcogenides on thin films. The obtained thin films were used for the different application and it is the promising metal chalcogenides for several purpose. The layer by layer deposition of metal chalcogenides via SILAR method and its impacts for solar cell application has been studied.

## **2. EXPERIMENTAL SECTION**

The Molybdenum Coated glass (Mo) substrates of size 26 mm X76 mm X 1 mm were used for the deposition of  $\text{Cu}_2\text{S}$ ,  $\text{SnS}_2$  and ZnS thin films. The Mo substrate was cleaned by reported method in our previous work. The substrates were washed with detergent for multiple times. Further the substrates were cleaned ultrasonically in ammonia solution.

All the chemicals were purchased from S. D. fine chemicals, Mumbai (India) and used without purification. The 0.02 M copper sulphate ( $\text{CuSO}_4$ ), 0.5 M Zinc sulphate ( $\text{ZnSO}_4$ ), 0.08 M Tin sulphate ( $\text{SnSO}_4$ ) were used as an anionic precursors and 0.16 M sodium sulphide ( $\text{Na}_2\text{S}$ ) was used as a cationic precursor for the deposition of  $\text{Cu}_2\text{S}$ , ZnS and  $\text{SnS}_2$  thin films, respectively. The films were deposited onto Mo conducting substrate. These films were developed using the Modified version of SILAR method. The repetition of a sequential deeping of Mo

substrate in the metallic (Cu, Zn and Sn) solutions were followed by Sulphur solution. The developed films were cleaned by 30 sec immersion time and kept for each solution respectively. This cycle is repeated up to 80 times. Developed films were cleaned in distilled water many times. Finally, the films were soft dried electric oven at 333 K. Then obtained this films were used for further characterization. The schematic representation of the preparation of the metal chalcogenides as shown in Fig. 1. Then, these samples were used for characterizations by different characterization techniques.

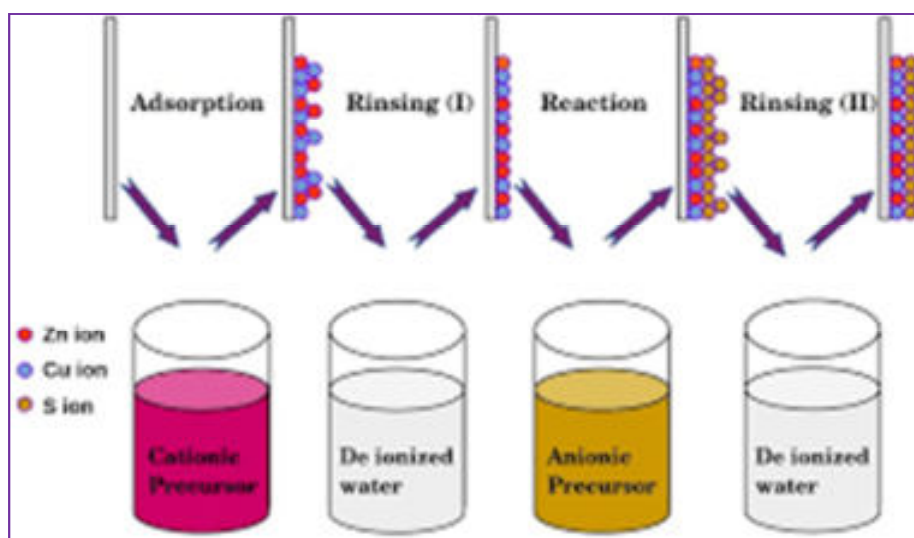


**Fig. 1. The schematic representation for the deposition of  $\text{Cu}_2\text{S}$  /  $\text{SnS}_2$ /  $\text{ZnS}$  thin films by SILAR method**

### 3. RESULTS AND DISCUSSION

Fig. 2 shows the XRD pattern of as-deposited  $\text{Cu}_2\text{S}$ ,  $\text{SnS}_2$  and  $\text{ZnS}$  thin films synthesized by SILAR method with constant deposition cycles. The peak intensities of  $\text{ZnS}$  and  $\text{Cu}_2\text{S}$  are lower than  $\text{SnS}_2$  peaks because of film thickness. The intensities of (021), (040), and (130) XRD peaks of  $\text{SnS}_2$  thin films can be seen in Fig. 2 and it is well match with standard JCPDS card no. 32-1361. On the basis of primary observations, we found no any diffractive reflections peaks of any other contaminant.

This confirms that engaged salts have been entirely transformed into the stable phases of  $\text{Cu}_2\text{S}$ ,  $\text{SnS}_2$  and  $\text{ZnS}$  metal chalcogenides.

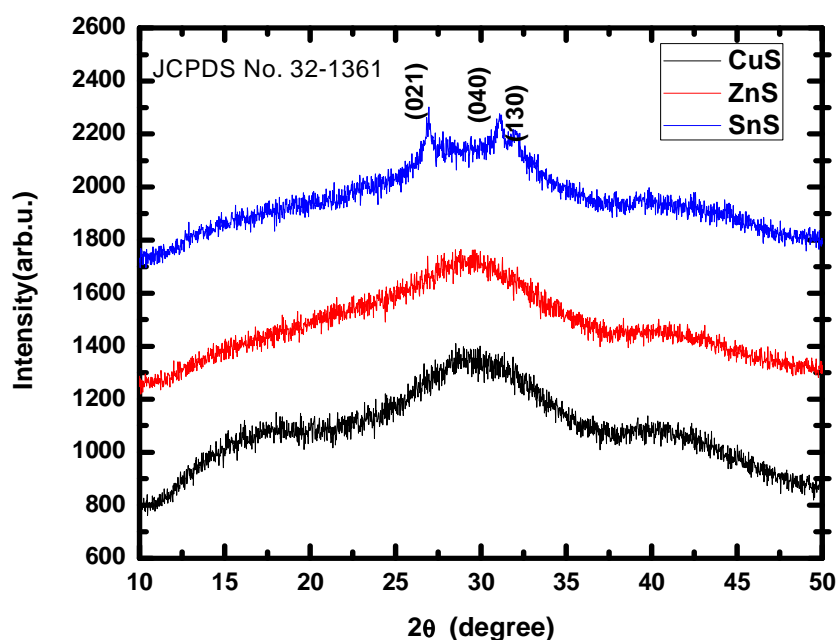


**Fig. 2 X –ray diffraction pattern of  $\text{Cu}_2\text{S}$ ,  $\text{ZnS}$  and  $\text{SnS}_2$  thin films**

The SEM micrographs of the  $\text{Cu}_2\text{S}$ ,  $\text{SnS}_2$  and  $\text{ZnS}$  thin films are shown in Fig. 3 (a, b, and c). The depositions of  $\text{Cu}_2\text{S}$  thin films were uniform and covered all over the substrate. The morphology of the  $\text{Cu}_2\text{S}$  thin films shows dense and homogeneous spherical grain shape morphology has been observed. The size of the grain was increased as increases the SILAR cycles. The size of the grains in the range from 0.3 to 0.8  $\mu\text{m}$ . This variation in the grain size is due to the different nucleation centres available for the films and agglomeration of the crystallites to lower the energy of the crystal. Fig. 3. b) shows the surface morphology of the  $\text{SnS}_2$  thin films. The obtained grain size in the range of 0.3 to 0.7  $\mu\text{m}$ . Meanwhile the film of  $\text{SnS}_2$  surface shows dense morphology with large grain size comparable to the  $\text{Cu}_2\text{S}$  thin films. Similarly, Fig. 3 c) shows the surface morphology of the  $\text{ZnS}$  thin

film deposited by SILAR technique. The film surface is relatively uniform having micro level grains present all over the film. The grain size varying from 0.2 to 0.4  $\mu\text{m}$ . Further the morphology of the films is uniform and no voids or cracks are observed on the films at micrometre range confirming suitability of the films for solar cell application.

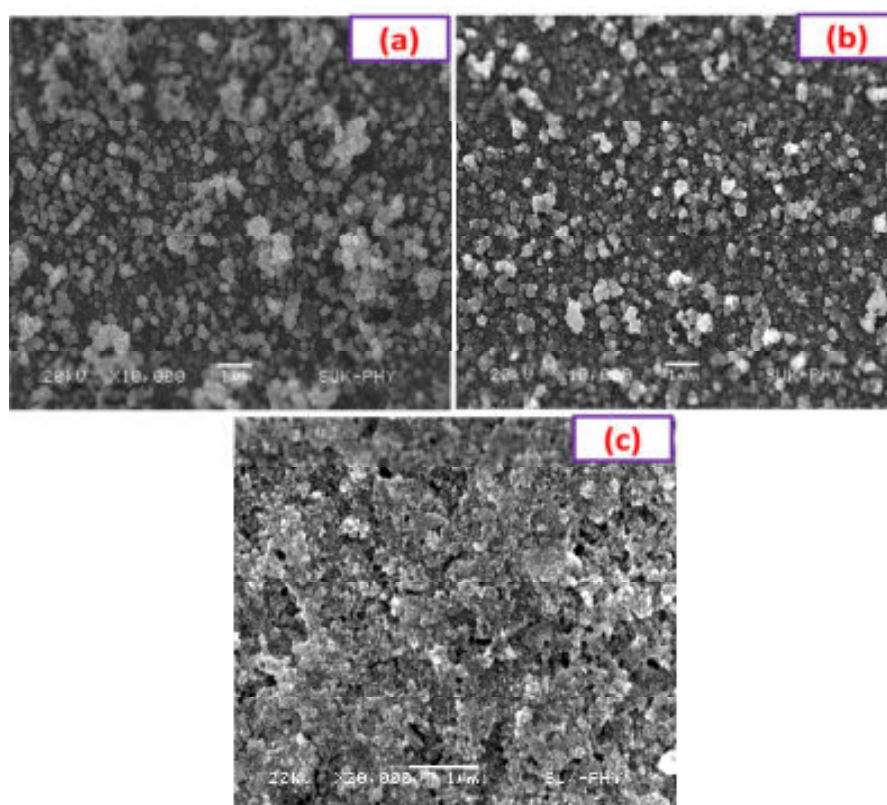


**Fig. 3 SEM images of (a)  $\text{Cu}_2\text{S}$  (b)  $\text{SnS}_2$  (c)  $\text{ZnS}$  thin films**

Fourier Transform Raman (FT-Raman) spectroscopy is used to examine the purity of the material and functional groups, present on the surface of the films. A typical FT-Raman spectra of a  $\text{Cu}_2\text{S}$ ,  $\text{SnS}_2$  and  $\text{ZnS}$  thin films is shown in Fig. 4. Positions of the peaks observed are in good agreement with those of  $\text{Cu}_2\text{S}$ ,  $\text{SnS}_2$  and  $\text{ZnS}$  films reported earlier in literature.

Fig. 4 (a) is FT-Raman spectra of  $\text{Cu}_2\text{S}$  thin film which shows the pronounced peak at  $272\text{ cm}^{-1}$  belongs to the vibration of the Cu-S bond and that observed at  $472\text{ cm}^{-1}$  which are attributed to the stretching vibrations of the S-S bond. The intensity of the Cu-S peak is greater than that of S-S bond confirming formation of Cu-S and also indicates absence or lesser presence of unreacted sulphur in CuS. Fig. 4 (b) shows the FT-Raman spectrum of typical  $\text{SnS}_2$  film. The presence of three characteristic peaks located at  $170\text{ cm}^{-1}$ ,  $192\text{ cm}^{-1}$  and at  $219\text{ cm}^{-1}$  suggests  $\text{SnS}_2$  phase [38]. These peak positions well agree with the earlier reports confirming the formation of  $\text{SnS}_2$  film [39]. The most intense peak is observed at  $192\text{ cm}^{-1}$  assigned to the asymmetric stretching of Sn-S bond [39]. The Raman peaks observed at  $170\text{ cm}^{-1}$  and at  $219\text{ cm}^{-1}$  belongs to lattice vibrations attributed to the symmetric stretching of Sn-S bond. Low intense peak at  $307\text{ cm}^{-1}$  is due to the presence of secondary phase  $\text{Sn}_2\text{S}_3$  which is observed in Fig. 4 (b). In addition absence of other peak at  $312\text{ cm}^{-1}$  indicates absence of secondary  $\text{SnS}_2$  phase. Fig 4. (c) shows FT-Raman spectrum of ZnS thin film. It is observed that ZnS has very low scattering efficiency due to lower film thickness and lower absorption and scattering in this range. Peaks available at  $654\text{ cm}^{-1}$  and  $1100\text{ cm}^{-1}$  confirms formation of ZnS phase. The observed Raman scattering efficiency in case of ZnS film was found very weak with green level visible excitation obtained due to less absorption as well as scattering in the particular region [40]. FT-Raman studies are in support with the XRD studies confirming the formation of the  $\text{Cu}_2\text{S}$ , ZnS and  $\text{SnS}_2$  thin films.

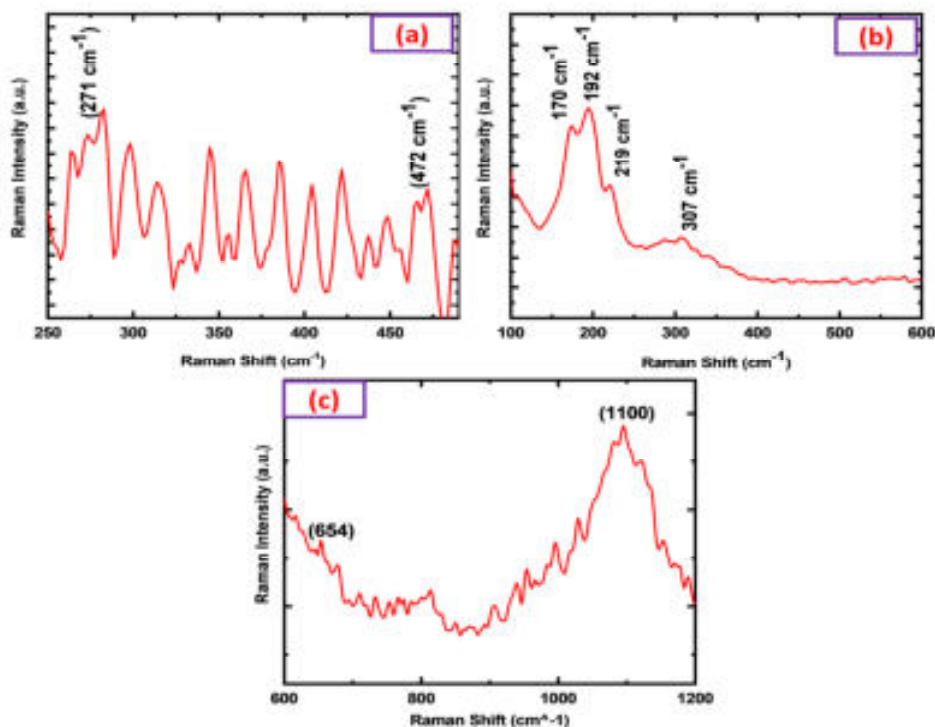


**Fig. 4 FT- Raman spectra of (a) Cu<sub>2</sub>S, (b) SnS<sub>2</sub> and (c) ZnS thin films**

The optical band gap of the metal chalcogenides thin films were estimated using well known Tauc's formula [34],

$$(\alpha h\nu)^{1/n} = A (h\nu - E_g) \quad (1)$$

However, “ $\alpha$ ” represents the absorption coefficient of respective thin film. The plot of  $(\alpha h\nu)^2$  versus  $h\nu$  for deposited thin films prepared by SILAR technique was given in the Fig. 5. On the basis of simulation, it is found that the absorption plot should attain linearity. Since, the divergence in absorption spectra of Cu<sub>2</sub>S film found at high bombardment of photons. It is found that the observed divergence are absent in case of SnS<sub>2</sub> and ZnS thin films. This can be ascribed to the formation of structural perturbation and surface level destruction in the respective films. The band gap energy graph of the prepared Cu<sub>2</sub>S, SnS<sub>2</sub>, and ZnS thin films as shown in Fig. 5.

The direct optical band gap values of synthesized Cu<sub>2</sub>S, SnS<sub>2</sub>, and ZnS thin films were 2.20, 1.65 and 3.20 eV respectively, which lies within the reported direct band gap range of literature value [35-37].

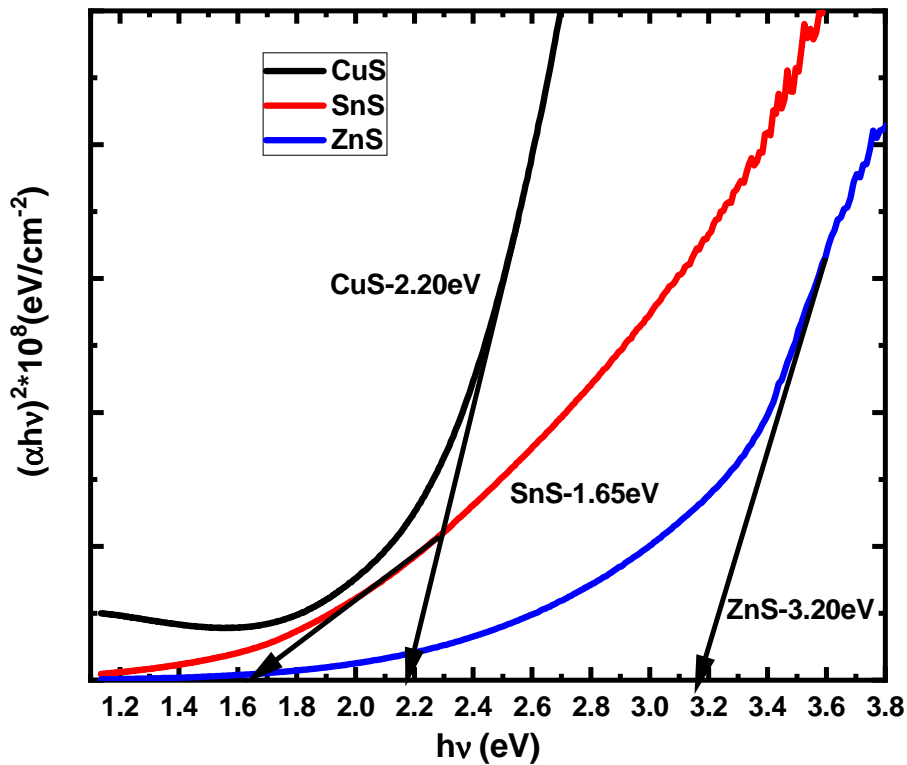


**Fig. 5 Band gap energy graph of Cu<sub>2</sub>S, ZnS and SnS<sub>2</sub> thin films**

#### 4. CONCLUSIONS

Thin films of Cu<sub>2</sub>S, SnS<sub>2</sub> and ZnS were successfully prepared by using SILAR method. XRD study confirmed the development of crystalline forms of the thin films. The SEM analysis showed that the as synthesized chalcogenides thin films were dense and homogeneous spherical in shape. The grains size in the range of 0.3 to 0.8 μm for all the prepared metal chalcogenides. The FT- Raman spectrum confirms all the bonds were present in the prepared chalcogenides. The direct optical band gap values of synthesized Cu<sub>2</sub>S, SnS<sub>2</sub> and ZnS thin films were 2.20, 1.65 and

3.20 eV, respectively. Based on these characterizations metal chalcogenides were suitable for solar cell application.

## ACKNOWLEDGMENT

The author VLP, SRB, RRB would like to acknowledge the Chhatrapati Shahu Maharaj Research Training and Human Development Institute (SARTHI), Pune (Government of Maharashtra) for the financial support under the Chhatrapati Shahu Maharaj National Research Fellowship-2019 and 2021.

## REFERENCES

1. Gao J., Li Q., Zhao H., Li L., Liu C., Gong Q., Qi L., (2008) *Chem. Mater.*, 20, 19
2. Cao H., Qian X., Wang C., Ma X., Yin J., Zhu Z., (2005) *J. Am. Chem. Soc.*, 127, 16024
3. Jiao S., Xu L., Jiang K., Xu D., (2006) *Adv. Mater.*, 18, 1174
4. Li B., Xie Y., Xue Y., (2007) *J. Phys. Chem., C* 111, 1218
5. Wan S., Guo F., Shi L., Peng Y., Liu X., Zhang Y., Qian Y., (2004) *J. Mater. Chem.*, 14, 2489
6. Schneikart A., Schimper H., Klein A., Jaegermann W., (2013) *J. Phys. D Appl. Phys.*, 46, 305109
7. Kawano Y., Chantana J., Minemoto T., (2015) *Curr. Appl. Phys.*, 15, 897
8. Steinmann V., Jaramillo R., Hartman K., Chakraborty R., Brandt R., Poindexter J., (2014) *Adv. Mater.*, 26, 7488
9. Sinsermsuksakul P., Sun L., Lee S., Park H., Kim S., Yang C., (2014) *Adv. Energy Mater.*, 4, 1400496
10. Herzenberg R., Kolbeckina, (1932) *Aires. Rev. Miner.*, 4, 33
11. Ehm L., Knorr K., Dera P., Krimmel A., Bouvier P., Mezouar M., (2004) *J. Phys. Condens. Matter.* 16, 3545

12. Albers W., Haas C., van der Maesen F., (1960) *J. Phys. Chem. Solids*, 15, 306
13. Vidal J., Lany S., D'Avezac M., Zunger A., Zakutayev A., Francis, (2012) J., *Appl. Phys. Lett.*, 100, 032104.
14. Cheng S., Conibeer G., ( 2011) *Thin Solid Films*, 520, 837
15. Devika M., Reddy N., Ramesh K., Ganesam V., Gopal E., Ramakrishna K., (2006), *Appl. Surf. Sci.*, 253, 1673
16. Hartman K., Johnson J., Bertoni M., Recht D., Aziz M., Scarpulla M., (2011) *Thin Solid Films*, 519, 7421
17. Gao C., Shen H., Sun L., (2011), *Appl. Surf. Sci.*, 257, 6750
18. Yue G., Peng G., Yan P., Wang L., Wang W., Luo X., (2009) *J. Alloys. Compd.*, 468, 254
19. Reddy K., Reddy P., Miles R., Datta P., (2001) *Opt. Mater.* 17, 295
20. Sinsermsuksakul P., Heo J., Noh W., Hock A., Gordon R. G., (2011) *Adv. Energy Mater.* 1, 1116
21. Jiang T., Ozin G., (1998) *J. Mater. Chem.* 8, 1099
22. Ristov M., Grozdanov I., Mitreski M., (1989) *Thin Solid Films*, 173, 53
23. Reddy K., Reddy N., Miles R., (2006) *Sol. Energy Mater. Sol. Cells*, 90, 3041
24. Ikuno T., Suzuki R., Kitazumi K., Takahashi N., Kato N., Higuchi K., (2013), *Appl. Phys. Lett.*, 102, 193901
25. Park H., Heasley R., Sun L., Steinmann V., Jaramillo R., Hartman K., (2015) , *Prog. Photovolt. Res. Appl.* 23, 901
26. Hu L., Chen M., Shan W., Zhan T., Liao M., Fang X., Hu X., Wu L., ( 2012) *Adv. Mater* 24, 5872
27. Kim S., Kim T., Kang M., Kwak S., Yoo T., Park L., Yang I., Hwang S., Lee J., Kim S. and Kim S., (2012) *J. Am. Chem. Soc.* 134, 3804
28. Ubale A., Sangawar V. and Kulkarni D., (2007) *Bull. Mater. Sci.* 30, 147
29. Yu Y., Hyun M., Nam S., Lee D., Lee B., Yu P., Choi Y., (2002) *J. Appl. Phys.* 91,9429

30. Wang X., Shi J., Feng Z., Li M. and Li C., (2011) *Phys. Chem. Chem. Phys.* 13, 4715
31. Liu J., Chen H., Lin Z., Lin J. M., (2010 ) *Anal. Chem.* 82, 7380
32. Kumar S., Khadar M., Nair K., Dhara S., Magudapathy P. J., ( 2008) *Raman Spectrosc* 39, 1900
33. Yu J., Joo J., Park H., Baik S., Kim Y., Kim S., Hyeon T., ( 2005) *J. Am. Chem. Soc.* 127, 5662
34. Maji S., Mukherjee N., Dutta A., Srivastava D., Paul P., Karmakar B., Mondal A., Adhikary B., (2011) *Mater. Chem. Phys.* 130, 392
35. Pathan H., Kale S., Lokhande C., Ahn J., Joo S., (2007) *Mater. Res. Bull.* 42, 1565
36. Vidal J., Lany S., d'Avezac M., Zunger A., Zakutayev A., (2012) *Appl. Phys. Lett.* 100, 032104
37. Lopez, M. Espinos J., Martin F., Leinen D. and Barrado J., (2005) *J. Cryst. Growth* 285, 66

# Gas Sensor Based on Metal Oxide-Polymer Composites

Satyashila D. Ghongade<sup>a</sup>, Pradnya G. Raje<sup>a</sup>, Shital J. Shinde<sup>a</sup>, Azeem M. Bagwan<sup>a</sup>, Rajendra G. Sonkawade<sup>a\*</sup>

<sup>a</sup>Department of Physics, Shivaji University, Kolhapur 416 004, Maharashtra, India.

\*Corresponding author: rgs\_phy@unishivaji.ac.in

---

---

## ABSTRACT

*Researchers are trying to develop sensors based on metal oxide-polymer composites used at low concentrations and low temperatures. These materials have excellent environmental stability and endurance, providing numerous advantages over individual constituents, and are widely used in sensor applications. Because of their synergic interaction, the composite outperforms a single metal oxide or polymer in terms of sensing performance. The composite shows enhanced sensing performance as compared to a single metal oxide or polymer due to their synergic interaction. This work emphasizes an overview of metal oxide-polymer composites for sensing performance, and finally, we comment on the future research directions for further development in this field.*

## KEYWORDS

*Metal Oxides, Conducting Polymers, Composite, Gas Sensor.*

.....

## 1. INTRODUCTION

A sensor is an electronic device that converts gas concentrations and components into conventional electrical signals. There are a variety for applications of sensors in various fields, such as drug delivery, remote control, water, air, food quality, and agriculture. It is essential to continuously measure the concentration of dangerous gases in the air to protect the environment and human health from the adverse effects of air pollution. For real-time applications, accurate and quick detection, stability and reproducibility, and cost effectiveness are the features needed to be met by the modern sensing scheme [1]. The performance of gas sensors influences several parameters, including sensitivity, characteristic response, selectivity, operating temperature, detection limit, and additives or dopants [2], which are schematically represented in **Figure-1**. For practical applications, gas sensors must have high responsibility, quick response and recovery, room-temperature (RT) working, strong selectivity and stability, and ease of fabrication [3]. To meet these requirements, many types of gas sensors have evolved from metal oxides (MOs), polymers, carbon materials, metal-organic frameworks (MOFs), MXenes, and other two-dimensional (2D) materials. Several investigations have been undertaken to construct gas sensors using MOs such as ZnO [4], WO<sub>3</sub> [5], TiO<sub>2</sub> [6], SnO<sub>2</sub> [7], etc.

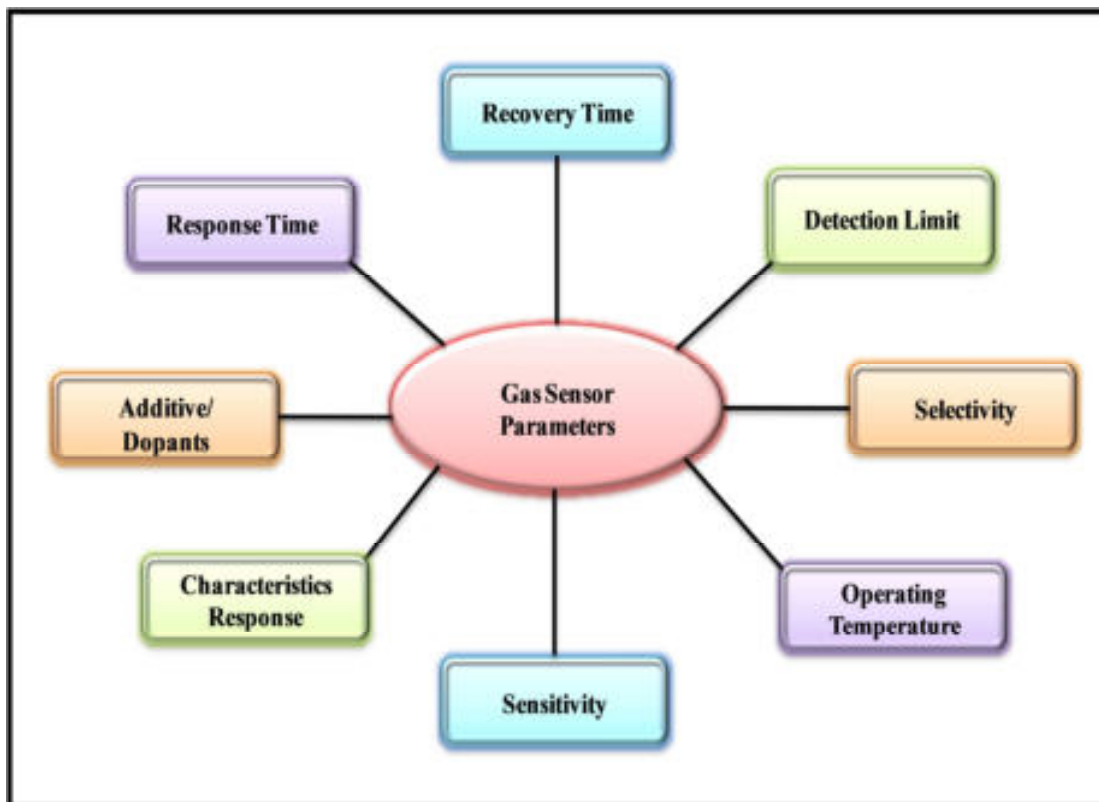


**Figure-1. Schematic representation of the various parameters influenced by the performance of the gas sensor**

The MOs exhibit greater feasibility due to their catalytic behaviour, wide band gap, tunable conductivity, and dielectric nature [1].

The field of MO-based gas sensors has grown significantly in order to improve selectivity, sensitivity, and response time. Because of their high operating temperature and higher power consumption, MO-based sensors have limited applications. Single MOs have several drawbacks. They need higher temperatures for formation, so the sensing efficiency is reduced [8]. As a result, researchers focused primarily on modifying them to lower their operating temperature by incorporating polymers. Composites of conducting polymers (CPs) and metal oxides (MOs) for gas-sensing utilization have the interest of researchers owing to their synergistic properties, which have attracted extensive interest in gas-sensing applications. Because of their oxygen stoichiometry and active surface charges, MOs can make sensors more responsive to the target gases. On the other hand, the presence of CPs can affect the working temperature and lead to better selectivity for various gases [8]. The goal of today's research is to lower the sensor's working temperature while enhancing sensitivity, response, and recovery time. This review article provides an overview of various types of metal oxide-polymer materials for sensing applications.

### **1.1 Advantages and scope of composite material for gas-sensor application**

The goal of today's research is to reduce the working temperature of the sensor while increasing sensitivity, response, and recovery time. The composite structures are

made of various organic-organic and organic-inorganic materials, and they achieve excellent properties by combining different materials with different compositions. When two or more materials are combined, their properties are altered, resulting in hybrid materials with innovative and distinct properties [9]. MO-polymer nanocomposite with improved optical, mechanical, and electrical properties for gas sensor applications that combines the benefits of both organic polymer material and inorganic metal oxide [10]. The ability of polymer-based sensors to have their physical and chemical properties tuned so that their resistance to degradation, biodegradability, and flexibility can be modified is what makes them useful. Polymers have a low formation temperature; at a lower temperature, fewer electrons are created at the material's surface, and such materials are thermally stable but have a lower response. When the gas sensors are subjected to higher concentrations at low operating temperatures, their response, recovery, and stability suffer [11]. But the issue with the bare polymers is their low chemical stability and mechanical strength. The creation of MO-polymer-based composites makes it possible to combine the advantages of both materials while eliminating their drawbacks [10].

## **2. AN OVERVIEW OF METAL OXIDE-POLYMER COMPOSITES FOR GAS SENSOR APPLICATION MATERIALS**

The MO gas sensors achieved superior sensing performance when subjected to  $\text{NH}_3$ ,  $\text{H}_2\text{S}$ ,  $\text{NO}_2$ , LPG, toluene, acetone, and many more gases [12], but they needed higher formation and operating temperatures. High temperatures reduce the sensor's life and involve higher power consumption. As a result, developing a gas sensor that operates at room-temperature is highly desirable. Currently, there is a lot of interest in studying improved sensing properties using hybrid materials like organic (CP) and inorganic (MO) composites [13]. The complementary behaviour between polymers and MOs resolves the problems associated with pristine MOs gas sensors. Polyaniline (PANI) and polypyrrole (PPy) are the most promising CPs for detecting hazardous as well as flammable gases at room temperature, even at low gas concentrations [14,15]. Here we discuss MOs hybrids with polymers such as ZnO,  $\text{TiO}_2$ ,  $\text{WO}_3$ ,  $\text{SnO}_2$ , etc.

ZnO has gotten a lot of attention in the last year because of its large band gap, high excitation energy, high chemical stability, and good mechanical strength. Bare ZnO has some disadvantages. It requires a high temperature for efficient sensing performance and is not as effective at room temperature. The performance of the ZnO-PANI nanocomposite for ethanol, methanol, and  $\text{NH}_3$  sensing at room temperature was reported by Das and his colleagues [13]. According to the author, ZnO-PANI nanocomposite is highly selective for  $\text{NH}_3$  gas, has a quick response time, and is more stable than single-phase PANI film. ZnO and sulphate ions are present in the PANI chain, which contributes to the comparatively quick recovery time of ZnO-PANI composite films. The composite's response time is about 21 sec, which is substantially faster than that previously reported. According to the author's finding, sensors fabricated from the composite exhibit better selectivity towards  $\text{NH}_3$  with a low detection limit, quick response, and fast recovery, along with high stability at room temperature.  $\text{NO}_2$  has become a significant pollutant gas because it is highly

oxidizing and toxic, and it also causes acid rain. The NO<sub>2</sub> sensing capabilities of Ni-doped ZnO-PANI composites were studied by Jain et al. [8] using an in-situ oxidative polymerization technique. ZnO nanoparticles not only tune the surface-active sites for adsorption and desorption of target gases but also tune the semiconducting properties. Because of its higher electrical conductivity, PANI could improve electron transfer rates. Ni-doped ZnO-PANI sensors outperformed pure PANI and ZnO/PANI nanocomposite sensors in terms of selectivity, sensitivity, and response, achieving 75% sensing response towards 100 ppm of NO<sub>2</sub> gas at ambient temperature with response and recovery times of 82 sec and 399 sec, respectively. The result showed that doping Ni over ZnO nanorods increases their surface area and maximizes gas adsorption, resulting in a very effective NO<sub>2</sub> gas sensor at room temperature [8].

In another report, Sonker et al. [16] reported the NO<sub>2</sub> sensing performance of pure ZnO and PANI-ZnO composite thin films. The variation of PANI concentration in a ZnO composite thin film with exposure to different NO<sub>2</sub> gas concentrations was investigated in this work, and it was discovered that the sensor was highly responsive, had good selectivity, had better reproducibility, and was functional at room temperature. With the incorporation of p-type PANI into Z-type ZnO, it was found to increase the sensing response towards NO<sub>2</sub> gas. This could be because p-n heterojunctions form in the hybrid composite films, and PANI chains are surrounded by mesh-like structures made by ZnO nanoparticles. The model for ZnO-PANI heterojunction through the schematic is shown in **Figure-2**. Minority charge carriers in PANI are less energetic to move to the conduction band during the formation of the p-n junction; as a result, a small variation was observed at first, but because ZnO is n-type and abundant in the sample, the n-type nature of films will dominate. Minority charge carriers in PANI are less energetic to move to the conduction band during the formation of a p-n junction; as a result, a small variation was observed at first, but because ZnO is n-type and abundant in the sample, the n-type nature of films will dominate. Only PANI will enhance the rate of reaction with oxidizing gases like NO<sub>2</sub>. The first oxygen species were adsorbed on the surface of air particles and then ionized into O<sub>ads</sub><sup>-</sup>, capturing free electrons from the particles and resulting in the formation of a thin space charge layer and increased surface bending. Because the doped PANI has a lower band gap than that of ZnO, the electrons are transferred to the PANI, resulting in the formation of an accumulation layer at the ZnO-PANI interface. The film was stabilized before being exposed to NO<sub>2</sub>, which was adsorbed by the heterojunctions between ZnO and PANI. In the reaction, the electron served as an electron acceptor, and an acceptor surface state was observed. Because the surface state energy level is close to the valence band edge in order to bring the Fermi level close to the surface state. As a result, fewer electrons are transferred from ZnO to PANI, resulting in an increase in resistance. After stopping the supply of NO<sub>2</sub>, the trapped electrons are released into heterojunctions between ZnO and PANI by NO<sub>2</sub>, resulting in a decrease in resistance. As a result, this sensor structure can be used to detect NO<sub>2</sub> gas at commercial levels at room temperature with confidence [16].

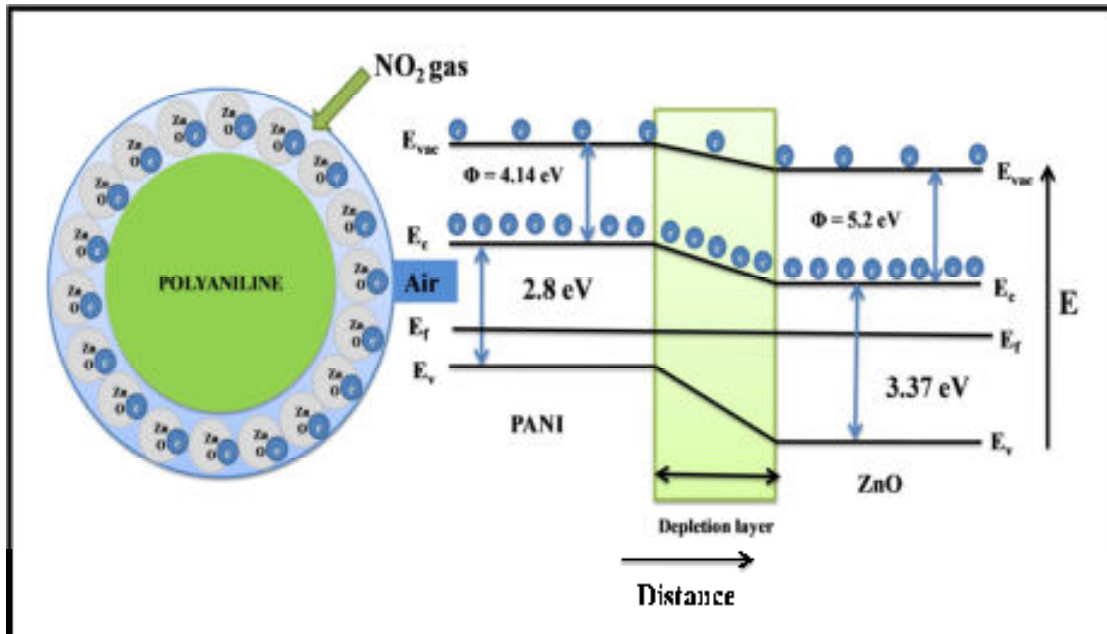


**Figure-2. Schematic representation of proposed mechanism of NO<sub>2</sub> sensing of ZnO/PANI heterojunction**

Barkade et al. [17] worked on PPy/ZnO functional materials synthesised by the ultrasound-assisted oil-water mini-emulsion method at different concentrations of ZnO (2, 4, 6, 8, and 10 wt%) in order to improve the efficiency of liquefied petroleum (LPG) gas. The use of ultrasound acts as a size-controlling tool in the synthesis, which enhances the interaction between ZnO and PPy nanoparticles. The ultrasound irradiation significantly improves the process of encapsulating ZnO nanoparticles into the PPy chains, resulting in cavitation conditions that ensure the formation of a miniemulsion. **Figure-3** depicts the reaction mechanism for the formation of a hybrid PPy/ZnO nanocomposite using the ultrasound-assisted miniemulsion method. The response curve of the PPy and PPy/ZnO sensors as a function of LPG concentrations varies from 1000 ppm to 1800 ppm, as illustrated in **Figure-4a**. The response increases up to 1400 ppm for both PPy and PPy/ZnO sensors and remains constant for higher concentrations of LPG. Both PPy and PPy/ZnO nanocomposite exhibit the highest response at 1400 ppm concentration of LPG, and the response amplitude of PPy/ZnO nanocomposite is higher than that of pure PPy. **Figure-4b** indicates the sensing reproducibility of the PPy/ZnO nanocomposite sensor prepared with 10 wt% of ZnO for 1400 ppm of LPG. The PPy/ZnO nanocomposite sensor shows steady behaviour with repeated exposure to LPG for up to three cycles. The study found that the PPy/ZnO-based sensor responded more quickly than bare PPy in the presence of LPG [17].

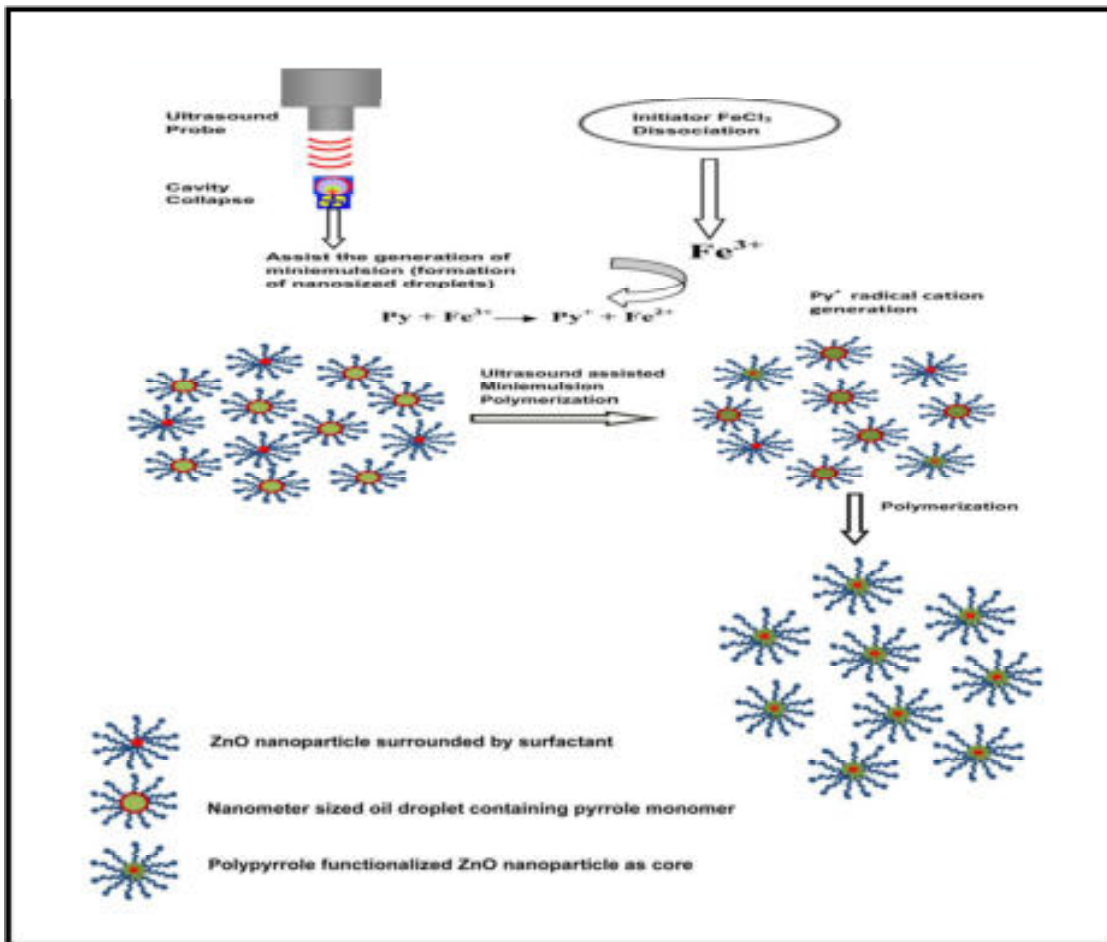


Figure-3. Reaction mechanism for the formation of a hybrid PPy/ZnO nanocomposite using the ultrasound-assisted miniemulsion method. Adapted with permission from [17]. Copyright (2013) American Chemical Society.

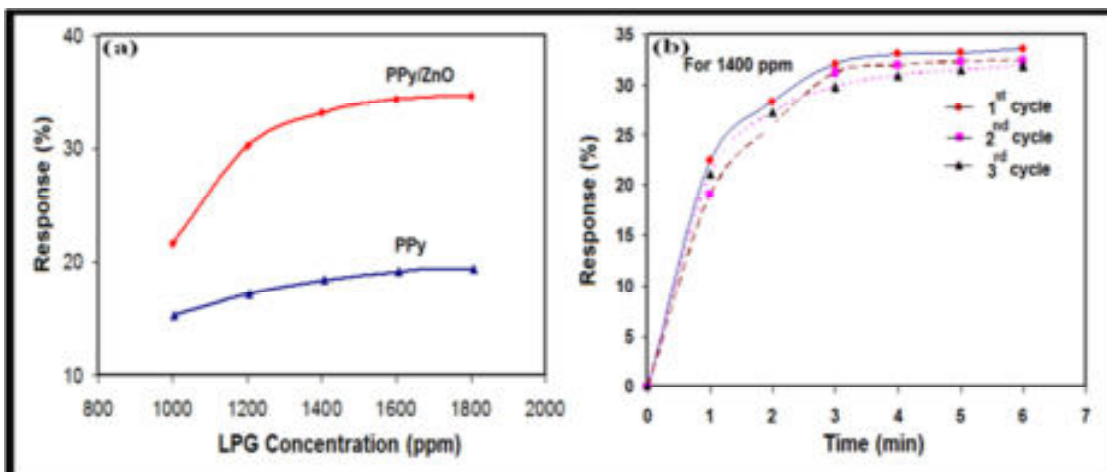
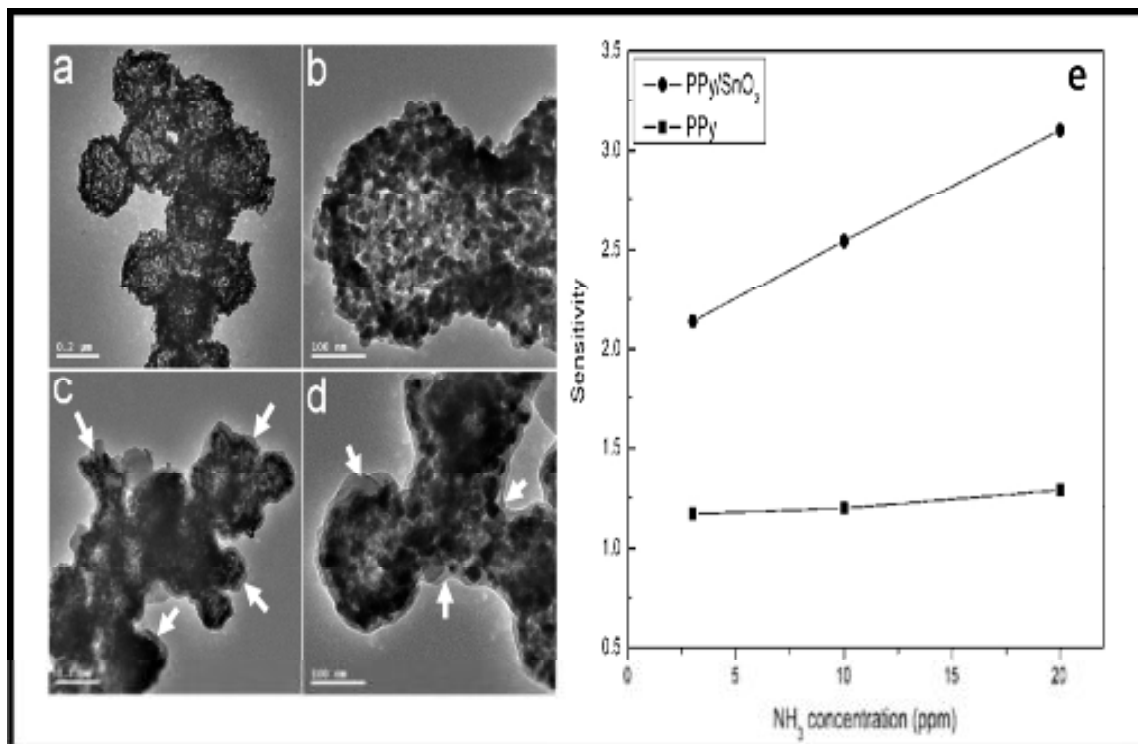


Figure-4. a) Response of PPy and PPy/ZnO sensors as a function of concentration of LPG b) Sensing reproducibility of the PPy/ZnO nanocomposite sensor prepared with 10 wt% ZnO (1400 ppm of LPG). Adapted with permission from [17]. Copyright (2013) American Chemical Society.

The detection of greenhouse gases has become essential to controlling the damage to the environment and the quality of life. CO<sub>2</sub> is the major greenhouse gas. Hence, the detection and control of CO<sub>2</sub> levels in the environment are essential. Sonker et al. [6] used a spin-coating technique to create a TiO<sub>2</sub>-PANI nanocomposite thin film and tested its CO<sub>2</sub> sensing performance at room temperature. The pure TiO<sub>2</sub> achieved a sensing response of 1.77, while the TiO<sub>2</sub>-PANI thin film sensor exhibited a 7.76 sensing response, indicating that this sensor structure can be used for the detection of CO<sub>2</sub> gas [6]. In another work, Seif et al. [18] worked on ultra-violet (UV)-irradiated TiO<sub>2</sub>/PANI core-shell NFs for NH<sub>3</sub> sensing performance. Without exposing it to UV irradiation, the TiO<sub>2</sub>/PANI hybrid showed an 18.1% response towards 1 ppm of NH<sub>3</sub>, while the UV-irradiated TiO<sub>2</sub>/PANI hybrid exhibited a 53.11% response towards 1 ppm of NH<sub>3</sub>, with significant response (58 sec) and recovery (38 sec) times. The work concluded that exposure to UV irradiation of the sensing material significantly improves the gas sensing performance, and UV light exposure leads to a reduction in recovery and response time [18].

Due to its exceptional semiconducting properties, WO<sub>3</sub> is an n-type gas-sensing material [5]. However, there are some drawbacks to single WO<sub>3</sub>-based gas sensors, including their operating temperature, long-term stability, and lower detection. Hence, hybrids of WO<sub>3</sub> with polymers were fabricated by researchers for long-term stability and excellent sensing performance [19]. Li and co-workers [5] developed a WO<sub>3</sub> hollow spheres@PANI hybrid sensing device that operated at a lower temperature. The fabricated sensor achieved a sensing response of 25 towards 100 ppm of NH<sub>3</sub> at 20 °C. The improvement in sensing parameters is attributed to the heterojunction between PANI (p-type) and WO<sub>3</sub> (n-type) hollow spheres [5]. Zhang et al. [7] investigated the performance of PPy-coated SnO<sub>2</sub> hollow spheres for NH<sub>3</sub> sensing. The PPy-coated SnO<sub>2</sub> hollow spheres were synthesized through in-situ polymerization of pyrrole monomer in the presence of SnO<sub>2</sub> hollow spheres. The figure depicts the TEM images of SnO<sub>2</sub> hollow spheres and PPy-coated SnO<sub>2</sub> hollow spheres. It is seen that the SnO<sub>2</sub> hollow spheres have a rough and porous morphology (**Figure-5a and Figure-5b**), and TEM images of PPy-coated SnO<sub>2</sub> hollow spheres show that the SnO<sub>2</sub> hollow spheres were homogeneously wrapped by PPy coatings (**Figure-5c and Figure-5d**). **Figure-5e** shows the sensitivity of gas sensors to different NH<sub>3</sub> gas concentrations at room temperature and clearly shows that the sensitivity of PPy-coated SnO<sub>2</sub> hollow spheres is higher than that of SnO<sub>2</sub> hollow spheres. The great sensitivity of PPy-coated SnO<sub>2</sub> is caused by a number of factors. A fine pathway for electron transfer in the gas sensing process is provided by the interconnection of SnO<sub>2</sub> hollow spheres with PPy coatings. The synergic interaction of PPy and SnO<sub>2</sub> hollow spheres may result in the formation of a p-n junction, which is also responsible for improved sensing performance [7].



**Figure-5. TEM images of a-b) pristine SnO<sub>2</sub> hollow spheres and c-d) Polypyrrole-coated SnO<sub>2</sub> hollow spheres, e) Sensitivity of gas sensors to different ammonia gas concentrations at room temperature. Adapted with permission from [7]. Copyright (2009) American Chemical Society.**

**Table-1** shows the various metal oxide-polymer composites for gas sensor applications with various parameters such as synthesis route, gas, gas concentration, response/recovery time, operating temperature, etc.

**Table-1. Various metal oxide-polymer composite for gas sensor application**

Material	Synthesis Route	Gas	Gas concentration (ppm)	Response	Operating Temperature (°C)	Response/Recovery time	Ref.
WO <sub>3</sub> @PANI	Two step method	NH <sub>3</sub>	100	25	20	-	[5]
Ni@ZnO/PANI	In-situ polymerization	NO <sub>2</sub>	100	75%	RT	82 sec /399 sec	[8]
PPy-WO <sub>3</sub>	Solid state synthesis	NO <sub>2</sub>	100	61%	RT	-	[19]

PANI/TiO <sub>2</sub>	In-situ chemical oxidation polymerization	NH <sub>3</sub>	23	1.67	25	18 sec /58 sec	[20]
PANI/SnO <sub>2</sub>	Solution route technique	NH <sub>3</sub>	100	-	RT	15 sec /80 sec	[21]
SnO <sub>2</sub> -Ag-PPy	Chemical method	NH <sub>3</sub>	0.02	3.15%	RT	-	[22]
TiO <sub>2</sub> -Au-PPy	Chemical method	NH <sub>3</sub>	0.02	3.2%	RT	-	[22]

**Specification** DMA: Dimethylamine

### 3. CONCLUSION

There is a greater need for gas sensors to detect atmospheric pollutants. These pollutants are hazardous to human health and the environment; detecting them in the future is essential. Single MO and polymers have some drawbacks, such as the fact that MO requires a higher temperature to form, reducing sensing efficiency. Polymers have a low formation temperature, but at a low operating temperature, their response, recovery, and stability suffer. As a result, researchers concentrated on lowering the operating temperature while maintaining stability. Various research groups around the world are continuously working on metal oxide-polymer composites for sensor applications. This review article is focused on MO-polymer composites for the detection of numerous dangerous and flammable gases. The expansion of the application spectrum is provided by the overall hybridization condition. MO-polymer composites that are both eco-friendly and cost-effective are essential for the evolution of effective sensor devices, which will be a significant step forward in sensing applications.

### ACKNOWLEDGMENT

The financial assistant provided through DST PURSE-Phase II (2018-2022) and UGC DSA-Phase II (2018-2023) is highly acknowledged.

### REFERENCES

1. Usha, S. P., Shrivastav, A. M., Gupta, B. D. (2018) Optical Fiber Technology, 45, 146-166.
2. Gadkari, A. B., Shinde, T. J., Vasambekar, P. N. (2011) IEEE, 11, 849–861.
3. Abdel-Karim, R., Reda, Y., Abdel-Fattah, A. (2020) Journal of The Electrochemical Society, 167, 037554.
4. Patil, V. L., Vanalakar, S. A., Patil, P. S., Kim, J. H. (2017) Sensors Actuators B. Chemical, 239, 1185–1193.

5. Li, A. S., Liu, A., Yang, Z., Zhao, L. (2019) *Sensors Actuators B. Chemical*, 289, 252-259.
6. Sonker, R. K., Sabhajeet, S. R., Yadav, B. C. (2016) *Journal of Materials Science: Materials in Electronics*, 27, 11726-11732.
7. Jun, Z., Shurong, Mijuan W., Yan X., Huijuan W., Shoumin X., Xianzhi Z., Shihua W. (2009) *The Journal of Physical Chemistry C*, 113, 1662-1665.
8. Jain, S., Karmakar, N., Shah, A., Shimpi, N. G. (2019) *Materials Science and Engineering B: Solid-State Materials for Advanced Technology*, 247, 114381.
9. Rejab, M. R. B. M., Hamdan, M. H. M., Ma, Q., Siregar, J. P., Bachtiar, D., Muchlis, Y. *Encyclopedia of Renewable and Sustainable Materials*, edited by Choudhury I., Hashmi S., Elsevier, (2019).
10. Nemade, K. R., Waghuley, S. A. (2013), *Materials Science and Engineering: B*, 3, 310-313.
11. Ganesh, R. S., Navaneethan, M., Patil, V. L., Ponnusamy, S. Muthamizhchelvan, C., Kawasaki, S., Patil, P. S., Hayakawa, Y. (2017) *Sensors Actuators B. Chemical*, 255, 672-683.
12. Saasa, V., Malwela, T., Lemmer, Y., Beukes, M., Mwakikunga, B. (2020) *Materials Science in Semiconductor Processing*, 117, 105157.
13. Das, M., Sarkar, D. (2017) *Ceramic International* 43, 11123-11131.
14. Li, Y. Ban, H. Yang, M. (2016) *Sensors Actuators B. Chemical*, 224, 449-457.
15. Mekki, A., Joshi, N., Singh, A., Salmi, Z., Jha, P., Decorse, P., Lau-Truong, S., Mahmoud, R., Chehimi, M. M., Aswal, D. K., Gupta, S. K. (2014) *Organic Electronics*, 15, 71-81.
16. Sonker, R. K., Yadav, B. C., Sharma, A., Tomar, M., Gupta, V. (2016) *RSC Advances*, 6, 56149-56158.
17. Barkade, S. S., Pinjari, D. V., Singh, A. K., Gogate, P. R., Naik, J. B., Sonawane, S. H., Ashokkumar, M., Pandit, A. B. (2013) *Industrial & Engineering Chemical Research*, 52, 7704-7712.
18. Nikfarjam, A. Nikfarjam, A. Hajghassem, H. (2019) *Sensors Actuators B. Chemical*, 298, 126906.
19. Mane, A. T., Navale, S. T., Sen, S., Aswal, D. K., Gupta, S. K., Patil, V. B. (2015) *Organic Electronics*, 16, 195-204.
20. Tai, H., Jiang, Y., Xie, G., Yu, J. Chen, X. (2007) *Sensors Actuators B. Chemical*, 125, 644-650.
21. Deshpande, N. G., Gudage, Y. G., Sharma, R., Vyas, J. C., Kim, Y. P., Lee, J. B. (2009) *Sensors Actuators B. Chemical*, 138, 76-84.
22. Jiang, T., Wang, Z., Li, Z., Wang, W., Xu, X., Liu, X., Wang, J., Wang, C. (2013) *Journal of Materials Chemistry C*, 1, 3017-3025.

# Perovskite Oxide Based Resistive Switching Devices for Non-Volatile Memory: A Mini-Review

Lahu. D. Namade<sup>a</sup>, Tukaram. D. Dongale<sup>b</sup>, Amitkumar. R. Patil<sup>a</sup>, Namrata. A. Narewadikar<sup>a</sup>, Keshav. Y. Rajpure<sup>a\*</sup>

<sup>a</sup>Department of Physics, Shivaji University, Kolhapur.416004

<sup>b</sup>School of Nanoscience and Biotechnology, Shivaji University, Kolhapur, 416004, India

\*Corresponding author: rajpureky@gmail.com

## ABSTRACT

*Perovskite oxides have recently gained significant attention as promising materials for resistive switching applications. These materials possess unique electronic and optical properties, making them suitable for use in various electronic devices such as non-volatile memories (NVM) and logic circuits. Resistive switching is a property where the electrical resistance of a material changes upon the application of an electric field, allowing for the storage and retrieval of data. This property is based on the formation and rupture of conductive filaments within the material. Perovskite oxides show excellent resistive switching behavior due to their ability to undergo phase transitions and their high ionic conductivity. Moreover, they are relatively low-cost, environmentally friendly, and scalable, making them attractive for use in large-scale electronic devices. In this review, we present an overview of the recent progress in the field of perovskite oxides for resistive switching applications. We discuss the various factors that affect the resistive switching behavior, including material composition, electrode materials, and device architecture. Furthermore, we highlight the challenges that need to be overcome for the successful implementation of perovskite oxides in resistive switching devices and outline future directions for research in this area.*

**KEYWORDS:** Non-volatile memory (NVM); Resistive switching; RRAM; Perovskite Oxides

## 1. INTRODUCTION

Nanotechnology has developed rapidly over the past few years. There is a need for more efficient electronic components that researchers have driven to develop new materials and devices. Memristors are a relatively unexplored field in electronics that has become increasingly popular over the years [1]. Prof. Leon Chua discovered a two-terminal passive electronic device in 1971 named a memristor. A memristor gives a relationship between electric charge ( $q$ ) and magnetic flux ( $\phi$ ). The memristor is a two-terminal passive electronic element theoretically predicted by Leon Chua in 1971 [2,3]. Memristor has a unique property to remember the last resistance state [4].

Today in the data storage devices market, silicon-based flash memory has struggled to meet the requirements for future device development due to some limitations, like it requires high voltage, it consumes high power, and its retention capacity is limited. A growing trend in the miniaturization of electronic devices has increased the need for memory devices.

Memory devices based on RRAM are not only used as elements in analog circuits but can also be widely used in neuromorphic computing applications [5]. RRAM is considered a promising candidate for next-generation memory devices as the upcoming technology in non-volatile memory devices (NVM) [6]. NVM devices are growing attention in current microprocessor-based devices, which run different functions within electronic devices like smartphones, electric vehicles, wireless devices, etc. NVM, technology is based on the storage of charges. Therefore, charge storage-based devices are being studied for next-generation NVM applications, such as Static RAM (SRAM), dynamic RAM (DRAM), phase change memory (PCM), magnetic RAM (MRAM), and RRAM. Of these, RRAM is one of the most promising candidates for NVM because of its simple structure (Metal/Insulator/Metal), low operating voltage, large endurance, fast write, read and erase speeds, and excellent scalability. **Table-1** indicates the importance of RRAM devices where the parameters of voltage, retention, endurance, etc., are discussed in detail.

**Table-1. Comparison of memory technologies**

Memory technology	SRAM	DRAM	PCM	MRAM	RRAM	ref
Cell area	$> 100F^2$	$6F^2$	$4-20F^2$	$6-20F^2$	$< 4F^2(3D)$	[7]
Cell element	6T	1T1C	1T(D)1R	1(2)T1R	1T(D)1R	[7]
Voltage	$<1$ V	$<1$ V	$<3$ V	$<2$ V	$<3$ V	[8]
Read time	$\sim 1$ ns	$\sim 10$ ns	$< 10$ ns	$< 10$ ns	$< 10$ ns	[9]
Write time	$\sim 1$ ns	$\sim 10$ ns	$\sim 50$ ns	$< 5$ ns	$< 10$ ns	[10]
Write energy (J/bit)	$\sim fJ$	$\sim 10$ fJ	$\sim 10$ pJ	$\sim 0.1$ pJ	$\sim 0.1$ pJ	[11]
Retention	N/A	$\sim 64$ ms	$> 10$ y	$> 10$ y	$> 10$ y	[12,13]
Endurance	$> 10^{16}$	$> 10^{16}$	$> 10^9$	$> 10^{15}$	$\sim 10^6 - 10^{12}$	[14]
Multibit capacity	No	No	Yes	Yes	Yes	
Non-volatility	No	No	Yes	Yes	Yes	

**Figure-1** depicts a simple metal insulator metal (MIM) structure consisting of an RS layer sandwiched between the top and bottom electrodes. This simple structure consisting of a top electrode (Pt, Au, Ag, Al), bottom electrode (ITO, FTO), and RS layer makes ReRAM prominent [15–18]. There are several perovskite oxides, which are common active materials in memory devices. Aside from being highly durable, chemically stable, and fast, perovskite oxides also exhibit many unique properties due to their strong electron correlations, which make them highly promising materials for RRAM.

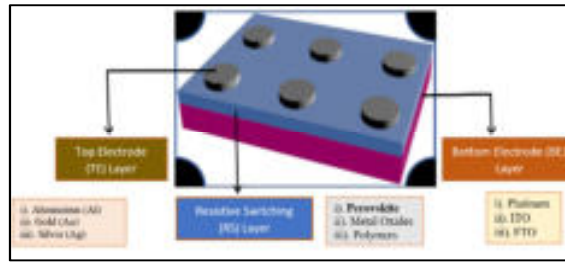


**Figure-1. Sandwich structure for ReRAM devices**

The following **Figure-2** shows the statistical analysis of published literature in the last five years in the field of memristor and perovskite materials-based memristor have been added in graphical form based on the Scopus database.

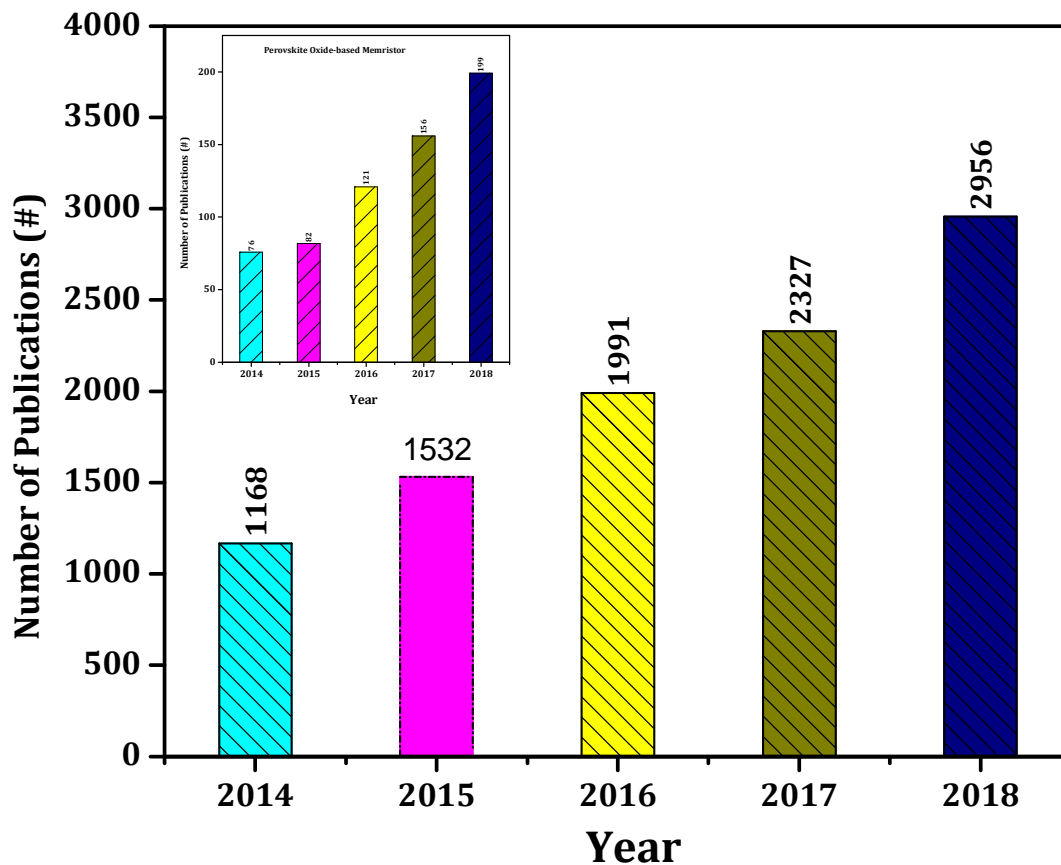


**Figure-2. statistical analysis of published literature in the last five years in the field of memristor and perovskite materials-based memristor**

### 1.1 Review of memristive properties

The defining property of memristor is its ability to store and recall information based on the resistance of the materials, which is referred to as memristance. Memristance is the result of the formation and rupture of conductive filaments within the material, and is controlled by the application of an electric field. One of the key properties of memristors is

their non-volatility, which means that they can retain information even when power is turned off. This makes them attractive for use in various electronic devices, such as memory and logic circuits. Another important property of memristors is their ability to exhibit both resistive and capacitive behavior, which make them suitable for use in various hybrid electronic devices. Furthermore, memristors have been shown to have high endurance, meaning that they can be switched between low and high resistance states many times without degradation. Additionally, memristors can exhibit multiple resistance states, which make them suitable for use in multi-level memory devices. In conclusion, the unique properties of memristors, non-volatility, resistive-capacitive behaviour, high endurance, and multiple resistance states, make them attractive for use in various electronic applications. There has been significant progress in the development of memristor devices in recent years, and they are poised to play a significant role in the future of electronics.

## 2. RS MECHANISMS OF RRAM DEVICES

RRAM has a simple three-layered M-I-M structure. The external voltage is applied across the top electrode in the MIM structure, and the bottom electrode and current will be measured using a semiconductor characterization system [19]. The device functions in the insulator's reversible soft breakdown, which changes its resistance by applying an external bias. The process of forming cation-based conducting filaments by metal electrodes is known as electrochemical metallization. An electrode consists of an inert metal to carry out the valence change mechanism (VCM), which causes to increase in electronic conductivity as oxygen is enriched [20–23]. Applying high voltage stress transforms the initial high resistance state into a low resistance state (LRS) called electroforming. The process of switching LRS to a high resistance state (HRS) by applying voltage is called the RESET process, and the process of switching HRS to LRS by applying external voltage is called the SET process. In the RS process, the change from the SET to RESET process gives the "ON" state, while the opposite behaviour shows the "OFF" state [19, 24]. Several insulating oxides and perovskites exhibit this RS behaviour.

### 2.1 Unipolar resistive switching (URS)

In URS, the switching direction depends only on the amplitude of applied voltage, not on polarity, as shown in **Figure-2a**. Under an external electric stimulus, a device in HRS can be transformed into LRS, which can be regarded as a forming process. Once the forming process is complete, LRS will be switched to HRS with threshold voltage ( $V_{\text{reset}}$ ). By introducing an electric stimulus ( $V_{\text{set}}$ ) greater than  $V_{\text{reset}}$ , the HRS is switched to the LRS. Current compliance (CC) is applied in the SET process to restrict the current. Alternatively, a series resistor can be combined with the SET process to limit the current. The current compliance (CC) is not applied in the RESET process. Generally, In unipolar RS,  $V_{\text{set}}$  may be larger than  $V_{\text{reset}}$ [25]. It should be noted that I–V curves are often symmetrical.

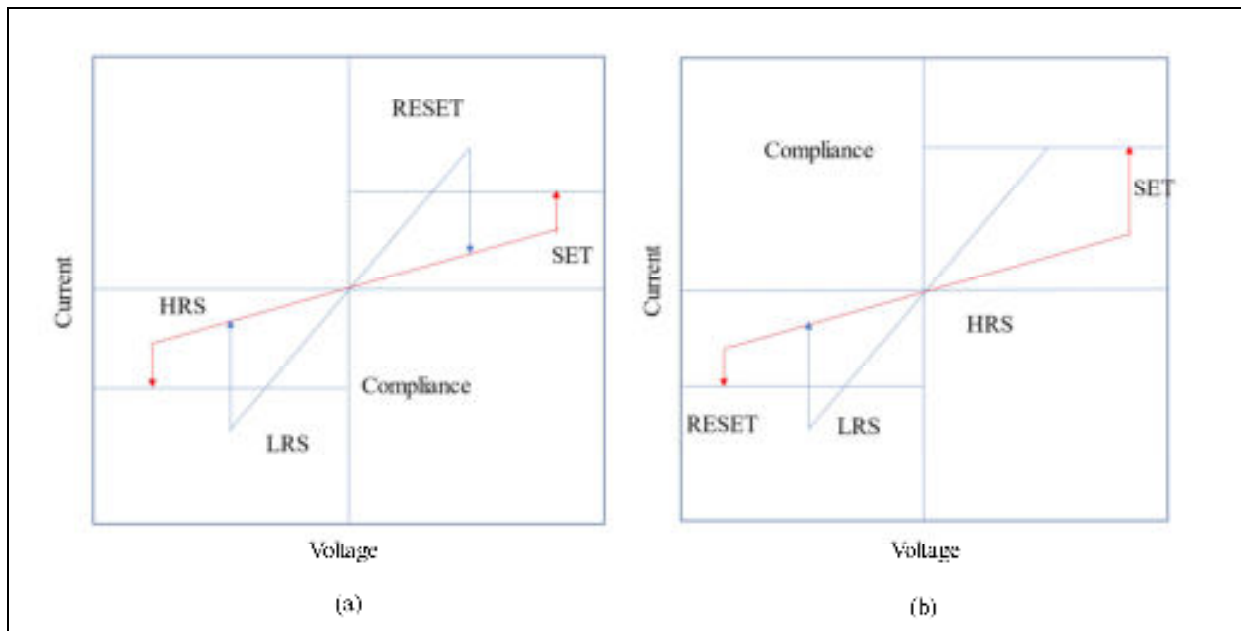


**Figure 3: Current-Voltage curves for RRAM. a) URS and b) BRS. Reproduced from [26]**

## 2.2 Bipolar resistive switching (BRS)

In a divergence from URS, the BRS in RRAM depends on the polarities of the external electric stimulus, as seen from a distinctive BRS Current-Voltage curve, as shown in **Figure-2b**. In the RESET process, the device is switched from an LRS to an HRS by applying a negative bias. Conversely, in the SET process, the device has to be switched from the HRS to the LRS. An input must satisfy amplitude and polarity conditions for BRS to operate. This spectacle occurs in many semiconducting oxides, such as perovskite [27-30].

## 2.3 Endurance

There is frequent switching between the HRS and the LRS for RRAM. As a result of switching between resistive states, each event can permanently damage the RRAM and decrease its performance. As an RRAM device varies between HRS and LRS, endurance describes how often the two can be switched without losing their distinct ratio [31]. Endurance testing determines how often the HRS and LRS can be switched effectively before they are no longer distinguishable from one another. On application of a read voltage, the endurance characteristics of RRAM can be determined by scanning the I-V of an RS cell and extracting the  $R_{HRS}$  and  $R_{LRS}$  [32]. In addition to accurate switching, this method is very slow since obtaining an I-V sweep takes a long time, especially if lower currents are used.

## 2.4 Retention

After a set and reset transition, it is crucial to investigate the stability of an RRAM device over a long period to determine its data retention. Memory cells retain their content for a specified period following a set/reset operation, i.e., the amount of time it takes to remain in their current state [33]. Using a low read voltage, constant voltage stress (CVS) over time can measure the current versus time (I-t) curve for both the LRS and HRS. Retention is usually not a concern since it is the natural state of the RRAM, and if no bias (or low bias) is applied, it will remain in this state. As the compliance limit increases during the switching process of

the LRS, the retention of the conducting filament increases, resulting in a more stable conducting filament over time, for instance, in RRAMs using conductive filament switching mechanisms [34][32].

### 3. PEROVSKITE OXIDES FOR RRAM DEVICES

A change in resistance is observed in some insulators when an electric field is applied. Recent research has investigated this property of resistance change for developing future non-volatile memory devices [35]. The use of oxide-based switching materials in non-volatile memory applications has been extensively studied due to their compatibility with CMOS semiconductors. The recent study of RS can be traced back to the discovery of hysteresis (I-V) properties in perovskite oxides such as BaTiO<sub>3</sub>, SrTiO<sub>3</sub>, BaSrTiO<sub>3</sub>, BiMnO<sub>3</sub>, and LiNbO<sub>3</sub>.

#### 3.1 BaTiO<sub>3</sub> (BTO)

Barium titanate (BTO) has been considered the most significant perovskite oxide material with an ABO<sub>3</sub> pattern. BTO possesses excellent properties like high dielectric constant (3.2 eV), ferroelectric activity, large optoelectronic coefficients, spontaneous polarization, and piezoelectricity attracted considerable attention from many researchers in the last few decades. BTO is a well-known ferroelectric material in the crystalline phase with a spontaneous polarization of  $\sim 26 \mu\text{C}/\text{cm}^2$  and with a large and tunable bandgap of 3.2 eV. Qian et al. [36] reported a Pt/BTO/LSMO/BTO/Pt switching device. A complimentary RS (CRS) memory device consists of two ferroelectric tunnel junctions, symmetrically connected by a metallic top electrode and a common bottom electrode based on BaTiO<sub>3</sub>. It permits the non-volatile storage of two states ("0" and "1") of each ferroelectric tunnel junction. In 2010, Linn et al. [37] proposed to solve the current-sneak problem by connecting two RS devices in complementary RS configurations such that if one device is in an LRS state, the other is in an HRS state (referred to as complementary RS, CRS). A single RS element in these circumstances does not store information, but two distinguishable coupled pairs, namely LRS+HRS and HRS+LRS, represent the logic states "0" and "1". The results presented that using BTO ferroelectric tunnel barriers and nanometric thin film electrodes, the two resistive states, HRS and LRS, determined and controlled by the polarization reversal, can be used as building blocks for a CRS device.

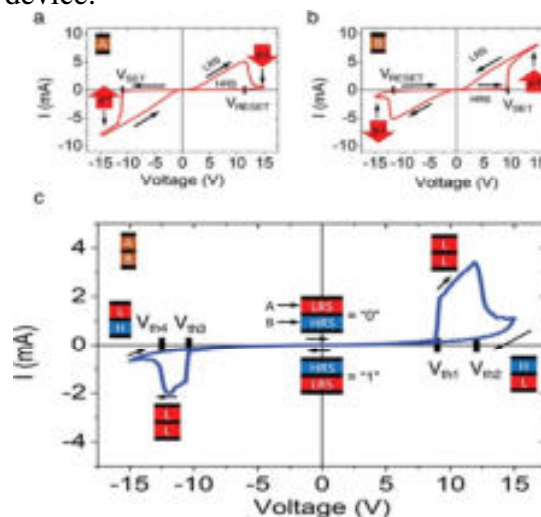


**Figure-4. a) I-V curve of junction A recorded in T-B contact configuration. b) I-V of junction B recorded in reversed T-B configuration. c) I-V curve of device AB recorded**

**in T–T contact configuration. Sketches indicate the resistance states (H=HRS, L=LRS) of the two anti-series connected capacitors. Reprint using Ref. [36]**

### 3.2 SrTiO<sub>3</sub> (STO)

Strontium titanate (STO) is an important para-electric perovskite material with cubic and tetragonal crystal structures depending on temperature. STO has lots of interesting properties, like high dielectric constant (3.2 eV), ferroelectric activity, piezoelectricity, good thermal stability, photoactivity, etc. According to these properties, STO has possible applications in RRAM, micro-electronics, photocatalysis, solar cell, and gas sensor. Perovskite STO appears to be an important material for the application of RRAM due to its high value of the dielectric constant that reduces the magnitude of leakage current. Stacking STO thin films with other semiconductor materials has been studied to achieve higher resistance ratios and even multilevel RS. Wang et al. prepared STO and Bi-doped STO films for non-volatile memory application by the sol-gel approach. They have also deliberated endurance and retention properties. STO and Bi-doped STO films deposited on Si or Pt substrate have identical phase compositions, morphology, and grain size; however, the grain size of the Bi-doped STO films deposited on Si is a little larger than that of the STO films deposited on Si or the Bi-doped STO films grown on Pt. The STO or Bi-doped STO films deposited on Si or Pt all show bipolar resistive-switching behaviour and observe the same conductive filament (CF) mechanism. Also, the Ag/ Sr<sub>0.92</sub>Bi<sub>0.08</sub>TiO<sub>3</sub>/Si device has the highest R<sub>HRS</sub>/R<sub>LRS</sub> of 10<sup>5</sup> and the greatest endurance and retention properties. The doping of Bi enhances the RS ratio of the STO films. Also, the Si substrates aid in improving the endurance and retention properties of the Bi-doped STO films [38]. Bera et al. synthesized a heterojunction RRAM composite ZnO nanorods (NRs) on STO substrate, which has a single shared crystallinity formed using the facile aqueous chemical deposition technique. In addition to their excellent rectification properties, Schottky diodes possess a photodetection capability, a photo-to-dark current ratio of 104, and a high forward-to-reverse bias ratio of 10<sup>3</sup>. set / reset voltage ranging from -4V to +4V. As a result of a reversible reconfiguration of ionic defects near the interface region, the voltage and photosensitive properties of ZnO/STO heterojunction diodes are modified [39].

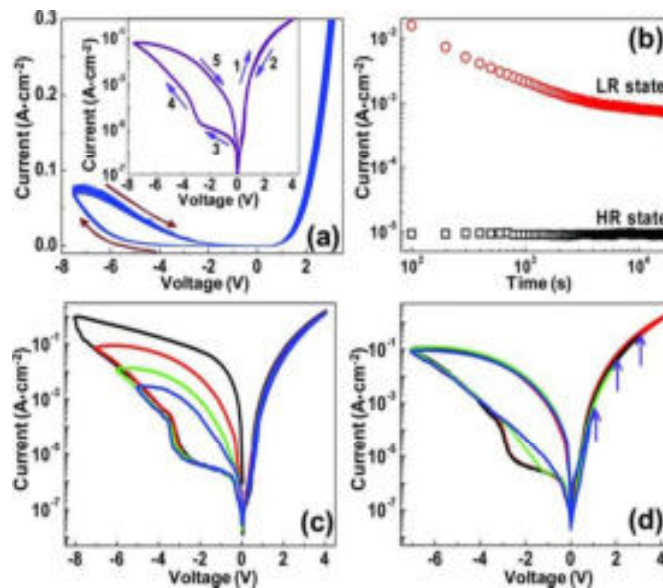


**Figure-5. a) I–V switching loop for 30 cycles. For clarity, the absolute value of the reverse current is plotted. Inset is the semi-log plot for a single loop with the scanning sequence and directions marked. b) Retention data of the ZnO NRs/NSTO heterojunction. Both ON and OFF states were measured at – 2 V. c) Switching loops showing the modulation of the LR state via scanning to different maximum negative voltages. d) Switching loops showing the modulation of the HR state as a result of different maximum positive voltages. The arrows mark the maximum positive voltages for different loops. Reprint using Ref. [39]**

### **3.3 BaSrTiO<sub>3</sub> (BSTO)**

A BaSrTiO<sub>3</sub> compound is a solid solution of barium titanate (BTO) and strontium titanate (STO) containing perovskites oxide (ABO<sub>3</sub>) nature. For decades, BSTO has been investigated for applications in tunable microwave devices and DRAM cells due to its high dielectric and low dielectric loss properties. The application of resistive random-access memory (RRAM) to BSTO films has recently been expanded by the demonstration of resistive switching (RS). Epitaxial BSTO thin films are deposited on SrTiO<sub>3</sub>:Nb (NSTO) using the hydrothermal method. When the Pt/BSTO/NSTO device is operated at a relatively low voltage, it shows typical rectification characteristics. In contrast, when it operates at relatively high voltage, it exhibits bipolar RS with a high and low resistance ratio greater than 10<sup>4</sup>. Under various reset voltages, negative differential resistance arises during the reset process, resulting in multilevel RS. As oxygen vacancies form at the interface of Pt/BST, these behaviors in Pt/BST/NSTO devices are likely due to electron trapping or detrapping. This process is referred to as the set process, which occurs when the voltage swept from 0V to 3V switches the resistive state from HRS to LRS.

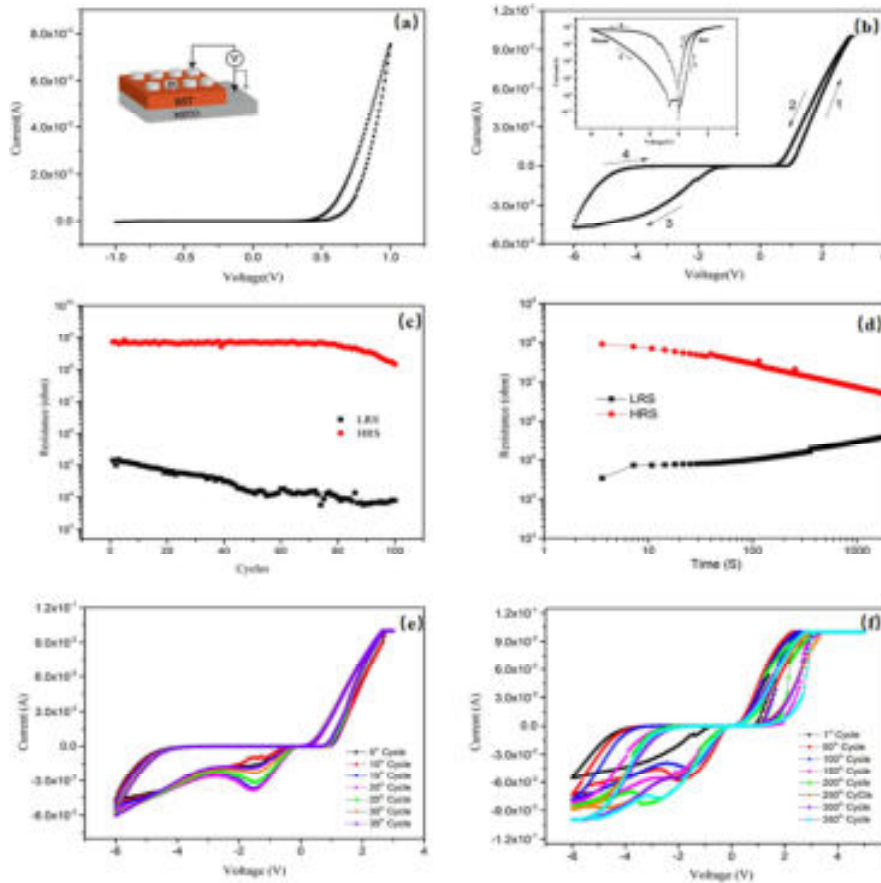


**Figure-6. a) Current-voltage (I–V) curves for the Pt/BST/NSTO device at low voltage b) BRS characteristics of the Pt/BST/NSTO device. Retention characteristics at (HRS) and (LRS) were measured at 0.1 V for c) 100 switching cycles and d) 1800 s. I–V curves for the Pt/BST/ NSTO device at e) -6V to 3 V and f) -6 V to 5V. Reprint using Ref. [40].**

### 3.4 BiMnO<sub>3</sub> (BMO)

BiMnO<sub>3</sub> (BMO) displays a perovskite structure (ABO<sub>3</sub>), and it shows ferromagnetic (FM) and ferroelectricity (FE) properties, like BiFeO<sub>3</sub> (BFO) and BiCrO<sub>3</sub> (BCrO). Because ferroelectric (FE) and ferromagnetic (FM) orders are coupled, these materials can switch spontaneous magnetization and electric polarization by applying electric and magnetic fields. Sun et al. [41] reported the light-controlled RS memory behaviour of multiferroic BMO nanowire arrays at room temperature by hydrothermal method, which is prominent for the next generation of NVM. The voltage was varying from 0 → + 4 V → 0 → - 4 V → 0. The device has two stable states of resistance when connected to the positive electric field. A sudden current increase occurs at about 3.85 V ( $V_{Set}$ ) in the dark and 4.0 V ( $V_{1 Set}$ ) under the presence of white light, shows that a "Set" process from an HRS to an LRS happens; when the applied voltage is varying from zero to a certain negative voltage ( $V_{Reset}$ ) of about -3.5 V in the dark and - 3.75 V ( $V_{1 Reset}$ ) under the presence of white-light, shows that a "Reset" process from an LRS to HRS occurs. It is demonstrated that BMO nanowires can control multiple levels of memory under light-controlled conditions because they provide a clear memory window in both the dark and under white light illumination [42].

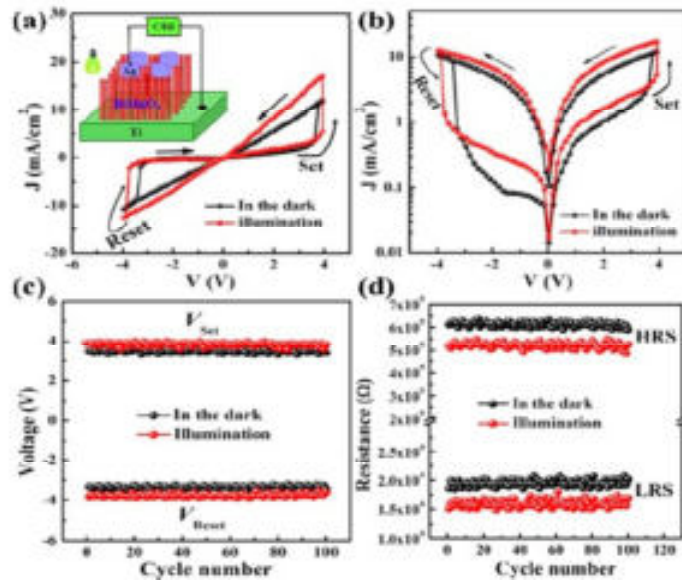


**Figure-7. a) The typical J-V characteristics curves Ag/BiMnO<sub>3</sub>/Ti structure in the dark and under white-light illumination; The inset shows the experimental test circuit. b) The corresponding resistive switching effects in logarithmic scale. c) The evolution of switching voltages including  $V_{Set}$  and  $V_{Reset}$  during the 100 resistive switching cycles in the dark and under white-light illumination respectively. d) The resistance-cycle number curve with 100 cycles under a positive bias voltage of 1.5 V in the dark and under white-light illumination respectively. Reprint using Ref. [43]**

### 3.5 LiNbO<sub>3</sub> (LNO)

Among the many uses of lithium niobate crystals (LNO) in acoustic, optic, and optoelectronic devices, lithium niobate is an important dielectric and ferroelectric material. A few factors affect the physical and chemical properties of LNO, including its microstructure, defects, compositions, and dimensions. Liu et al. reported the fabrication of the RS device made of lithium niobate (LNO). The LNO is a potential candidate for RS and neuromorphic computing. The structure of the device consists of Ti/Pt/ LNO /Ti/Pt, where the switching layer of LNO was prepared by the PLD (Pulsed laser deposition) method [44]. There were 10 nm of titanium (Ti) and 50 nm of platinum (Pt) in the bottom electrode, whereas 10 nm of Ti and 80 nm of Pt were in the top electrode. The silicon substrate was used on which the 2  $\mu$ m layer of SiO was deposited by the PECVD method. In this structure, Ti is an active metal like Ag. Ti was used as the top electrode, which probably increased the movement of oxygen vacancies inside the layer, resulting in RS. A voltage between -3 V and 3 V was applied for most measurements, allowing for repeatable hysteresis loops. It exhibits a bipolar RS mechanism [45].

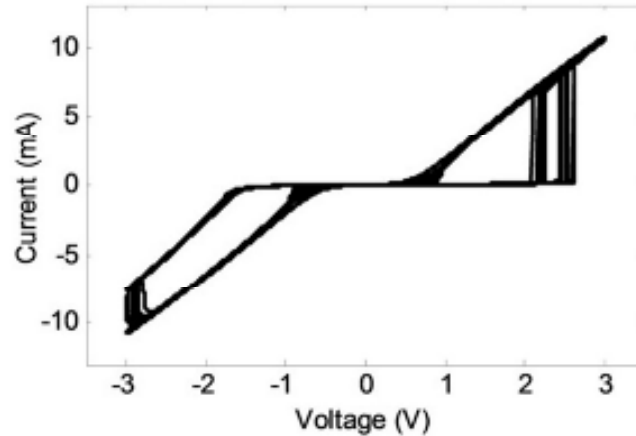


**Figure-8. I-V characteristic of a 15  $\mu\text{m}^2$  LiNiO<sub>3</sub> device. The many hysteresis loops show strong repeatability with a small amount of variation in the positive write voltage threshold Reprint using Ref. [46]**

**Table-2. State Of Art Comparison of Perovskite Oxides**

Structure	Deposition Technique	V <sub>SET</sub> (V)	V <sub>RESET</sub> (V)	Endurance (Cycles)	Retention (s)	Ref.
Pt/BTO/Pt	RF Magnetic Sputtering	10	-10	10 <sup>3</sup>	-	[47]
ZnO/BTO/ZnO	RF Magnetic Sputtering	1	-1	70	10 <sup>3</sup>	[48]
Pt/STO/Pt	RF Magnetic Sputtering	-1.35	1.9	10 <sup>6</sup>	10 <sup>5</sup>	[49]
Al/STO/Si	Pulsed Laser Deposition	5	-5	10 <sup>4</sup>	10 <sup>4</sup>	[50]
Pt/BSTO/NSTO	Hydrothermal	3	-6	10 <sup>2</sup>	1.8 X 10 <sup>3</sup>	[40]
Ag/BMO/Ti	Hydrothermal	4	-4	10 <sup>2</sup>	-	[41]
Ti/Pt/LNO/Ti/Pt	Pulsed Laser Deposition	3	-3	10 <sup>2</sup>	10 <sup>5</sup>	[46]

#### 4. CONCLUSION

This review article aims to offer a general outlook on the advancements in-memory technology, as well as the current trends that provide valuable intuition into the field of upcoming memory technology. We have presented a detailed discussion of RRAM, its structure, and the working mechanisms of RRAM. The current review also discusses RRAM operation based on the key performance parameters. Various important applications of RRAM have been highlighted, including non-volatile, neuromorphic computing. Furthermore, RRAM should be used more frequently in embedded memory and NVM technology because advances in these fields are much more interesting. RRAM devices will likely become an important non-volatile memory technology if they continue to be developed and improved. Memristor is a type of electronic component that can remember their previous

state and have the potential to be used for a wide range of applications such as memory storage, neuromorphic computing, and machine learning. Memristor have the potential to be integrated with other devices such as transistors and capacitors to form a new type of memory and computing systems. Researchers are actively developing new memristor designs with improved performance reliability and scalability. Memristors have the potential to be used in the development of new type of artificial neural networks and neuromorphic computing systems. As researchers continue to study the properties of memristors and develop new designs, the range of applications for memristors is likely to expand into new areas such as bio-inspired computing, autonomous systems, and the Internet of Things (IoT).

### **Declaration of competing interest**

The authors declare that they have no known competing financial interests or personal relationships that could have appeared to influence the work reported in this paper.

### **REFERENCES**

1. He S, Sun K, Peng Y, Wang L. (2020) AIP Advances, 10(1).
2. Chua LO. (1971) IEEE Transactions on Circuit Theory, 18(5), 507-519.
3. Duraisamy N, Muhammad NM, Kim HC, Jo JD, Choi KH. (2012) Thin Solid Films, 520(15), 5070-5074.
4. Strukov DB, Snider GS, Stewart DR, Williams RS. (2008) Nature, 453(7191), 80-83.
5. Domaradzki J, Wojcieszak D, Kotwica T, Mańkowska E. (2020) International Journal of Electronics and Telecommunications, 66(2), 373-381.
6. Munjal S, Khare N. (2020) 3Rd International Conference on Condensed Matter and Applied Physics (Icc-2019), 2220, 020171.
7. Goodman FJ, Martin AF, Wohlford RE. (1989) ICASSP, IEEE International Conference on Acoustics, Speech and Signal Processing - Proceedings, 1, 528-531.
8. Shen WC, Mei CY, Chih YD, et al. (2012) Technical Digest - International Electron Devices Meeting, IEDM, 745-748.
9. Mueller S, Slesazek S, Mikolajick T, Müller J, Polakowski P, Flachowsky S. (2015) IEEE International, 233-236.
10. Yang JJ, Zhang MX, Strachan JP, et al. (2010) Applied Physics Letters, 97(23), 12-15.
11. ITRS. International Roadmap Committee Overview. Published online 2013. <http://www.itrs.net/Links/2013ITRS/Summary2013.htm>
12. Song Z, Song S, Zhu M, et al. (2018) Science China Information Sciences, 61(8), 1-15.
13. Berdan R. (2016) Conventional Analogue Electronics. <https://spiral.imperial.ac.uk/bitstream/10044/1/43370/1/Berdan-R-2016-PhD-Thesis.pdf>
14. Hermes C, Wimmer M, Menzel S, et al. (2011) IEEE Electron Device Letters, 32(8), 1116-1118.
15. Zakaria O, Madi M, Kasugai S. (2020) Journal of Biomedical Materials Research - Part B Applied Biomaterials, 108(2), 460-467.
16. Mullani N, Ali I, Dongale TD, et al. (2020) Materials Science in Semiconductor

- Processing, 108, 104907.
17. Du X, Tadrous J, Sabharwal A. (2016) IEEE Transactions on Wireless Communications, 15(12), 8551-8564.
  18. Jamkhande PG, Ghule NW, Bamer AH, Kalaskar MG. (2019) Journal of Drug Delivery Science and Technology, 53, 101174.
  19. Prakash A, Jana D, Maikap S (2013) Nanoscale Research Letters, 8(1), 1-17.
  20. Menzel S. (2017) Journal of Computational Electronics, 16(4), 1017-1037.
  21. Baeumer C, Schmitz C, Marchewka A, et al. (2016) Nature Communications, 7, 1-7.
  22. Wang J. Aono Nat Mat 07 Ionic Switching Memory Nanoionics-based resistive switching memories.
  23. Waser R, Dittmann R, Staikov C, Szot K. (2009) Advanced Materials, 21(25-26), 2632-2663.
  24. Sawa A. (2008) Materials Today, 11(6), 28-36.
  25. Yao J, Zhong L, Natelson D, Tour JM. (2012) Scientific Reports, 2, 1-5.
  26. Devices F, Architectures A. Resistive Random Access Memory (RRAM).
  27. Beck A, Bednorz JG, Gerber C, Rossel C, Widmer D. (2000) Applied Physics Letters, 77(1), 139-141.
  28. Sawa A, Fujii T, Kawasaki M, Tokura Y. (2004) Applied Physics Letters, 85(18), 4073-4075.
  29. Fujii T, Kawasaki M, Sawa A, Akoh H, Kawazoe Y, Tokura Y. (2005) Applied Physics Letters, 86, 1-3.
  30. Sawa A, Fujii T, Kawasaki M, Tokura Y. (2005) Japanese Journal of Applied Physics, Part 2: Letters, 44(37-41), 6-9.
  31. Lanza M, Wong HP, Pop E, et al. (2018) Advanced Electronic Materials, 1800143, 1-28.
  32. Huang Y, Shen Z, Wu Y, Wang X, Zhang S. (2016) RSC Advances, 26, 17867-17872.
  33. Gupta V, Kapur S, Saurabh S, et al. (2019) IETE Technical Review, 0(0), 1-14.
  34. Bousoulas P, Stathopoulos S, Tsialoukis D, Tsoukalas D. IEEE Electron Device Letters, 37 (7), 874-877.
  35. Chang TC, Chang KC, Tsai TM, Chu TJ, Sze SM. (2016) Materials Today, 19(5), 254-264.
  36. Qian M, Fina I, Sánchez F, Fontcuberta J. (2019) Nano-micro Small, 1805042, 1-9.
  37. Linn E, Rosezin R, Kügeler C, Waser R. (2010) Nature Materials, 9(5), 403-406.
  38. Wang H, Zhang W, Xu J, Liu G, Xie H, Yang L. (2018) Bulletin of Materials Science, 41(6), 149.
  39. Bera A, Peng H, Lourembam J, Shen Y, Sun XW, Wu T. (2013) Advanced Functional Materials, 23(39), 4977-4984.
  40. Jing He, Jie Zhu, Changcheng Ma, Jingjing Lu, Zuoqi Hu. (2019) Applied Physics Letters, 115(7), 1-6.
  41. Acharya SA, Gaikwad VM, Kulkarni SK, Deshpande UP. (2017) Journal of Materials

- Science, 52(1), 458-466.
42. Sun B, Li CM. (2015) *Physical Chemistry Chemical Physics*, 17(10), 6718-6721.
  43. Lee BW, Yoo PS, Nam VB, Toreh KRN, Jung CU. (2015) *Nanoscale Research Letters*, 10(1), 1-5.
  44. Liu Y, Li J, Zhang Z, Kong Y. (2017) *Ferroelectrics*, 520(1), 34-41.
  45. Lapkin DA, Emelyanov A V., Demin VA, Berzina TS, Erokhin V V. (2018) *Microelectronic Engineering*, 185-186, 43-47.
  46. Wang S, Wang W, Yakopcic C, Shin E, Subramanyam G, Taha TM. (2017) *Microelectronic Engineering*, 168, 37-40.
  47. Pan RK, Zhang TJ, Wang JY, Wang JZ, Wang DF, Duan MG.(2012) *Thin Solid Films*, 520(11), 4016-4020.
  48. Wei L, Sun B, Zhao W, et al. (2016) *Modern Physics Letters B*, 30(14), 1-8.
  49. Nili H, Walia S, Balendhran S, Strukov DB, Bhaskaran M, Sriram S. (2014) *Advanced Functional Materials*, 24(43), 6741-6750.
  50. Song MY, Seo Y, Kim YS, et al. (2012) *Applied Physics Express*, 5(9). 091202

# Supercapacitive performance of chemically deposited CuO thin film

Suman A. Sawant<sup>a</sup>, Sunny R. Gurav<sup>a</sup>, Gayatri R. Chodankar<sup>a</sup>,  
Pradnya G. Raje<sup>a</sup>, Rajendra G. Sonkawade<sup>a,\*</sup>

<sup>a</sup>Department of Physics, Shivaji University, Kolhapur, Maharashtra, 416 004, India.

\*Corresponding author: rgs\_phy@unishivaji.ac.in

---

## ABSTRACT

Copper oxide (CuO)-based supercapacitors have gained considerable interest because they are inexpensive, ecologically benign and exhibit superior electrochemical performance. Herein, the synthesis and supercapacitive performance of nanoflakes-like CuO have been investigated. CuO thin films were synthesized by cost-effective and easy chemical bath deposition (CBD) method. The formation of monoclinic CuO was confirmed by an X-ray diffraction (XRD) pattern. Distribution of densely packed nanoflakes observed in the surface topographical image with an average roughness of CuO 91.66 nm. The hydrophilic nature of CuO thin films was revealed from water contact angle measurement. A nanocrystalline surface with hydrophilic nature helped for better electrochemical interactions. The electrochemical performance of CuO thin film was tested in 1M KOH and showed the specific capacitance ( $C_s$ ) of 340 F/g at a 5mV/s scan rate with small charge transfer resistance ( $R_{CT}$ ), energy density ( $Ed$ ), power density ( $Pd$ ) and coulomb efficiency ( $\eta$ ) of 3.23 $\Omega$ , 5 Wh/kg, 500 W/kg and 93.62%, respectively. These results show that this electrode will be a potential material in supercapacitor applications besides it is cost-effective.

## KEYWORDS

Copper Oxide, Energy Storage Device, Pseudocapacitor, Supercapacitor, Transition Metal Oxide.

.....

## 1. INTRODUCTION

The increase in global population and the rapid expansion of the modern economy required the use of energy resources to meet energy demands at a reduced cost. To fulfill the ever-growing demand for energy, many solutions are coming forward. On this context, supercapacitors (SCs) provide their candidature in the field of energy storage which bridges the gap between conventional capacitors and batteries [1].

Depending on the charge storage mechanism SCs are classified into two categories; first one is electric double layer capacitors (EDLCs) in which charge stored via electrostatic way and next is pseudocapacitors in which charge stored through faradic reactions. Carbon based materials shows EDLC type behavior whereas conducting polymers and metal oxides shows pseudocapacitive nature [2].

Till date various materials are studied for the SCs application. The properties of electrode material have a significant impact on the performance of SCs. Electrode materials with large surface area, great electrochemical stability, low toxicity, and high electrical conductivity have attracted a lot of interest [3]. Rigorous study has done on the most popular transition metal oxide  $\text{RuO}_2$  for pseudocapacitors due its large surface area and high conductivity. But the high cost and toxicity limit its commercial application [4]. Other cost effective and environmentally friendly metal oxides which exhibits better electrochemical properties are Nickel Oxide (NiO) [5], Manganese Oxide ( $\text{MnO}_2$ ) [3], and Copper Oxide (CuO) [2]. Among these, CuO gains lots of attention due to its easy synthesis, low cost, environmentally benign, and having higher electrical conductivity. CuO can be synthesized by different methods such as SILAR [6], hydrothermal [7], dip-coting method [8], and CBD [9]. Amongst, CBD is a most suitable technique for the synthesis of adherent, large area deposition without high-quality substrate and vacuum conditions at any stage. One can control the properties of prepared thin film by optimizing the deposition time, pH of solution, the temperature and concentration of precursors [9].

In present study, densely packed CuO nanoflakes were deposited on cost-effective stainless-steel substrates via simple CBD method. The CuO thin films were characterized using XRD, atomic force microscopy (AFM), Fourier transform infrared spectroscopy (FT-IR), Raman spectroscopy and surface wettability test. To study the electrochemical properties of CuO thin films, cyclic voltammetry (CV), galvanostatic charge discharge (GCD), and electrochemical impedance spectroscopy (EIS) methods were employed. Nanoflake-like form of CuO might be advantageous for electrochemical reactions and showed good supercapacitive performance. This nanoflake-like CuO thin film with no conducting additives or binder demonstrated promising capacitive capabilities.

## **2. EXPERIMENTAL SECTION**

### **2.1. Materials**

Chemicals like copper sulphate ( $\text{CuSO}_4 \cdot 5\text{H}_2\text{O}$ ) and ammonium hydroxide ( $\text{NH}_4\text{OH}$ ), and double distilled water (DDW) were used which were purchased from Thomas baker. None of the compounds underwent additional purification before usage.

## 2.2. Synthesis of CuO thin film

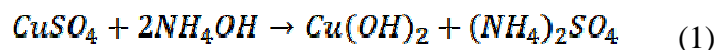
In the present work, CuO thin films were synthesized by cost-effective CBD method. Heterogeneous reactions are the basis for the synthesis of CuO via CBD method. When the solution reaches its maximum level of supersaturation, the ionic product exceeds the solubility product, which triggers the development of atomic nuclei and the deposition of the film. The preparative parameters used for the synthesis of CuO thin films are listed in **Table-1**.

**Table-1. Preparative Parameters of CuO thin film**

Preparative parameters	
Precursor	0.1M CuSO <sub>4</sub>
Complexing Agent	NH <sub>4</sub> OH
Substrate	Stainless steel
pH of Solution	12
Deposition Time	2hr
Deposition Temperature	80°C

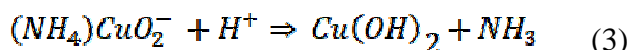
For the deposition of CuO, stainless steel substrates are used. Before deposition, substrates were cleaned using polish paper with successive washing and cleaning with DDW and acetone. Firstly, 0.1 M CuSO<sub>4</sub> solution was prepared in DDW. Then to make alkaline solution, aqueous ammonia was added drop by drop until the pH maintained at ≈12. Then the clean stainless-steel substrates were immersed in above prepared solution which is kept on constant temperature bath at 80°C for 2hr. Then as reaction goes precipitation starts and through heterogeneous reactions deposition takes place on substrates. In an alkaline bath initially formation of *Cu(OH)<sub>2</sub>* occurs and finally convert into CuO by annealing at 200°C for 2 Hrs.

The possible reaction mechanism involved in this process is given below:  
when ammonia is added to it,





When this solution was heated,



### 2.3. Characterizations

For the structural characterization, Bruker D8 Advanced X-ray diffractometer of Cu-K $\alpha$  Radiation with 1.54 Å wavelength was used for the study of XRD pattern of CuO electrodes. Perkin Elmer Spectrophotometer (4000-360 cm<sup>-1</sup>) were used for the study of FT-IR and Raman spectroscopy, respectively. However, NX-10 Bio-AFM was used for the study of topography. For electrochemical characterization three electrode system was used, where the CuO electrode, Platinum (Pt), and saturated calomel electrode (SCE) were used as working, counter, and a reference electrode, respectively. The whole assembly is immersed in 1M KOH electrolyte. Electrochemical workstation (Model: BioLogic vmp3 Potentiostat) was used for the CV, GCD and EIS study. From CV, GCD and EIS plot C<sub>s</sub>, E<sub>d</sub>, P<sub>d</sub>, g and R<sub>CT</sub> of CuO electrodes were calculated.

### 3. RESULTS AND DISCUSSION

XRD pattern of as prepared CuO thin film is shown in **Figure-1a**. The peaks observed in XRD pattern are well matched with ICDD card no. 00-048-1548 showed polycrystalline nature with pure monoclinic structure without presence of any impurity peak of CuOH and Cu(OH)<sub>2</sub>. The peaks denoted by star sign are due to stainless steel substrate. Obtained values of lattice constants for CuO are a = 0.46883 Å, b = 0.34229 Å, c = 51319 Å, and  $\beta = 99.05^\circ$  with unit cell volume 81.22 Å<sup>3</sup>. For  $2\theta = 35.5^\circ$  corresponding to (002) plane, FWHM is found to be 0.66041° and calculated value of crystalline size using Debye-Sharrer's formula is 12.6 nm. Additionally, interplanar distance (d), microstrain ( $\epsilon$ ), dislocation density, and distortion parameters are calculated and listed in **Table-2**.

**Figure-2b** represents the FT-IR spectrum of CuO recorded in range of 400-4000 cm<sup>-1</sup>. The dominate peak at 502 cm<sup>-1</sup> is associated with the Cu-O bond which confirms the formation of CuO. The peak observed at 1114, 1383, 1635, 2935 and 3435 cm<sup>-1</sup> corresponds to the C-NH<sub>2</sub> primary aliphatic amine, -COO carboxylic acid, C=O stretching, alkane C-H stretching mode, and OH stretching respectively [10]. Raman spectrum of CuO thin film recorded in the range of 100 to 1000 cm<sup>-1</sup> is shown in **Figure-3c**. In Raman spectrum, the peaks observed at 296, 329, and 610 cm<sup>-1</sup>. Among the optical branches which theoretically expected in the Raman spectrum (4Au + 5Bu + Ag + 2Bg) of CuO, three modes (Ag + 2Bg) are Raman active. The peaks observed at 296, 329, and 610 cm<sup>-1</sup> represents the first order phonon

scattering corresponding to Ag mode, Bg mode, and Bg mode, respectively, which confirms the formation of CuO [11,12].

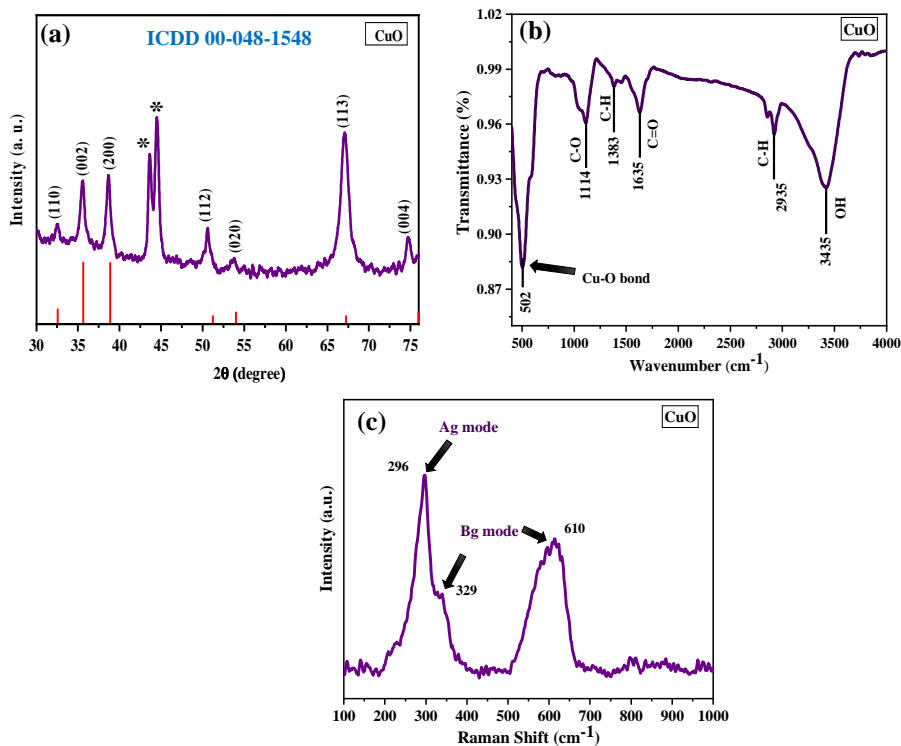


**Figure-1. a) XRD pattern of CuO thin film, b) FT-IR spectra of CuO thin film, and (c) Raman plots of CuO thin film.**

**Table-2. The XRD Parameters of CuO thin film.**

XRD parameters						
2θ (degree)	FWHM (β) (degree)	Crystalline Size (D) (nm)	Interplanar distance (d) (nm)	Strain (ε)	Dislocation Density (m <sup>-2</sup> )	Distortion Parameter (g)
35.5	0.66041	12.6	0.2346	0.41	6.26749E+15	0.036009463

Surface topological images of CuO thin films were studied using AFM. **Figure-4** shows 2D and 3D topography of CuO thin film with line profile. Images

show the distribution of densely packed CuO nanoflakes all over the substrate [13]. Nanoflakes having nearly  $0.426\ \mu\text{m}$  of size with  $0.121\ \mu\text{m}$  thickness. The measured

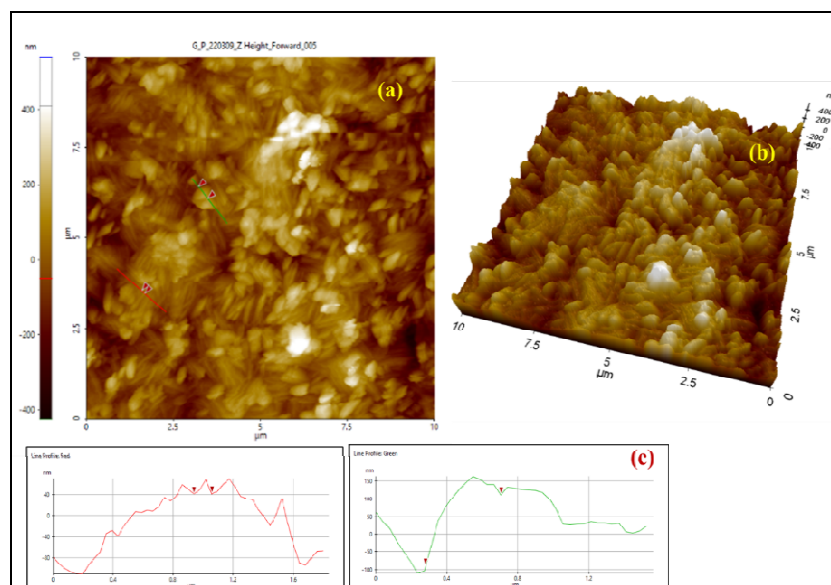


**Figure-2. (a) 2D and (b) 3D topographical images of CuO thin films, (c) line profile.**

average roughness value obtained as  $91.966\ \text{nm}$ . The rough surface densely covered by nanoflakes benefits application by exposing maximum active surface for the good electrochemical interaction between CuO and electrolyte.

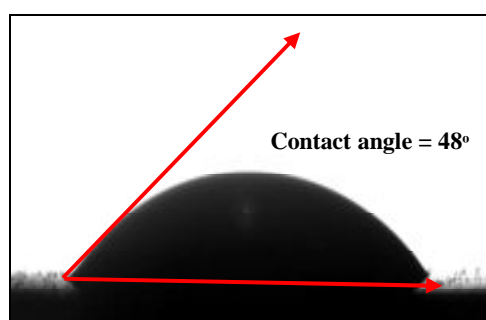


**Figure-3. Contact angle measurement of CuO thin film.**

While investigating electrochemical properties, in order to check hydrophilicity of electrode in aqueous electrolyte water contact angle measurements are mandatory. For the electrochemical application, interaction between electrode and electrolyte is highly dependent on surface wettability of electrode [2]. As the wettability of electrode is higher in electrolyte, electrochemical interactions taken

place at electrode electrolyte interface increases which improves the charge storage. To study the surface wettability, contact angle measurement is taken. CuO thin film showed hydrophilic nature with water contact angle of 48° as shown in **Figure-5**. Hydrophilicity is related to the nanocrystalline nature of material [14]. Prepared hydrophilic CuO thin film with nanocrystalline structure gives better wettability to the aqueous electrolyte solution used for SCs application.

### 3.1. Electrochemical Performance

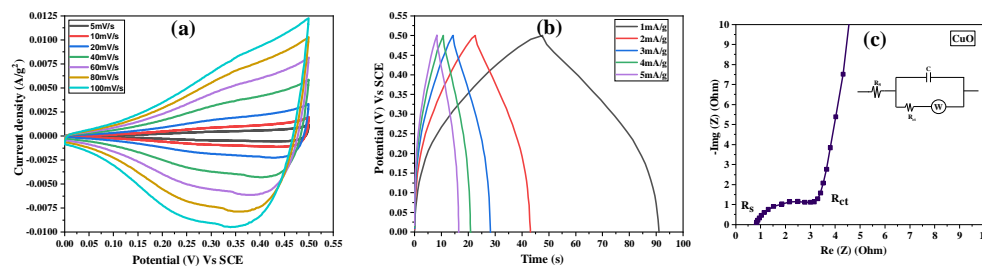


**Figure-4.** (a) CV, (b) CD, and (c) Nyquist plot of CuO carried out in 1M KOH.

**Figure-4** shows the CV, GCD and Nyquist plots of CuO thin film. CV plot of CuO thin film carried out in 1M KOH electrolyte between 0-0.5 V potential window is given in **Figure-6a**. The CV curves are not ideal rectangular type which reveals the pseudocapacitive behavior of CuO i.e., here charge is stored faradaically [14]. Redox peaks observed in CV curve are due to oxidation-reduction of  $\text{Cu}^+$  and  $\text{Cu}^{2+}$ . CV scanned at various scan rates from 5-100 mV/s scan rate and shows the increasing current density of CV curve with increasing scan rate. Capacitance (C) and  $C_s$  of electrodes is calculated by the following formulae:

$$C = \frac{I_{max}}{\frac{dV}{dt}} \text{----- (4)}$$

$$C_s = \frac{\frac{I_{max}}{\frac{dV}{dt}}}{M} \text{----- (5)}$$

Where,  $I_{max}$  - average current,  $dV/dt$  - scanning rate, M - the mass difference of electrode.

The highest specific capacitance obtained for the CuO thin film is 340 F/g at 5 mV/s scan rate. With increasing scan rate specific capacitance decreased from 340 F/g to 93 F/g. This drop in capacitance is due to at low scan rate, the ions get sufficient time to interact with / adsorb on active material and the electrode is fully

charged and discharged during cycling which in turn result into higher value of specific capacitance and vice versa. Consequently, at high scan rate the electrolyte ions are adsorbed only at the outer surface of the electrode due to slower transfer of ions that leads lower specific capacitance [15].

GCD plot of CuO thin film carried out in 1M KOH electrolyte between 0-0.5 V potential window at different current densities from 1 mA/g to 5 mA/g is given in **Figure-4b**. Non-linear nature of GCD curves represents the pseudocapacitive contribution of CuO [15]. The symmetric nature of charging – discharging curves is the indication of the suitability of CuO for supercapacitor application. The following formulae is used for the calculation of  $C_s$ ,  $E_d$ ,  $P_d$  and  $\eta$  and the obtained results are summarised in **Table-3**.

$$C_s = \frac{It_d}{m\Delta V} \text{ -----(6)}$$

$$E_d = \frac{0.5 + C_s \Delta V \Delta V}{3.6} \text{ -----(7)}$$

$$P_d = \frac{S.E. * 3600}{t_d} \text{ -----(8)}$$

$$\eta = \frac{t_d}{t_c} * 100 \text{ -----(9)}$$

The specific capacitance obtained for the CuO thin films is 176 F/g at 1 mA/g current density. It was found that with increasing scan rate specific capacitance was decreased due to diffusion of electrolyte [1].

EIS measurements were carried out in 1 M KOH electrolyte between 1 mHz to 1MHz frequency range fitted with equivalent circuit inside **Figure-4c**. **Figure-4c** shows the Nyquist plot of CuO thin film in which in high frequency region semicircle was observed which is due to faradic reactions. Where as in low frequency region straight line is observed due to diffusion of electrolyte ions [1]. The value of  $R_s$  and  $R_{CT}$  obtained for CuO are 0.79 and 3.23  $\Omega$ . The cycling stability of a CuO electrode is studied in 1 M KOH at a scan rate of 100 mV/s for 1000 CV cycles. **Figure-5** depicts the capacitance retention of a CuO electrode from the first to the 1000<sup>th</sup> CV cycle. The plot of the first, 1000<sup>th</sup> CV cycles is shown in the inset of **Figure-5**. After 1000 CV cycles, the capacity retention for CuO thin films is determined to be 67%. The loss in stability after 1000 CV cycles is attributed to structural collapse, active material deterioration during CV cycles, and active material dissolving into the KOH electrolyte. Surface roughness with hydrophilic nature of CuO thin film promoted the better electrochemical interactions between electrode and electrolyte solution. This lead to obtain higher specific capacitance with low charge transfer resistance.

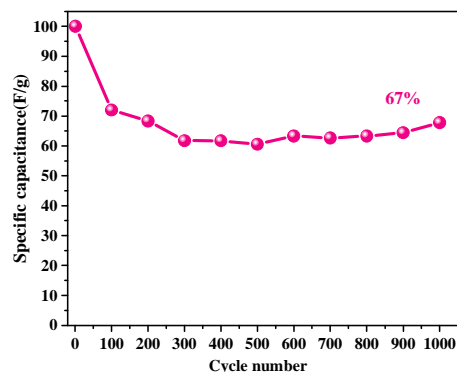


**Figure-5. Cyclic stability of CuO carried out in 1M KOH.**

**Table-3. Electrochemical performance of CuO**

Electrochemical results	
Current density (mA/g)	1
Specific capacitance (F/g)	176
Energy density (Wh/Kg)	5
Power density (W/Kg)	500
Coulomb efficiency (%)	93.62

#### 4. CONCLUSION

CuO thin films were successfully synthesized by cost effective CBD method. Pure monoclinic structure of polycrystalline CuO is confirmed by XRD analysis. Additionally, synthesis of CuO was confirmed from FTIR and Raman spectroscopy. Distribution of densely packed nanoflakes all over the surface observed in surface topographical image. Measured water contact angle measurements revealed hydrophilic nature of CuO thin films, which attributed to the nanocrystalline structure. The combination of rough, nanocrystalline and hydrophilic surface promoted good electrochemical interactions. Electrochemical measurements showed the CuO thin film displayed pseudocapacitive characteristics with maximum specific capacitance of 340 F/g at 5m V/s scan rate and energy density of 5 Wh/ kg, power density 500 W/kg and Coulomb efficiency of 91% obtained at 1 mA/g current density.

## ACKNOWLEDGMENT

Author Suman A. Sawant thankfully acknowledged the financial support provided Chhatrapati Shahu Maharaj Research Training and Human Development Institute (SARTHI), Pune (2019). The authors are thankful to the PIFC center, Department of Physics, Shivaji University, Kolhapur for providing contact angle measurement facility. The financial assistance through DST PURSE-Phase II (2018- 2022) & UGC DSA-Phase II (2018-2023) is highly acknowledged.

## REFERENCES

1. Waikar, M. R., Shaikh, A. A., Sonkawade, R. G. (2019) *Polymer Bulletin*, 76, 4703–4718.
2. Waikar, M.R., Shaikh, A. A., Sonkawade, R. G. (2019) *Vacuum*, 161, 168–175.
3. Shaikh, A. A., Waikar, M. R., Sonkawade, R. G. (2019) *Synthetic Metals*, 247, 1–9.
4. Shaikh, A. A., Waikar, M. R., Sonkawade, R. G. (2019) *Journal of Electronic Materials*, 488116–8128.
5. Dhas, S. D., Maldar, P. S., Patil, M. D., Nagare, A. B., Waikar, M. R., Sonkawade, R.G., Moholkar, A. V., (2020) *Vacuum*, 181, 109646.
6. Daoudi, O., Qachaou, Y., Raidou, A., Nouneh, K., Lharch, M., Fahoume, M. (2019) *Superlattices Microstructures*, 127, 93–99.
7. Sonia, S., Poongodi, S., Kumar, P.S., Mangalaraj, D., Ponpandian, N., Viswanathan C. (2015), *Materials Science in Semiconductor Processing*, 30, 585–591.
8. Martínez-Saucedo, G., Castanedo-Pérez, R., Torres-Delgado, G., Mendoza-Galván, A., Ángel, O.Z. (2017) *Materials Science in Semiconductor Processing*, 68, 133–139.
9. Sultana, J., Paul S., Karmakar, A., Yi R., Dalapati, G.K., Chattopadhyay, S. (2017) *Applied Surface Science*, 418, 380–387.
10. Sukumar, S., Rudrasenan, A., Nambiar, D. P., *ACS Omega*, (2019) 5 1040–1051.
11. Akgul, F. A., Akgul, G., Yildirim, N., Unalan, H. E., Turan, R. (2014), *Materials Chemistry and Physics*, 147, 987–995.

12. Hao, Y., Teja, A. S. (2014) *Journal of Nanomaterials*, 0100, 415–422.
13. Dhanasekaran, V., Mahalingam, T., Ganesan, V. (2013) *Microscopy Research and Techniques*, 76 58–65.
14. Dubal, D. P., Dhawale, D. S., Salunkhe, R. R., Jamdade, V. S., Lokhande, C.D. (2010) *Journal of Alloys and Compounds*, 492, 26–30.
15. Yan, J., Liu, J., Fan, Z. (2012) *Carbon*, 50, 2179–2188.

# SILAR Prepared Mn<sub>3</sub>O<sub>4</sub> Thin Film for Supercapacitor Application

Sunny R. Gurav<sup>a</sup>, Gayatri R. Chodankar<sup>a</sup>, Suman A. Sawant<sup>a</sup>, and Rajendra G. Sonkawade<sup>a,b,\*</sup>

<sup>a</sup>Department of Physics, Shivaji University, Kolhapur 416 004 (MS) India.

<sup>b</sup>Department of SAIF-CFC, Shivaji University, Kolhapur 416 004 (MS) India.

\*Corresponding author: rgs\_phy@unishivaji.ac.in

---

---

## ABSTRACT

*Mn<sub>3</sub>O<sub>4</sub> is a significant possibility for a multitude of applications. The Mn<sub>3</sub>O<sub>4</sub> thin film was successfully prepared utilising Successive Ionic Layer Adsorption and Reaction (SILAR) method in this research work. Systematic evaluations were carried out to confirm the morphology and structural properties of the Mn<sub>3</sub>O<sub>4</sub> materials. In an electrochemical system, spherical Mn<sub>3</sub>O<sub>4</sub> grains that are well spaced and well-connected could promote greater electrolyte penetration and fill the ion buffer reservoir to ensure a steady supply of electrolyte. The Mn<sub>3</sub>O<sub>4</sub> thin film showed good specific capacitance (C<sub>s</sub>) of 106 F/g at 5 mV/s and 62 F/g at 1 mA/cm<sup>2</sup> in 1M Na<sub>2</sub>SO<sub>4</sub> electrolyte. The developed Mn<sub>3</sub>O<sub>4</sub> thin film exhibits incredible energy density (E<sub>d</sub>) and power density (P<sub>d</sub>) values of 5.54 Wh/Kg and 800 W/Kg, respectively. The Mn<sub>3</sub>O<sub>4</sub> thin film achieve a lower value of R<sub>s</sub> and R<sub>ct</sub> as 1.44 and 0.98 Ω and it has a capacity retention rate of 99% after 1000<sup>th</sup> CV cycles at 100 mV/s scan rate. With the help of this work, high performance electrochemical SCs can be produced directly by manufacturing a thin film of Mn<sub>3</sub>O<sub>4</sub>.*

## KEYWORDS

*Energy Storage Device, Microsphere, Mn<sub>3</sub>O<sub>4</sub>, SILAR, Pseudocapacitor, Supercapacitor.*

.....

## 1. INTRODUCTION

Fossil fuels are being used carelessly, which has led to large CO<sub>2</sub> emissions that have contributed to global warming and other serious environmental and health problems. The rapid growth of the world's population, the depletion of fossil fuels, and the scarcity of traditional energy sources have resulted in a shift to the usage of renewable energy sources such as hydro, solar energy, wind, tidal, and energy storage devices (ESDs) [1,2]. But right now, renewable energy sources like wind, solar, and others are insufficient. Additionally, because the majority of these energy production and conversion paths are irregular, they require the appropriate storage options in order to replace fossil fuels. Significant research efforts over the past three decades have sparked the development of modern electrochemical energy storage technologies including batteries and SCs. Compared to batteries and capacitors, SCs have longer life cycles and high Pd, as well as extremely quick charge and discharge rates. SCs have already been used in the industrial sector, especially in constant power systems, electric trains, vehicles, and elevators [3,4].

The characteristics of the electrode materials have a significant impact on how well a SCs performs. Depending on what type of electrode, SCs are divided into 2: pseudocapacitors, which store energy through quick Faradaic reactions at the electrode surface, and electrochemical double layer capacitors (EDLCs), which rely on the

accumulation of electrostatic charges at the electrode and electrolyte interaction [2,5]. The capacitance of pseudocapacitors can be 10 to 100 times more than the capacitance of EDLCs under the same electrode area, implying that they have a greater potential for development [6]. Till now, among metal oxides,  $\text{RuO}_2 \cdot x\text{H}_2\text{O}$  provides a superior electrochemical behaviour or pseudocapacitors; nevertheless, the massive prices, toxicities, and unavailability of its raw resources restrict its practical utilisation. As a result, there has been a surge of attention in designing commercially viable, attractive transition-metal oxide (TMO) electrodes like  $\text{Mn}_3\text{O}_4$ ,  $\text{NiO}$ ,  $\text{Co}_3\text{O}_4$ ,  $\text{V}_2\text{O}_5$ ,  $\text{Fe}_3\text{O}_4$ ,  $\text{Bi}_2\text{O}_3$ ,  $\text{IrO}_2$ ,  $\text{NiFe}_2\text{O}_4$ , and  $\text{BiFeO}_3$ , and others. Manganese oxide materials stand out among them for their exceptional structural flexibility together with excellent physical and chemical properties, making them extremely important in application areas including catalysis and rechargeable batteries. There are various crystal forms of manganese oxide, so it is crucial to the charge storage mechanism [7–9].

$\text{Mn}_3\text{O}_4$  has been used as a working electrode for ESDs due to its high specific capacity, variable structure and shape, and wide availability. Compared to other conventional electrode materials, it has attracted considerable attention for energy storage applications because of its greater manganese valence, higher theoretical capacitance value, abundance in nature, simple manufacturing process, outstanding environmental compatibility, superior electrochemical performance, and diversified structure [9]. Luo et al. [10] synthesized  $\text{Mn}_3\text{O}_4$  cubes interlocked with each other for SCs application. At scan rates of 1 mV/s and low current densities of 1 A/g, the  $\text{Mn}_3\text{O}_4$  electrode exhibits maximum  $C_s$  of 667 F/g and 583 F/g, respectively. Through the use of a modified solvothermal process, Qiao et al. [11] fabricated porous  $\text{Mn}_3\text{O}_4$  with micro/nano-structure. The porous  $\text{Mn}_3\text{O}_4$  employed as a SCs electrode showed great electrochemical properties, with a comparatively high  $C_s$  value of 302 F/g at a low current density of 0.5 A/g, with high-rate dischargability (246 F/g, 81% capacity retention when the current densities are increased by 10 times (5 A/g), and good cycling stability (89% retention after 5000<sup>th</sup> charge/discharge cycles at 5 A/g). The  $\text{Mn}_3\text{O}_4$  thin films were synthesized using the SILAR technique by Dubal et al. [12]. The highest  $C_s$  of the  $\text{Mn}_3\text{O}_4$  thin film supercapacitive capabilities in 1M  $\text{Na}_2\text{SO}_4$  electrolyte was 314 F/g at scan rate 5 mV/s. In light of these factors, in this article we presented a  $\text{Mn}_3\text{O}_4$  thin films for SCs application via SILAR method.

## 2. EXPERIMENTAL DETAILS

### 2.1 Synthesis of $\text{Mn}_3\text{O}_4$ material

The SILAR method is employed to synthesize  $\text{Mn}_3\text{O}_4$  thin film on a stainless steel (SS) substrate using a manganese acetate as a cationic precursor. Double distilled water (DDW) was employed as the solvent and the AR grade chemicals acquired from Thomas Baker were used without further purification. In a typical process, 50 ml of 0.1 M manganese acetate was employed as a cationic precursor and 50 ml of 1 M sodium hydroxide (NaOH) was employed as an anionic precursor to deposit pure  $\text{Mn}_3\text{O}_4$  thin film.  $\text{Mn}_3\text{O}_4$  electrodes were grown on SS substrates that were  $1 \times 5 \text{ cm}^2$  in size. The surfaces of SS substrates were well cleaned with acetone cleaned after being properly polished with 320-grade silicon carbide paper. Furthermore, experimental work was conducted on properly cleaned stainless steel substrates. The SS substrate was immersed in manganese acetate solutions for 22 seconds to deposit  $\text{Mn}^{2+}$  ions, and for the next 11 seconds, it was washed with DDW to remove any loosely bound  $\text{Mn}^{2+}$  ions. In order to build a layer of manganese oxide, the SS substrate was dipped in the anionic solution (which contained the NaOH solution) for 22 seconds. The substrate

was then rinsed in DDW for 11 seconds. The completion of this single SILAR cycle process takes place at room temperature. 140 SILAR cycles were performed to get the  $\text{Mn}_3\text{O}_4$  thin film to the proper and consistent thickness.

## 2.2 Characterization of $\text{Mn}_3\text{O}_4$ material

The  $\text{Mn}_3\text{O}_4$  sample was characterized by various characterization techniques such as structural, morphological, surface wettability, and functional group detection. The identification of the structure and phase determination of  $\text{Mn}_3\text{O}_4$  material were studied through X-ray diffractometer [Model Bruker D8-Advance: phaser with  $\text{Cu K}\alpha$  radiation ( $\lambda = 1.5406 \text{ \AA}$ )]. Surface morphology was studied from Scanning Electron Microscopy (SEM), JEOL-6360, Japan. Fourier Transform Infrared (FT-IR) spectra of  $\text{Mn}_3\text{O}_4$  samples were recorded on Perkin Elmer FT-IR Spectrophotometer ( $4000\text{--}360 \text{ cm}^{-1}$ ) with KBr as compressed slices to realize the nature of bonds. Surface wettability test was studied from Contact Angle (CA) measurement instrument. The electrochemical performance was investigated through EC lab (Potentiostat) instrument.

## 3. RESULTS AND DISCUSSION

As-prepared  $\text{Mn}_3\text{O}_4$  thin film exhibits a typical XRD pattern in **Figure-1**, which suggests that the final product is almost X-ray weakly crystalline form. A weakly crystalline form of  $\text{Mn}_3\text{O}_4$  thin film is thought to result from the low temperature of the synthesis. The XRD pattern is

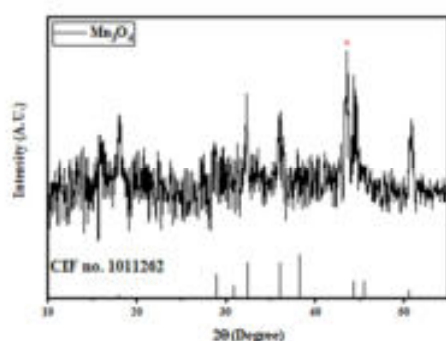


**Figure-1.** XRD pattern of  $\text{Mn}_3\text{O}_4$  thin film.

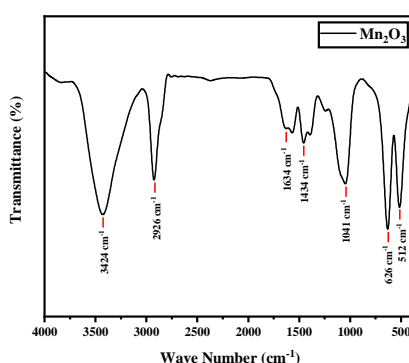


**Figure-2.** FT-IR spectrum of  $\text{Mn}_3\text{O}_4$

very well matches with the *CIF no. 1011262*. Whereas, the reflections observed at  $2\theta$  values  $44^\circ$  is corresponds to SS substrate, which indicated by \* [7,13]. The FT-IR spectrum is captured in order to confirm the bonding properties of the  $Mn_3O_4$  materials shown in **Figure-2**. Peaks at 3424, 1634, 1448, 1040, 626, and 512  $cm^{-1}$  are attributable to different bonding types between  $Mn_3O_4$  and surface-absorbed water molecules, respectively. The stretching and bending vibrations of molecule O-H are relevant for the IR bands at 3424, 2930, and 1634  $cm^{-1}$ . While the peaks at 1434 and 1041  $cm^{-1}$  signify the combined bending vibrations of the Mn atoms with the -OH groups. Two sharp IR bands are seen at 626 and 512  $cm^{-1}$ , which reflect the stretching vibrations of Mn-O units and the asymmetric Mn-O-Mn stretching; hence, the formation of  $Mn_3O_4$  may be understood [14-16].

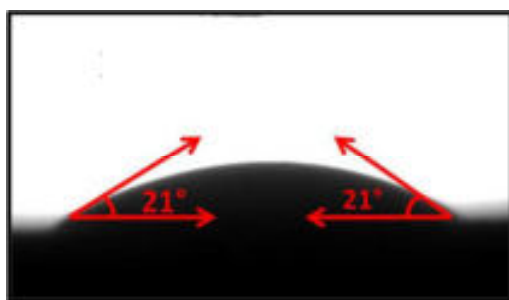


**Figure-3. Surface wettability test of  $Mn_3O_4$  thin film.**

In SCs applications, surface wettability is critical. In order to investigate how water interacts with the  $Mn_3O_4$  thin film, a wettability study was conducted [17]. **Figure-3** (with digital image) depicts the CA value of water droplets on the  $Mn_3O_4$  nanoplate electrode surface. The CA of a  $Mn_3O_4$  electrode with a water drop is  $21^\circ$ , which indicates that  $Mn_3O_4$  surface has a hydrophilic nature. Because of their hydrophilic nature, aqueous electrolytes can make good contact with the electrode surface in electrochemical applications. It is obvious that the hydrophilic surface of the electrode material in SCs applications is a crucial aspect for improved performance [18,19]. SEM has been used to investigate the surface morphology research of  $Mn_3O_4$  thin film. Spherical and polygonal grains have been seen in the SEM image of  $Mn_3O_4$  thin film as shown in **Figure-4a**. Additionally, it is shown that the particles were agglomerated, as well-connected, uniformly dispersed spherical grains with increased porosity were revealed. Electrolyte ions can access a high number of microscopic pores in a  $Mn_3O_4$  thin film, increasing the electrode's ability to store charges [7]. **Figure-4b** shows the histogram of grain size of  $Mn_3O_4$  material. The approximately average grain size of  $Mn_3O_4$  is 375 nm.

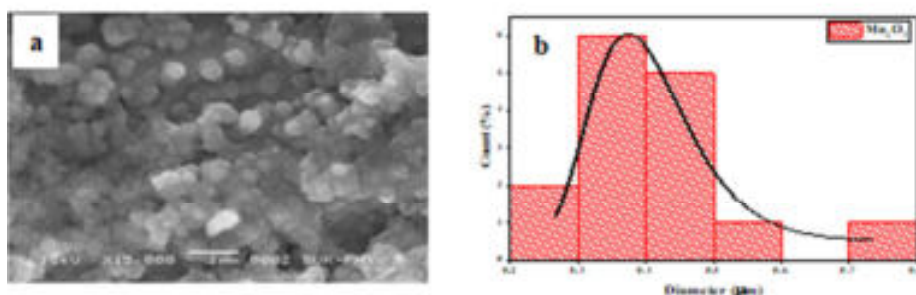


**Figure-4. a) SEM image of Mn<sub>3</sub>O<sub>4</sub> thin film and b) histogram of grain size of the Mn<sub>3</sub>O<sub>4</sub>.**

### 3.1 Electrochemical Study

Through CV and GCD analysis, the SCs performance was assessed in 1M Na<sub>2</sub>SO<sub>4</sub> electrolyte. The CV curve of the Mn<sub>3</sub>O<sub>4</sub> thin film is shown in **Figure-5a** at scan rates of 5, 10, 25, 50, 75, and 100 mV/s. The curves show a redox peak, which suggests that the thin Mn<sub>3</sub>O<sub>4</sub> thin film exhibits pseudocapacitor behaviour due to the faradic redox processes. The capacitance behaviour of the working electrodes is represented by the area of the CV curve. Thus, it is evident that the area of the curve rises with increasing scan rate (**Figure-5a**). However, when the scan rate rises, the C<sub>s</sub> of the Mn<sub>3</sub>O<sub>4</sub> thin film drops. This is because at high scan rates, there is inadequate intercalation and deintercalation at the electrode-electrolyte interface. Therefore, with a scan rate of 5, 10, 25, 50, 75, & 100 mV/s, respectively, maximum C<sub>s</sub> values of 106, 77, 51, 36, 28, & 23 F/g have been achieved. According to the **Equation-1**, the C<sub>s</sub> value of the Mn<sub>3</sub>O<sub>4</sub> thin film was estimated from CV curves [7,20].

$$C_s = \frac{\int_{v_1}^{v_2} I(V)dv}{m*v*\Delta v} \quad (1)$$

Whereas,  $\int_{v_1}^{v_2} I(V)dv$ - area under the CV curve, m - the mass of deposited material in grams,  $\Delta v$  is a potential window in V/SCE. Furthermore, the C<sub>s</sub>, P<sub>d</sub>, and E<sub>d</sub> of the Mn<sub>3</sub>O<sub>4</sub> thin film were examined by GCD analysis.

Current Density (mA/cm <sup>2</sup> )	Cs (F/g)	Ed (Wh/kg)	Pd (W/kg)
1	62.35	5.54	800
2	35.35	3.14	1600
3	26.85	2.38	2400
4	20.10	1.78	3200

**Table-1: - The estimated values of Cs, Pd, Ed, and  $\eta$**

As depicted in **Figure-5b**, the non-linearity of the GCD curves further supports the Mn<sub>3</sub>O<sub>4</sub> thin film's pseudocapacitive character, which is consistent with the findings from CV curves. The GCD curves, which are shown in **Table-1**, were used to estimate the values of the C<sub>s</sub>, P<sub>d</sub>, and E<sub>d</sub>. The values of C<sub>s</sub> and E<sub>d</sub> decrease as the current increases; as a result, the current density at 2 mA/cm<sup>2</sup> exhibits the maximum SCs performance of Mn<sub>3</sub>O<sub>4</sub> thin film. The following equations 2, 3, and 4 respectively, are used to calculate the C<sub>s</sub>, E<sub>d</sub>, and P<sub>d</sub> [20].

$$C_s = \frac{It_d}{m\Delta V} \quad (2)$$

$$E_d = \frac{0.5*C_s*\Delta V*\Delta V}{3.6} \quad (3)$$

$$P_d = \frac{S.E.*3600}{t_d} \quad (4)$$

where m is the mass of the deposition in grammes, t<sub>d</sub> is the discharge time in seconds, t<sub>c</sub> is the charging time in seconds, V is a potential window in V/SCE, and I is the discharge

current in mA. In addition to CV and CD, the frequency dependence and resistance provided by the  $\text{Mn}_3\text{O}_4$  thin film is investigated using EIS analysis in the frequency range of 1 Hz to 1 MHz. **Figure-5c** depicts Nyquist plots for  $\text{Mn}_3\text{O}_4$  thin film. It is observed that  $\text{Mn}_3\text{O}_4$  thin film achieve a lower value of  $R_s$  and  $R_{ct}$  as 1.44 and 0.98  $\Omega$ . Thus, the  $\text{Mn}_3\text{O}_4$  thin film exhibits superior SCs performances due to their low value of  $R_s$  and  $R_{ct}$ , which signifies the rapid charge transfer mechanism during the charging or discharging cycle. Furthermore, the cyclic stability of  $\text{Mn}_3\text{O}_4$  thin film is examined for 1000<sup>th</sup> cycles using CV measurement in 1M  $\text{Na}_2\text{SO}_4$  electrolyte at a 100 mV/s scan rate (**Figure-5d**). It is apparent that there is a dramatic increase in the  $C_s$  by 14% after 250<sup>th</sup> cycles to that of 1<sup>st</sup> cycle, which is attributed to the increase in the material's active site. Furthermore, after the 500<sup>th</sup>, 750<sup>th</sup>, and 1000<sup>th</sup> cycles, it decreases by 6, 6, and 3% to that of the 250<sup>th</sup>, 500<sup>th</sup> and 750<sup>th</sup> cycles respectively. This decrement in capacity retention between 250<sup>th</sup> to 1000<sup>th</sup> CV cycles is due to a large amount of material active sites material loss during the stability test. The prepared  $\text{Mn}_3\text{O}_4$  thin film has a capacity retention rate of 99% after 1000<sup>th</sup> CV cycles. Hence, the aforementioned study confirms the stable nature of a  $\text{Mn}_3\text{O}_4$  thin film and it is a suitable candidate for SCs.

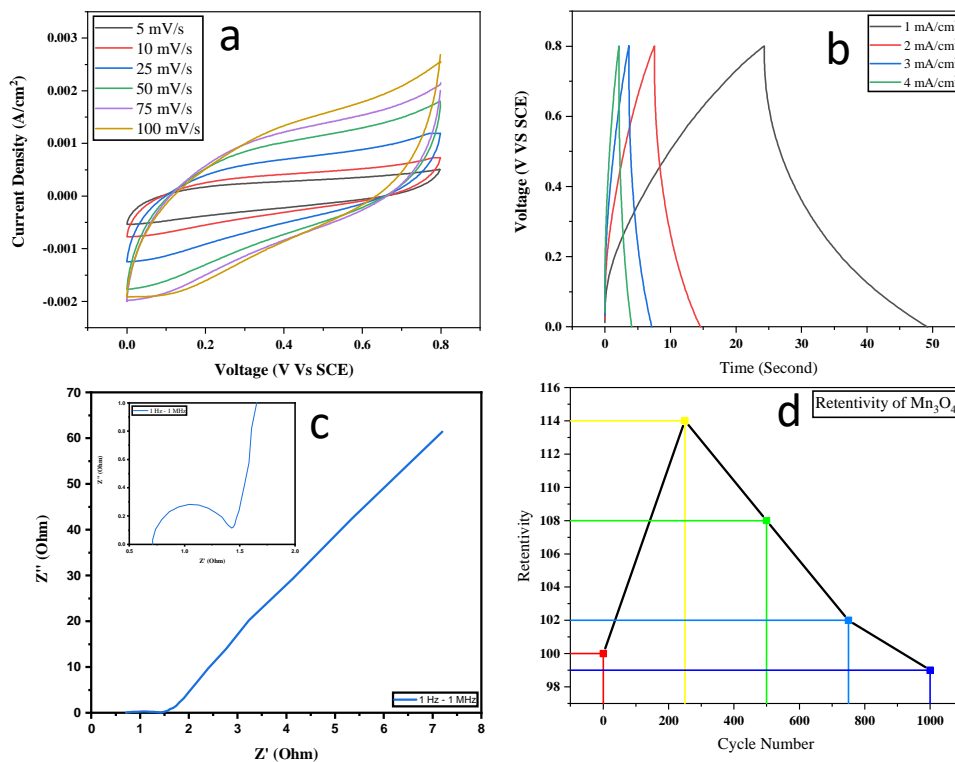


**Figure-5. a) CV curve of  $\text{Mn}_3\text{O}_4$  at various scan rates, b) GCD plot of  $\text{Mn}_3\text{O}_4$  thin film at various current, c) EIS plot of  $\text{Mn}_3\text{O}_4$  and d) Retentivity plot of  $\text{Mn}_3\text{O}_4$  thin film**

## CONCLUSION

In conclusion,  $\text{Mn}_3\text{O}_4$  thin films have been synthesized using a SILAR method. The XRD pattern revealed that the  $\text{Mn}_3\text{O}_4$  thin film is crystalline in nature and a  $\text{Mn}_3\text{O}_4$  phase was confirmed by the FT-IR analysis. SEM images show that the  $\text{Mn}_3\text{O}_4$  thin film surface was completely covered with spherical and polygonal-shaped grains. The contact angle

measurement revealed that the  $\text{Mn}_3\text{O}_4$  surface was hydrophilic, with a contact angle of  $21^\circ$ . In 1M  $\text{Na}_2\text{SO}_4$  electrolyte, the  $\text{Mn}_3\text{O}_4$  thin film achieved a great  $C_s$  of 106 F/g at 5 mV/s and 62 F/g at 1 mA/cm<sup>2</sup>. The developed  $\text{Mn}_3\text{O}_4$  thin film exhibits incredible  $E_d$  and  $P_d$  as of 5.54 Wh/Kg and 800 W/Kg, respectively. The  $\text{Mn}_3\text{O}_4$  thin film achieve a lower value of  $R_s$  and  $R_{ct}$  as 1.44 and 0.98  $\Omega$  and it has a capacity retention rate of 99% after 1000<sup>th</sup> CV cycles at 100 mV/s scan rate. These findings showed that chemically deposited  $\text{Mn}_3\text{O}_4$  thin film is a strong candidate for the role of electrode material in SCs application.

## ACKNOWLEDGMENT

The author Sunny R. Gurav is thankful to the PIFC, Department of Physics, Shivaji University, Kolhapur for providing material characterization facility. Additionally, authors are thankful to the SAIF-CFC-DST centre, Shivaji University, Kolhapur for providing material characterization facility. The financial assistance through DST PURSE-Phase II (2018- 2022) and UGC DSA-Phase II (2018-2023) is highly acknowledged.

## REFERENCES

- 1 Sharma, K. P, Arora, A., Tripathi, S. K., Journal Energy Storage, (2019), 21, 801–825.
- 2 Simotwo, S. K., Delre, C., Kalra, V., ACS Applied Material Interfaces, (2016), 8, 21261–21269.
- 3 Li, Q., Horn, M., Wang, Y., MacLeod, J., Motta, N., Liu, J., Materials (Basel). (2019), 12(5), 703.
- 4 Purkait, T., Singh, G., Kumar, D., Singh, M., Dey, R. S., Scientific Report, (2018), 8, 1–13.
- 5 Waikar, M. R., Shaikh, A. A., Sonkawade, R. G., Polymer Bulletin, (2019), 76, 4703–4718.
- 6 Zhu, J., Wu, Q., Li, J., ChemistrySelect, (2020), 5, 10407–10423.
- 7 Shaikh, A. A., Waikar, M. R., Sonkawade, R. G., Journal of electronic materials, (2019), 48, 8116–8128.
- 8 Li, W., Shao, J., Liu, Q., Liu, X., Zhou, X., Hu, J., Electrochimica Acta, (2015), 157, 108–114.
- 9 Li, Z. Y., Akhtar, M. S., Bui, P. T. Yang, O. B., Chemical Engineering Journal, (2017), 330, 1240–1247.
- 10 Luo, Y., Yang, T., Li, Z., Xiao, B., and Zhang, M., Materials Letters, (2016), 178, 171–174.
- 11 Qiao, Y., Sun, Q., Xi, J., Cui, H., Tang, Y., Wang, X., Journals of Alloys and Compounds, (2016), 660, 416–422.
- 12 Dubal, D. P., Dhawale, D. S., Salunkhe, R. R., Pawar, S. M., Lokhande, C. D., Applied Surface Science, (2010), 256, 4411–4416.
- 13 Munaiah, Y., Raj, B. G., Kumar, T. P., Ragupathy, P., Journal Material Chemistry A, (2013), 1, 4300–4306.
- 14 Sharrouf, M., Awad, R., Marhaba, S., Bakeer, D. E., Nano, (2016), 11, 850–859.
- 15 Wu, Z., Yu, K., Huang, Y., Pan, C., and Xie, Y., Chemistry Central Journal, (2007), 1, 1–9.
- 16 Ahmed, A. M., and Huang, K., Arab. Journal of Chemistry, (2019), 12, 429–439.
- 17 Maile, N. C., Mahadik, S. B., Takale, M. V., Fulari, V. J., materials research express, (2019), 6, 045204.

- 18 Ingole, S. M., Navale, S. T., Navale, Y. H., Dhole, I. A., Mane, R. S., Stadler, F. J., Patil, V. B., *J. Solid State Electrochemistry*, (2017), 21, 1817–1826.
- 19 Kharade, P. M., Kulkarni, S. B., Salunkhe, D. J., *Chinese Journal of Physics*, (2017), 55, 1684–1689.
- 20 Waikar, M. R., Shaikh, A. A., Sonkawade, R. G., *Vacuum*, (2019), 161, 168–175.

# Effect of Artificial Negative Ions on the Nutrition and Growth of Wheat (*Triticum Aestivum*) using Negative Air Ion Generator

Subhash D. Pawar<sup>a</sup>, Pratima S. Sankpal<sup>a</sup>, Satvashila B. Nalawade<sup>b</sup>, Mamata S. Singh<sup>b</sup>,  
Nilesh S. Shinde<sup>b</sup>, P.H. Mangsule<sup>b</sup>, S. B. Jogdand<sup>c</sup>

<sup>a,b</sup>Department of Physics, Arts, Commerce And Science College, Palus 416 310 (MS) India.

<sup>b</sup>Department of Botany, Y. M. College, Pune 111 045 (MS) India.

\*Corresponding author: supath345@gmail.com

---

## ABSTRACT

India is agro-based continental country with 1.35 billion population. The available cultivable land in the country has been continuously encroached and decreased by cement jungles, in the fast expanding cities in India, which has significantly decreased cultivability. Number of scientists concentrated in research on increase in yield and decrease production-cost of wheat all over the world to overcome high demand. Negative air ion generator (NAI) plays very important role in the management of soil and crop yield in the agricultural sector. Main focus of the study is to see the effect of artificially generated negative air ions of the order of 10<sup>9</sup> per cc generated by negative air ion generator (NAI). Treatment of the generated negative ions was observed on nutrition and growth of wheat crop, which may help to increase the yield. The study was carried in the observatory, to observe the effect of artificial negative ions on the nutrition and growth of wheat crop. For this study we cultivated wheat crop (HD-2496) in the pots separately for untreated crop as a control and treated crop to find the result. In this research it has been observed that growth of plants and percentage of mineral nutrients present in wheat crop has been increased. Thus, after treatment of negative air ions, we found that the values of rate of growth and eight mineral nutrients like N, P, K, Na, Fe, Zn, Mn, and Cu of the wheat crop has been increased. Due to this experiment, there is no need of using other fertilizers. It has given hopeful results to increase the yield and quality of wheat grains. Such study significantly alters the electrostatic configuration of the agriculture and increases cation holding capacity (CEC) of the soil to maintain fertility, giving healthy vigorous crop.

## KEYWORDS

Negative air ion generator (NAI), Negative air ions, Wheat plant (*Triticum aestivum*), Cation exchange capacity (CEC), Nutrition, Mineral Nutrients.

.....

## 1. INTRODUCTION

Wheat is the one of the oldest and second-largest seasonal cereal cultivated in rubi crop in India. The overall area under the crop is about 29 million hectare within the country. The productivity of wheat which was 2602 kg/hectare in 2004-05 has increased to 3140 kg/hectare in 2011-12 [25]. Wheat is known as world's most important nutrient crop which can provide approximately 20% of calories. Therefore, world's nutrient is build upon wheat and wheat products; e.g. pasta, chapatti, breads, etc. [16]. To improve crop yield many of

farmers in India widely used chemical fertilizers and pesticides in agriculture. Though chemical fertilizers increase crop production; their overuse has hardened the soil, decreased fertility, strengthened pesticides, polluted air and water, released greenhouse gases, thereby bringing hazards to human health and environment as well. Therefore, our study is to overcome the use of fertilizers and pesticides. So, we developed alternative option which is known as negative ion generator (NAI). All airborne particles in the environment with electrical conductivity and charges (positive and Negative) are known as air ions [24]. Main work of NAI is to generate a negative ion which carries negative charge (Figure-2).

There are many harmful effects of air pollutions on plants; they can have direct poisonous impacts or by implication by changing soil pH followed by solubilisation of the sulphur dioxide can influence the opening of the stomata, bringing about excessive loss of water. Air is mixture of different gases. Natural air ions are generally producing many ways such as gamma rays, natural radioactivity, cosmic rays, waterfalls and wind motions. Ionisation, attachment, and clustering are three phases for stable form of ions [23]. When atom loses or gains electron then it is said to be positively or negatively charged respectively. Process is called as ionisation [22] as shown in Figure-3. For atom or molecule which is electrically neutral and balanced, it is said to have an equal number protons and electrons [22]. Losing an electron atom molecule becomes negative ions [24]. The constriction of such negative air ions in the atmosphere affects human health and plant physiology.

The participation of air ions in the atmosphere has increased the interest of scientists in the aerosol formation, its influence of air quality, climate change and human health. Studies of various scientists have been revealing and describing the impact of air ions on human and crop health. Oxygen and other ionised molecules of air components have stronger effect on human being [22]. Air ions may have healing or harmful effect on human health. We feel happy, relaxed and breathe easy in the presence negative ions [20].

In the recent year air ionizer is used for as air management and soil management which killed bacteria present in atmosphere which is healthy for human health. Number of researchers has been invented the biological action of ions in atmosphere but attention has given on physical action of air ions. Clinically study shows that negative air ions overcome the bacterial activity present in atmosphere and protected the human life [29]. Negative ions which help to kill bacteria or viruses present in plant and soil and increase growth of plant and nutrient level [29].

The aim of this study is to see the effect of artificially generated negative air ions on the nutrition and growth of wheat crop (*Triticum aestivum*), without using fertilizers and pesticides useful for human health. It may be useful to improve the economy by increasing the yield of wheat in developing country like India. Our hypothesis explained the physical evidences of effect of generated air ions in agricultural sector. There has been great interest to see the effect of negative air ions artificially generate negative air ion generator on the nutrition, growth and increase in the yield of different crops.

## **2. EXPERIMENTAL DETAILS**

### **2.1 Experimental details and study area**

Our experiment carried out at Ghogaon (17°05'29"N, 74°26'27"E) and 570 m above sea level) rural area located in Sangli District; Maharashtra (India) as shown in **Figure-1a**. Figure

1d shows the vegetation area around the observatory at rural site Ghogaon, climate is clean, less dust particles and high wind speed (~2.6 mt/sec towards East).

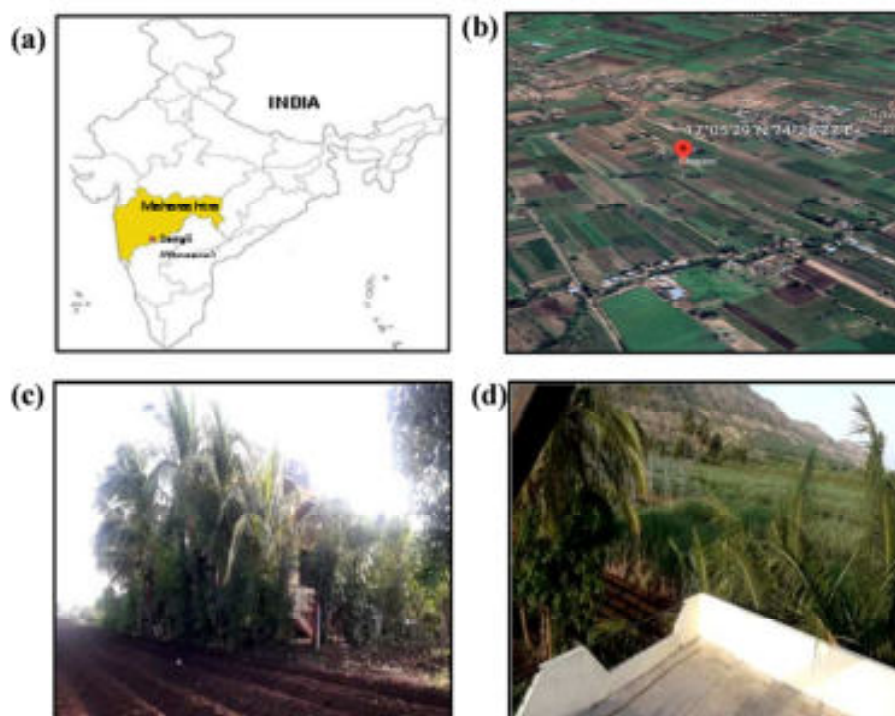


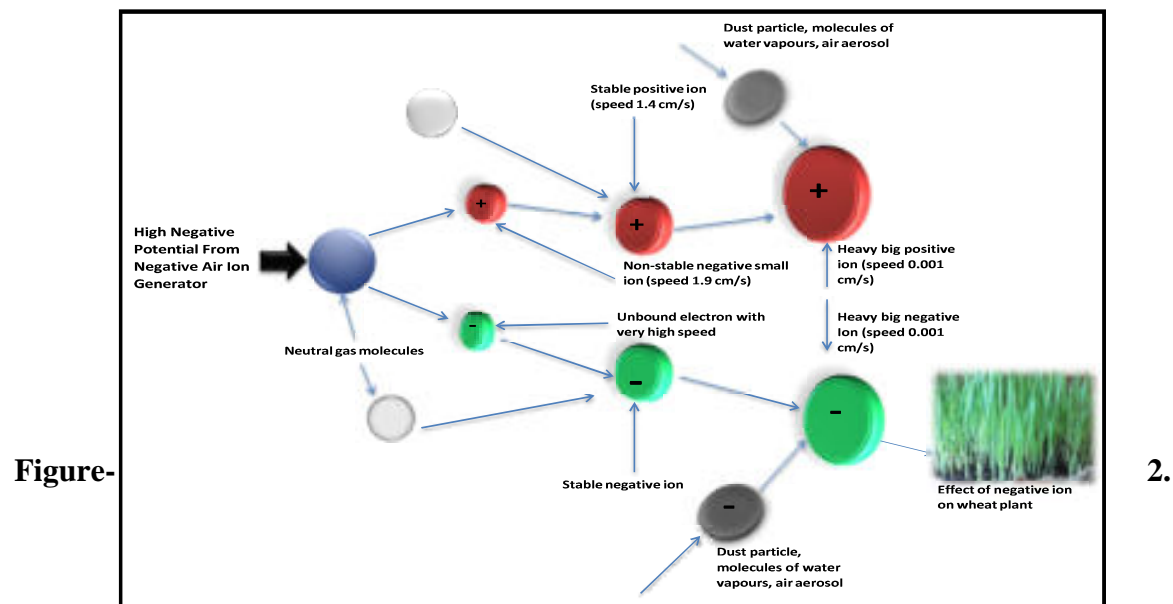
**Figure-1. a) Map of Ghogaon (17°05'29''N, 74°26'27''E) rural area located in District Sangli; Maharashtra (India), b) Satellite view of rural area Ghogaon (Sangli), c) The vegetated area surrounding the observatory at rural site Ghogaon, d) Mountain site surrounding to the observatory.**

The experiment was conducted in the well-furnished observatory on the first floor. The room temperature was 25 °C ( $\pm 1$  °C) in all of the measuring tests **Figure-1c**. The NAI was placed at the distance of one feet from the wheat plant. The mountain site just half Km from observatory **Figure-1d**. Google map clearly shows observatory surrounding area is covered with vegetation area with few numbers of homes; it is typical Indian village **Figure-1b**.

Two pots of same size and shape filled with same type of soil from the same locality containing 100 seeds each of wheat HD-2496 variety, and covered with a soil properly with a same quantity placed at N.T.P.in two separate rooms. First dish placed without negative ion generator in room and another dish is placed with negative ion generator another room. The treatment of negative air ion was given from 12 November 2020 to 27 November 2020 continuously for sixteen days and height of plants was recorded on 11, 12, 20 and 23 November in first experiment. Daily same water content was poured to both the dishes at the same time and growth was recorded. All plants were removed from each dish separately and dried properly in clean area in the shade. The plants from two pots and soil were separately sent for laboratory testing. The testing report was recorded. Same experiment was repeated for the period from 13 January 2021 to 28 January 2021.

## 2.2 High negative potential (-eV)

According to variation of energy in the environment, different methods based on natural generation are introduced. As for artificial generation of NAI, corona discharge is dominantly elaborated due to its preponderance in convenient to control of the concentration of ions. It tends to introduce the determination of NAI, containing quantitative and qualitative detection, by using ion counting device. By using negative air ion generator near about 7000V negative potential is created at the tip of negative air ion generator as shown in **Figure-2**. When neutral air molecules come in to contact with high negative potential electron is attached to the neutral molecule. Thus, neutral atoms and molecules are negative charged. These negatively charged air ions repelled by high negative potential of negative air ion generator. These artificially produced negative are surrounded by wheat plant in the observatory.



**Schematic of production of negative air ions by negative air ion generator.**

## 2.3 Process of cation exchange capacity (CES)

Cation exchange is the absorbed cations replenished the ion in the soil solution when concentration decreases due to uptake by plant root. Cation exchange capacity (CEC) is a measure of the total negative charges within the soil that absorbs plant nutrients cations such as calcium ( $\text{Ca}^{2+}$ ), magnesium ( $\text{Mg}^{2+}$ ), and potassium ( $\text{K}^+$ ) (**Figure-3**).

Cations are positively charged; they are held by negatively charged sites on clay and humus particles called colloids. These consist of thin, flat plates and for their size, have a comparatively large surface area.

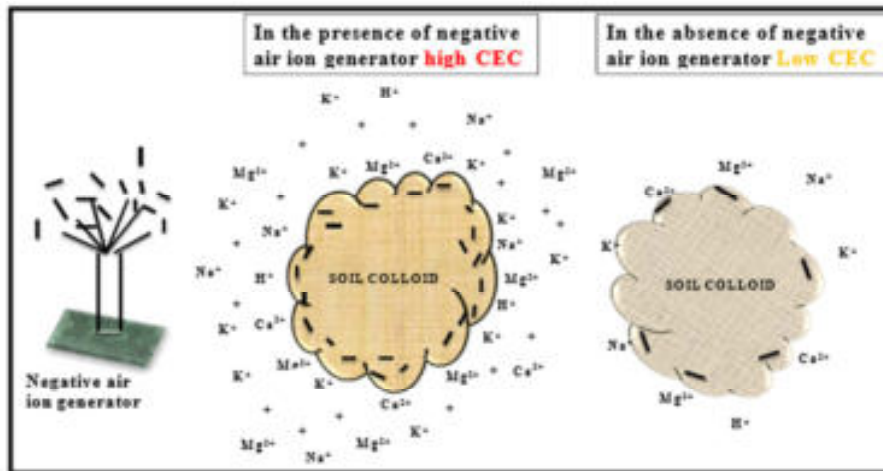
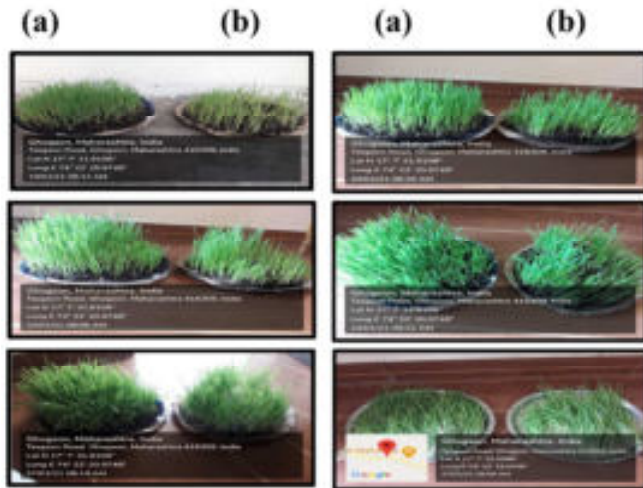


**Figure-3. Schematic representation of cation exchange capacity (CEC) process in presence and absence of NAI.**

Therefore because of this reason they are able of griping very high quantities of cations. The stronger the negative charge on the colloid, the higher its capacity to grip and exchange cations, hence the term CEC (**Figure-3**).

### 3. RESULTS AND DISCUSSION

The result indicates that high concentration of negative ions causes significant change the experimental data (**Table-1 and 2**). It shows the effect of treatment of negative ions on the wheat crop. To support this observation control without treatment has been shown. It has been observed that wheat crop under treatment of negative ions generated by NAI, show comparatively more healthy growth and stability than untreated wheat crop **Figure-4 and 5**. Daily measurements revealed variability in height of wheat plants, which showed comparatively more height in treated plants than untreated plants (**Figure-5a&b**). After the treatment of negative air ions Nitrogen increases from 1.76% to 1.80%, Phosphorus from 0.22% to 0.27%, Potassium from 0.12% to 0.13%, Sodium from 69.00% to 73.00%, Iron changes from 102.04 PPM to 138.40 PPM, Zinc 30.16 PPM to 34.80 PPM, Manganese from 52.25 PPM to 61.42PPM, Copper 48.20 PPM to 55.20 PPM (**Table-2**) in the first experiment. From the graph it is also clear that nutrition of wheat increases due to negatively charged generated air ion near the plants (**Figure-6**). In the second experiment conducted from 13 to 28 January 2021 with same soil and environment, we observed clearly increase in mineral nutrients of the wheat plants after the treatment of negative ions by NAI in the soil and on the crop (**Table-2**). It revealed after the treatment of negative air ions Nitrogen increases from 4.60% to 4.72%, Phosphorus from 0.83% to 0.84%, Potassium from 1.19% to 2.11%, Iron changes from 156.24 PPM to 182.25 PPM, Zinc 32.75 PPM to 37.40 PPM, Manganese from 0.21 PPM to 0.22 PPM, Copper 6.77 PPM to 8.33 PPM (**Table-2**) in the second experiment.



Analysis Report			
Sr. No.	Constituents	Without treatment	With treatment
1.	Nitrogen%	1.76	1.80
2.	Phosphorous%	0.22	0.27
3.	Potassium%	0.12	0.13
4.	Sodium%	69.0	73.0
5.	Iron in PPM	102.04	138.40
6.	Zinc in PPM	30.16	34.80
7.	Manganese in PPM	52.25	61.42
8.	Copper in PPM	48.20	55.20

**Figure-4. Daily observation of growth of Wheat crop a) with Table 1: Nutrition analysis report without and b) without treatment of negative air ion generator at with treatment of NAI Ghogaon from 12 to 27 November 2020.**



Analysis Report			
Sr. No.	Constituents	Without treatment	With treatment
1.	Nitrogen%	4.60	4.72
2.	Phosphorous%	0.84	0.85
3.	Potassium%	1.99	2.11
4.	Sodium%	62.00	65.8
5.	Iron in PPM	156.24	182.25
6.	Zinc in PPM	32.75	37.40
7.	Manganese in PPM	0.21	0.22
8.	Copper in PPM	6.77	8.32

**Figure-5. Repeated experiment from 13 to 28 January Table 2: Nutrition analysis report with and 2021 for daily observation of growth of Wheat without treatment. Crop a) with b) without treatment of NAI at Ghogaon.**

### 3.1 Graphical interpretation of nutrient level

The variation in nutrition of wheat plants before and after the treatment by the negative ions using NAI of both the experiment have been presented in **Figure- 6a** and **6b**. It has clearly

revealed that treated plants showed steady increase in the nutrient level in the both the experiments as compared to untreated plants.

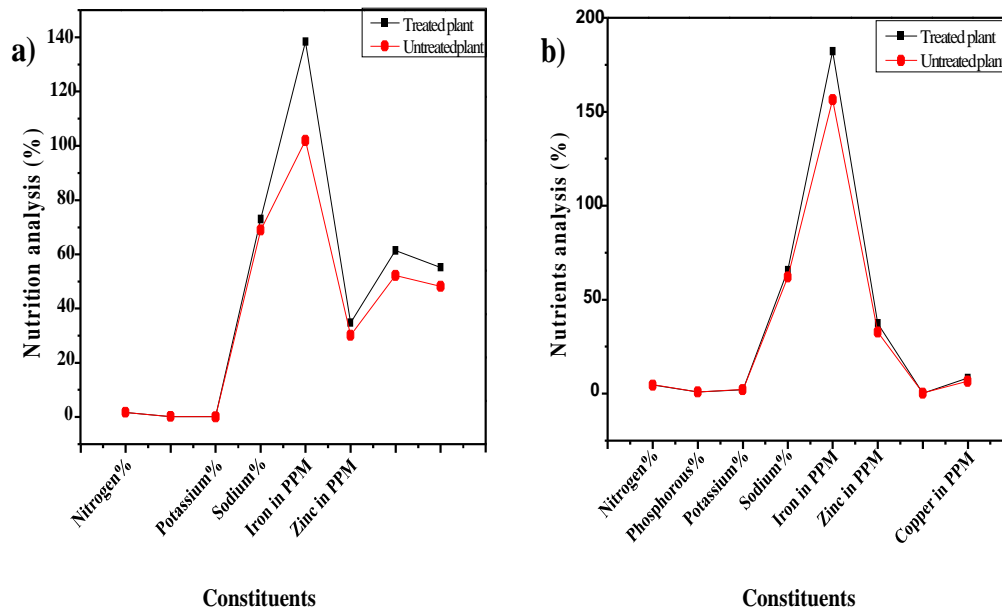


**Figure-6. a) Nutrition variation of wheat plant with different constituents present in plant, before and after treatment of NAI (From 12 to 27 November 2020) b) After repeated same experiment of nutrition variation of wheat plant with different constituents present in plant (from 13 to 28 January 2021).**

Increased Fe level from 102.4 & 156.24 to 138.40 & 182.25 respectively in both the experiments. It helps for more chlorophyll pigments in the leaves giving bright green colour to the leaves enhancing rate of photosynthesis consequently resulting in the higher growth rate to help higher productivity of quality wheat grain.

Zinc plays important role in yield of plant and it is also known as foliar application. Mn, N, P, K, Na and Cu are also important micronutrients for more wheat plant growth and NPK acts as natural fertilizer to the wheat crop. Thus, it avoids use of chemical fertilizers and soil and air pollution. From these observations, we may conclude that effect of negative ions using NAI on wheat plants gave positive response of nutrients on the growth of wheat plants.

### 3.2 Graphical interpretation of growth of wheat crop

There is no need of chemical fertilizers and avoids soil and air pollution. The histogram shown in the **Figure-7** clearly revealed comparatively more growth on 11<sup>th</sup>, 12<sup>th</sup>, 20<sup>th</sup>, and 23<sup>rd</sup> November 2020 in the first experiment and on 19<sup>th</sup>, 21<sup>st</sup>, 22<sup>nd</sup>, and 23<sup>rd</sup> January 2021. It clearly indicates good results and vigorous growth of wheat crop. These results of the experiments showed vigorous growth of wheat crop as alternative method of soil and crop treatment as a substitute method in the place of chemical manual treatment preventing the soil and air pollution.

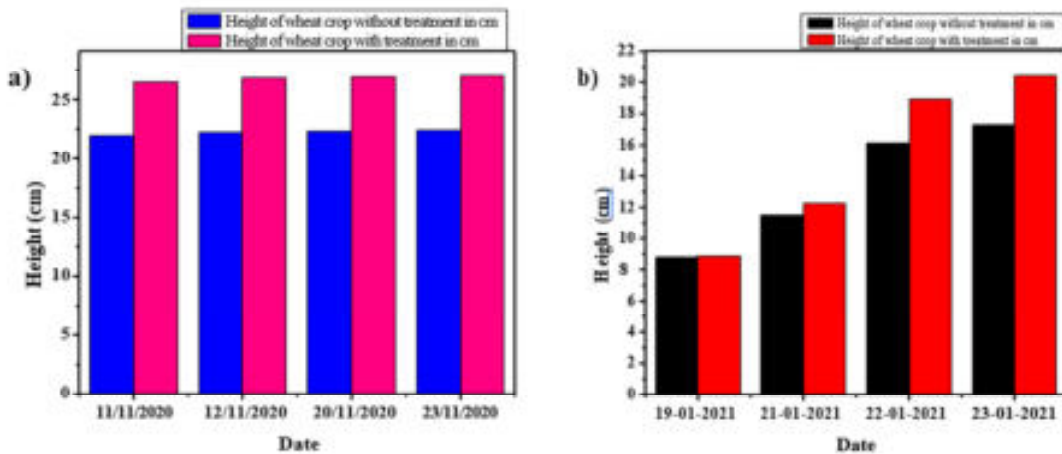


**Figure-7. Growth of Wheat crop at rural at Ghogon a) From 12 to 27 November 2020 b) From 13 to 28 January 2021.**



**Figure-8. Growth of wheat a) Without b) With treatment of NAI at rural station Ghogon.**

In a research study of equilibrium separation of heavy metals in Dutch field soils, it was observed that the solid/aqueous phase partition coefficients for Cd, Cu, Ni, Pb and Zn correlated well with CEC [30]. In a study on Pb bioavailability and toxicity to earthworm's significant negative relationships between mortality and pH and between mortality and CEC were demonstrated [10]. In the same study statistically, remarkable negative associates emerged between internal Pb, CEC. Furthermore, the relationship between earthworm internal Pb concentration and soil properties such as CEC was also significant [10].

Ion exchange phenomena in soil are important for retaining and increasing the nutrients status of soil [13]. Various types of clay minerals along with the organic matter in the soil have certain electrically charged site which can attract the opposite charge ions in soil. With negative charge site in the layer lattice clay minerals, CEC of the soil increases which have the ability to hold positive cations like H<sup>+</sup>, Al<sup>3+</sup>, Ca<sup>2+</sup>, Mg<sup>2+</sup>, Na<sup>+</sup>, NH<sub>4</sub><sup>+</sup>, etc. So, with increase ion exchange in soil, it has the capacity to hold the nutrients in the form of ions but exchangeable with other similar charged ions from the soil solution [1]. By holding the nutrients in the surface layer, it reduces the loss of nutrients through leaching and in other way it reduces the contamination of groundwater with the ions or heavy metal reducing water

pollution [28]. CEC in soil is an important index for the fertility status of soil [2]. With increase in CEC the exchangeable nutrient ions in soil increases and this exchangeable form of nutrients is the most available form for plant uptake. Plant roots also have the ability to exchange cations from the soil. This property of root is due to the presence of free carboxylic groups of Uronic acid of pectin (Laird et al., 2010). There lies a positive correlation with the dry matter production and yield of crops with the increase in CEC of soil [17]. Nutrients uptake by plant to shoot and grains from soil is influenced by the roots CEC [31], which also depends on different physiological growth stage of plant [4]. With large CEC the nutrient gripping capacity of a soil increases with its capability to grip nutrients cations in the negative charged surface making many nutrient buffering capacities of the soil for plant uptake **Figure- 8.**

#### **4. ROLE OF PHOSPHORUS**

Phosphorus is a component of high-energy bonds, including phosphoanhydride, acyl phosphate and enol phosphate and plays an important role in cellular metabolism. These high-energy phosphate-containing compounds transfer the energy to acceptor molecules, thereby serving as sources of crucial cellular processes. It plays an important role in photosynthesis right from the seedling growth till grain formation and maturity [8]. Uptake is the first step of the pathway involved in the movement of any element from soil to roots and other plant parts. The availability of phosphorus in soil solution is largely decided by soil components, including soil pH, texture and concentration of phosphorus. In NAI treatment phosphorus increases from 0.22% to 0.27% in first and 0.83% to 0.84% in second experiment this is due CEC in increases after the treatment of negative ions by NAI.

Air pollution has become a serious environmental stress to crop plants due to increasing industrialization and urbanization during last decades [26]. Some scientists have reported the adverse effect of air pollution on wheat crops [27]. Air pollution emitted from urban and industries adversely affecting the ambient air and agricultural production. It is very clear that urban and industrial air pollution has become a serious threat to agricultural production. In this study artificially generated negative ions not only used to increase the CEC of soil but also used for cleaning air pollution surrounding the wheat crop. Negative air ions produced by NAI are combined with pollutants surrounding the wheat crop and settle down on surface [22]. Due to these reasons even though we are not used fertilizers or pesticides there is growth both in height and mineral nutrients in the NAI treated wheat plants.

#### **5. CONCLUSION**

From this study we have to conclude that, negative ions which help to kill bacteria or viruses present in plant and soil and increase growth of plant and nutrient level. In this study observed that negative air ion produced around wheat plant by negative air ion generator. Due to high negative potential 1010 negative air ions per  $\text{cm}^3$  are generated. Soil in plant pot is more negatively charged. At the same time more cations are held by soil due to more negatively charged soil. As there is attraction between positively charged cation near the surface of soil and negatively charged soil as result cation exchange capacity (CEC) increased. Therefore, more nutrients were provided to wheat plant. Automatically, nutrients of plant in increases, due to that yield of wheat will increase without using any fertilizer or

pesticides. This naturally produced wheat production is healthy for human health and production cost effective for developing country like India. Negative air ions produced by NAI are combined with pollutants surrounding the wheat crop and settle down on surface. Due to these reasons even though we are not used fertilizers or pesticides there is growth both in height and mineral nutrients in the NAI treated wheat plants.

In Further study we will see the effect of treatment of negative ions using NAI on wheat crop in green house which will be helpful to the increase the yield of wheat grains.

In present work, the ZCN NCs were prepared using simple sonochemical method. Further bare ZnO NRs and ZCN NCs based working electrodes were fabricated via binder free technique. The structural, optical as well as morphological studies were performed using XRD, FTIR, UV-Visible DRS and SEM analysis. The highest PEC performance was observed for ZCN1 NCs based working electrode, which also possessing high chronoamperometric stability. Hence, such ZCN NCs based photoanodes will be highly appreciated and efficient for solar energy conversion studies.

## ACKNOWLEDGMENT

This work was supported by Government of India, Ministry of Science and Technology, Department of Biotechnology, New Delhi. Authors gratefully acknowledge to Department of Biotechnology, New Delhi under star college Scheme for financial assistance to complete the project and thankful to the great support to the Principal of A.C.S college, Palus. Authors would like to acknowledge for technical supports from Arts, Commerce and Science College, Palus (Maharashtra), India.

## REFERENCES

- 1 Asadzadeh, F., Maleki-Kakelar, M. Shabani F. (2019), Northwest Iran. *Commun. SoilSciPlan.*50 (9):1106-1116.
- 2 Dvorak, J., Koryta, J. (1983). *Electrochemistry*. Prague: Academia. [In Czech]. Fischer, O., Kisova, L. Miadokova, M. Molin, J. (1983). *Physical Chemistry*. Prague: SPN. [In Czech].
- 3 Fredriksson, H., Salomonsson, L. Salomonsson, A. (2008). *Acta Agriculture Scandinavia, Section B- Soil and Plant Science*, 47, 35.
- 4 Goswami, R. Bajpai R. Tiwari, A. Bachkaiya, V. (2017), *Journal of Pharmacogn Phytochem*, 6(6):146-151.
- 5 Guo, J., Jia, Y. Chen, H. Zhang, L. Yang, J. Zhang, J. Zhou, Y. (2019), *Science Reporter*; 9(1): 1-12.
- 6 Guo, Y., Zeng H., Zheng, R., Li S., Pereira, G., Liu, Q. (2017), *Total Environment Science.*, 579:1460–6.
- 7 Gupta, A., (2016), Kulshrestha U., Saxena, P. (eds) *Plant Responses to Air Pollution*. Springer, Singapore. Malhotra, H., Sharma, V.,S., and Pandey, R., (2018), *Plant Nutrients and Abiotic Stress Tolerance*, Springer Nature Singapore pp171-190.
8. Hashim, D., Boffetta, P., (2014), *Ann Glob Health.*, 80:393–411.
- 9 Hou, Q., An X.,Q., Wang, Y., Guo, J.P., (2009), *Science of Total Environment*, (2010) 408:4026–32.
- 10 Jiang, S., Ma, A., Ramachandran, S., (2018), *International Journal of molecular*

- science.19, 2966.
- 11 Laird, D., Fleming, P., Wang, B., Horton, R., Karlen, D., (2010), *Geoderma*, 158(3): 436-442.
  - 12 Manisalidis, I., Stavropoulou, E., Stavropoulos, A., Bezirtzoglou, E., (2020), *Front. Public Health*, 8:14.
  - 13 Manucci, P., Franchini, M., (2017), *International Journal of Environment Research Public Health*, 14:1048.
  - 14 Matthew, P., (2016), *Essays in biochemistry* 60, 3, 255-273.
  - 15 Mallick, S., A., Gupta, K., A., Sharma, V., Sinha, B., K., *Ind J Plant Physiol.*, 18(2):183–186.
  - 16 Meychik, N., Nikolaeva, Y., Kushunina, M., Yermakov, I., (2014), *Plant soil*, 381(1-2):25-34.
  - 17 Mitchell, J., and Soga, K., (2005), John Wiley and Sons, New York.
  - 18 Middleton, R., (1989), *A Negative-Ion Cookbook.*, Dept. of Physics, Univ. of Pennsylvania.
  - 19 Moore, M. and Reynolds, R., (1997), *X-ray diffraction and the identification and analysis of clay minerals*”, Oxford University Press, New York.
  - 20 Patil, G., Pawar, S., Gurav, O., Bhosale, J. and Rananavare, S., (2021), *Int. J. Environment and Sustainable Development*, Vol. 20, No.2, pp.201–211.
  - 21 Pawar, S., Meena, G., Jadhav, D., (2010), India, *International Journal of Aerosol and Air Quality Research*10: pp 154-166..
  - 22 Pawar, S., Meena, G., Jadhav, D., (2011), India. *Journal of Global NEST*, 13. No.1. 65-73.
  - 23 Pawar, S., Meena, G., Jadhav, D., (2010), *Aeosol and Air Quality Research*, 12: 440-415.
  - 24 Pawar, S., (2013), India. *Journal of Earth System Science*, 122, No. 1, 229–237.
  - 25 Pradhan, S., Sehgal, K., K., Bandyopadhyay, P., Panigrahi, C., M., Parihar, C., M., Jat, S., L., (2018), *Ind J Plant Physiol.*, 23(3):416–425.
  - 25 Rajput, M., Agrawal, M., (2004), *Indian Journal of Plant Physiology* 9(1): 9-14.
  - 26 Rajput, M., Agrawal, M., (2005), *Environmental Monitoring and Assessment* 101: 39-53.
  - 27 Rahal, N., Alhumairi, B., (2019), *International Journal of Environment Science*; 16(7):3183-3192.
  - 28 Shepherd, S., Beggs, C., Smith, C., K., Noakes, C., Sleigh, P., (2010), *BMC Infect Dis.*12; 10:92.
  - 29 Syers, J., Campbell, A., Walker, T., (1970), *Plant and Soil*, Vol.33, pp.104-112. Ullah, A., Ma, Y., Li, J., Tahir, N., Hussain, B., (2020), *Agronomy*. 2020; 10(3):359.
  - 30 Watson, J., Robinson, N., Chow, J., Henry, R., Kim, B., Pace, T., Meyer, E., and Nguyen, Q., (1990). *Environment Software* 5:38-49.

# Synthesis and Characterization of Copper Oxide Nanoparticles via Chemical Route for Antibacterial Activity

Shweta M. Pawar<sup>a</sup>, Vithoba L. Patil<sup>a,b</sup>, Sumit D. Korade<sup>a</sup>, Sarika B. Dhavale<sup>a</sup>,  
Satyajeet S. Patil<sup>a</sup>, Pramod S. Patil<sup>a\*</sup>

<sup>a</sup>Department of Physics, Shivaji University, Kolhapur 416004 (MS) India.

<sup>b</sup>School of Nanoscience and Biotechnology, Shivaji University, Kolhapur 416004 (MS) India.

\*Corresponding author: psp\_phy@unishivaji.ac.in

---

---

## ABSTRACT

*Copper oxide nanoparticles were synthesized by a one-step hydrothermal method using copper acetate as a precursor. The purity, Monoclinic structure, and crystallinity of copper oxide nanoparticles were confirmed by x-ray diffraction, revealing a crystalline size of 16.87 nm. The Uv-visible spectra showed maximum absorbance at wavelength 310 nm and the band gap of copper oxide nanoparticles found to be 4.1 eV. Functional groups present in the sample were confirmed by Fourier Transform Infrared Spectroscopy. Scanning electron microscopy revealed a nanoflake-like morphology of the prepared copper oxide nanoparticles. The zone of inhibition for Bacillus subtilis (gram-positive bacteria) was found to be 8 mm and the zone of inhibition for Escherichia coli (gram-negative bacteria) was found to be 7 mm as compared to the standard antibiotic cefotaxime.*

## KEYWORDS

*Antimicrobial, Copper Oxide, Hydrothermal, Monoclinic, Transition Metal Oxide.*

.....

## 1. INTRODUCTION

Due to desirable qualities of copper oxide (CuO) nanoparticles such as low cost, nontoxicity, and ease of use, copper oxide nanoparticles have significant interest in research fields like Solar cells, Biodiesel, Photocatalysis, Supercapacitors, Electrocatalysis, Antimicrobial activity, etc. [1]. Scientists are currently working on copper oxide nanoparticles by various methods such as hydrothermal method, Solvothermal method, reflux method, sol-gel method for different applications [2]. Antibacterial activity is a very important characteristic in medical science, to provide enough protection against harmful bacteria and disease transmission. Transition metal oxide nanoparticles have great attention in recent years and applications in numerous fields. As compared to micro or bulk-sized materials, nanoparticles have a high surface-to-volume ratio which produces unrivaled physical and chemical properties [3]. To prevent microbial contamination of fabric nanoparticles including

silver, Chitosan, silicon dioxide, titanium dioxide, and zinc oxide have become popular in the textile industry [4]. An innovative and simple method for creating CuO nanocrystals is hydrothermal synthesis.

Copper oxide is a p-type semiconductor exhibiting a monoclinic phase and band gap of 1.2 eV. CuO has been extensively used as a gas sensor, heterogeneous catalyst, and field emission emitter in a variety of fields [5]. Due to their effectiveness in heat transfer applications as nanofluids, CuO NPs are of particular interest [6]. The United States Environmental Protection Agency (USEPA) has permitted copper and its alloy to kill 99.99% of bacteria [7]. Pathogenic bacteria becoming a pitfall to human health [8]. Copper oxide (CuO), zinc oxide (ZnO), titanium oxide (TiO<sub>2</sub>), and iron oxide (Fe<sub>2</sub>O<sub>3</sub>) played an important role in antimicrobial activity. Copper oxide is more inexpensive than silver and has stable physical and chemical properties [9]. The novelty of the work lies in the synthesis of copper oxide nanoparticles using the hydrothermal method and the observation of nanoflake morphology. The use of hydrothermal synthesis is a relatively simple and cost-effective method for the production of nanoparticles, and the resulting nanoflakes may have unique properties compared to other morphologies, such as spheres or rods. Additionally, the testing of the synthesized nanoparticles for antimicrobial activity against *Bacillus subtilis* and *Escherichia coli* is also a novel aspect of the work, as it demonstrates the potential applications of these materials in the field of microbiology.

The problem statement of work could be summarized as the need for more effective and sustainable methods for controlling bacterial growth, particularly in healthcare and food production settings. The widespread use of antibiotics has led to the emergence of antibiotic-resistant strains of bacteria, making it increasingly difficult to control bacterial infections. In addition, there is a growing concern about the environmental impact of traditional antimicrobial agents, such as heavy metals. The development of novel, environmentally friendly antimicrobial agents is therefore an important area of research. A focus of this study is to synthesize copper oxide nanoparticles by hydrothermal method and to study antibacterial activity of CuO NPs against *Bacillus subtilis* and *Escherichia coli*.

## **2. EXPERIMENTAL SECTION**

### **2.1 Synthesis of copper oxide NPs**

Copper oxide nanoparticles were prepared via hydrothermal method using copper acetate monohydrate (C<sub>4</sub>H<sub>8</sub>CuO<sub>5</sub>) as a precursor and sodium hydroxide (NaOH) as a precipitate agent. In a typical synthesis procedure 0.1 M C<sub>4</sub>H<sub>8</sub>CuO<sub>5</sub> (SD Fine Chem Ltd.) is added to 100 ml of double distilled water after that 1 M Sodium hydroxide (NaOH) solution was added drop wise to copper acetate solution under continuous stirring so as to get pH value 10. Then solution transferred into Teflon lined steel

autoclave at temperature 120°C for 2 hours under autogenous pressure. The solution filtered with filter paper and washed several times with double distilled water and ethanol to remove impurities. The filtrate was dried over night at 60°C in oven. The obtained powder further annealed at 400°C for 2 hrs. Figure-1 shows the schematic of synthesis of CuO NPs.

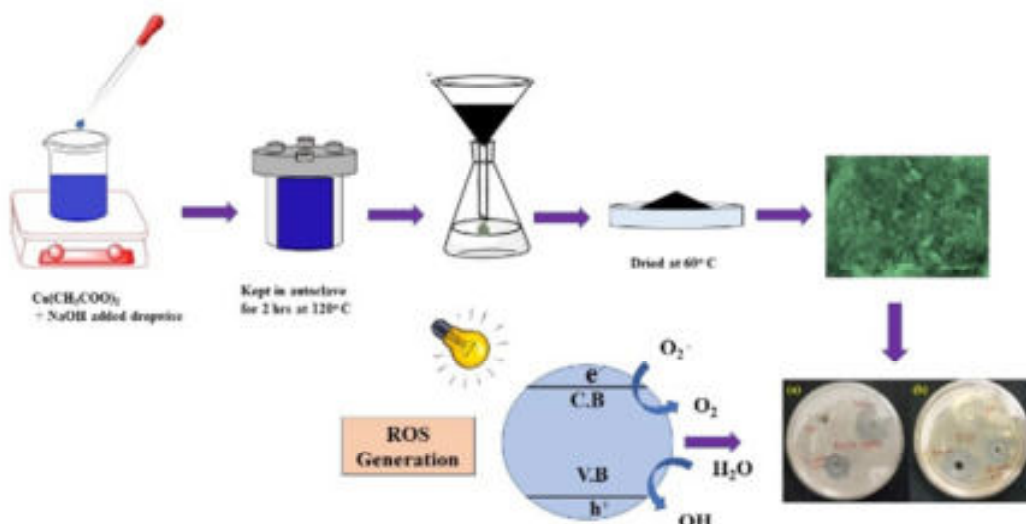


**Figure-1. Schematic of synthesis of CuO NPs**

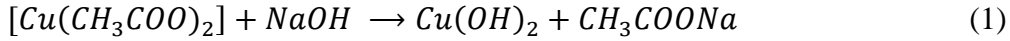
## 2.2 CHARACTERIZATION TECHNIQUES

Powder X ray diffraction pattern to confirm monoclinic phase of copper oxide nanoparticles were recorded on X-ray diffractometer using Cu-K $\alpha$  radiations of wavelength 1.54 Å in the 2 $\theta$  range of 10° to 90°. (Bruker AXS Analytical Instruments Private Ltd., Germany, Model: D6 phaser). Uv-visible spectroscopy was used to know absorption in sample. The Uv-Vis spectra recorded in the range of 200-800 nm. FTIR spectra of the samples were recorded using FTIR spectrometer (JASCO, Lisses, France) with the pellet technique in the wavenumber range of 4,000-400 cm<sup>-1</sup>. The surface morphology of copper oxide nanoparticles was characterized by using scanning electron microscopy [JEOL JSM 6360] with accelerating voltage 18 KeV. Antibacterial activity of CuO NPs was analyzed using disk diffusion assay.

## 3. RESULTS AND DISCUSSION

### 3.1 Growth mechanism of CuO NPs

Copper acetate monohydrate is used as copper precursor and sodium hydroxide as precipitating and stabilizing agent [5]. Sodium hydroxide reacted with copper acetate monohydrate to form copper hydroxide and sodium acetate.



On heating at 400 °C, copper hydroxide decomposes into copper oxide.



### 3.2 X-ray diffraction study

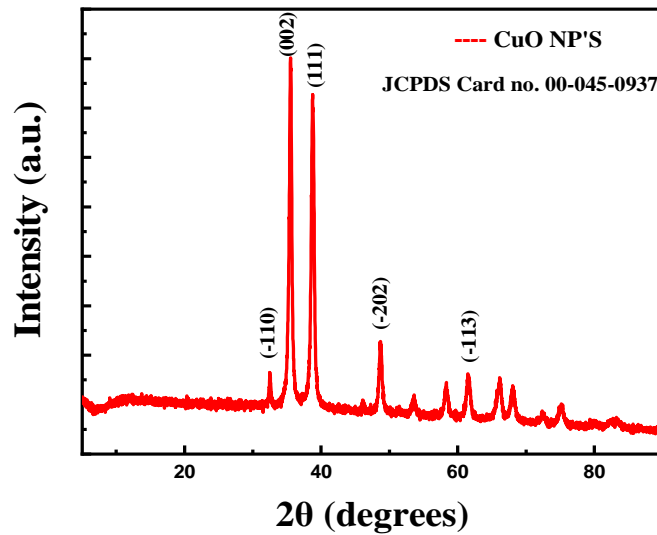


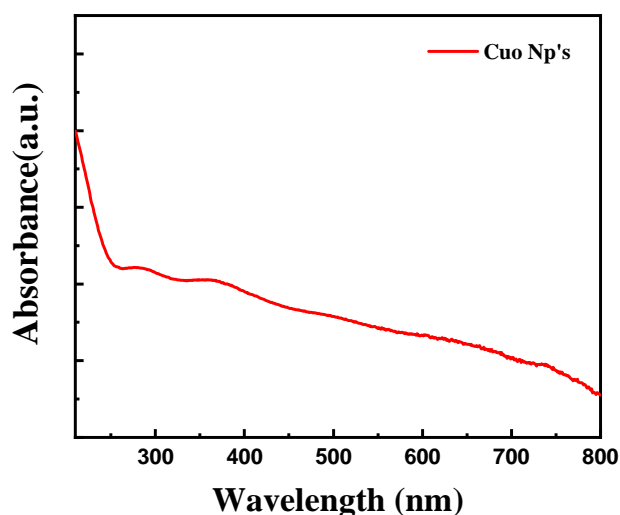
**Figure-2. X-ray diffraction of CuO NPs**

The phase and structural characteristics of copper oxide nanoparticles were confirmed using X- ray diffraction technique [10,11,12]. Copper oxide nanoparticles forms monoclinic structure. The diffraction peaks of copper oxide nanoparticles centered at 32.59°, 35.60°, 38.79°, 48.70°, 58.29°, 61.54°, 66.19°, 68.20° corresponding to the crystal planes (-110), (002), (111), (-202), (202), (-113), (-311), (-220) and matched with *JCPDS Card no. 00-045-0937*[11-14].(002) is most intense peak hence it attributed to high crystallinity and purity of sample. The crystallite size was calculated from Scherrer formula [13].

$$D = \frac{0.9\lambda}{\beta \cos\theta} \quad (3)$$

Where  $\lambda$  is wavelength of X- ray (1.54 Å).  $\beta$  is full width half maxima. The crystallite size found to be 16.87 nm. According to literature, (002) peak is most intense peak. It is seen that monoclinic phase was observed in many reports. It is

clearly seen that x-ray diffraction results in our work are well concurred with literature.



### 3.3 UV-Visible spectroscopy

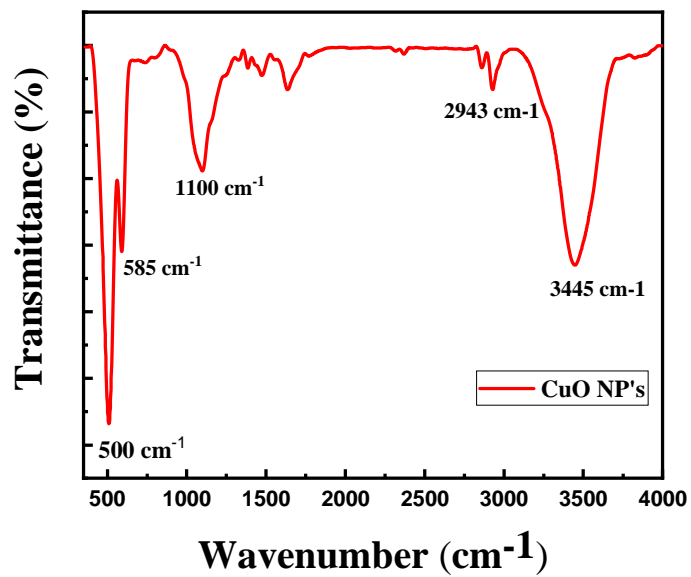
**Figure-3. UV-Visible spectrum of CuO NPs.**

The optical properties of Nanomaterials can be analyzed through this technique. The UV visible spectra were recorded in the wavelength range 200-800 nm. Band gap can be calculated from UV-Vis spectroscopy. The calculated band gap from UV spectra found to be 4.1 eV which was larger than band gap of bulk CuO due to quantum size effect [14,15]. The maximum absorbance was found at wavelength 310 nm. As size of nanoparticle decreases band gap of nanoparticles increases. According to literature, the band gap of nanoparticles was found to be 3-4 eV [16]. It is clearly seen that UV spectroscopy study in our work are well matches with literature.

### 3.4 FT-IR Study

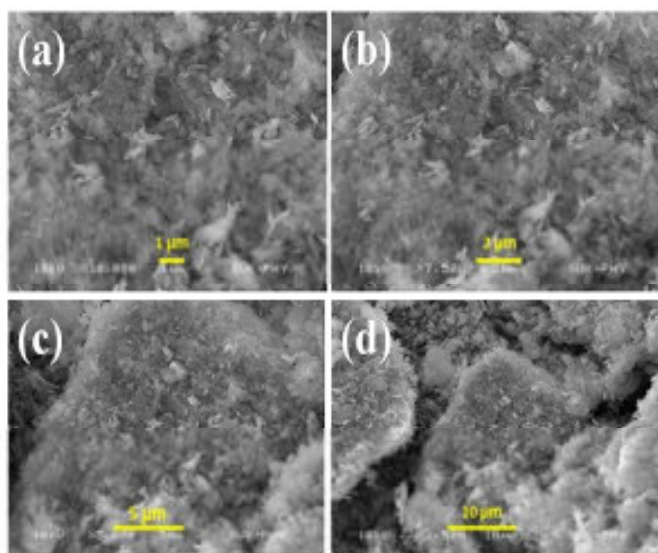
The chemical bonding of copper oxide nanoparticles synthesized using hydrothermal method was examined using FT-IR. 400 - 4000  $\text{cm}^{-1}$  wavenumber range was used to record the FTIR spectrum of CuO NPs. The peaks located at 500  $\text{cm}^{-1}$  and 585  $\text{cm}^{-1}$  showed the formation of pure copper oxide nanoparticles. A peak situated at 1100  $\text{cm}^{-1}$  attributed to the stretching mode of pyrrole ring and vibration mode of C-N bond. A peak located at 2943  $\text{cm}^{-1}$  showed C-H bond of indole moiety (alkaloids) and peak centered at 3445  $\text{cm}^{-1}$  reveals O-H stretching due to water molecule or

moisture present in the sample [17]. It is obvious that our results closely reflect the



literature.

**Fig. 4** FTIR spectrum of CuO NPs



### 3.5 SEM Study

**Figure-5.** SEM micrographs of CuO NPs.

The surface morphological study of copper oxide nanoparticles was confirmed by scanning electron microscopy. Figure-5. represents SEM micrographs of CuO NPs. It is observed that nanoparticles formed nanoflakes morphology [18]. In literature, number of morphologies has been reported like nanorods, nanospheres, nanoflakes, nanograins [3, 7-9, 15, 18]. It is confirmed that our results are well agreement with literature.

### 3.6 Antibacterial Activity of *Bacillus Subtilis* and *E. coli*

Antibacterial activity of CuO NPs was examined against *Bacillus subtilis* and *E. coli*. Figure-6. represents the antibacterial activity of CuO NPs against *Bacillus subtilis* and *E. coli* using disk diffusion assay[19]. The disk diffusion method was used to determine susceptibility of bacterial species (*Bacillus subtilis* and *E. coli*). The diameter of zone laid out magnitude of susceptibility of bacteria. The antibiotic used as positive control and distilled water used as negative control for comparison. In this method, the sterile Muller Hinton agar plate was prepared. Then the test organism spread over plate and by borer wells are prepared and then 50  $\mu$ L sample was added to the well from 1 mg/mL stock solution of CuO NPs. The plates were incubated at 37 $^{\circ}$  C for 24 hours. After 24 hours of incubation *Bacillus subtilis* exhibited 8 mm zone of inhibition in comparison with the standard antibiotic cefotaxime (15 mm) and *E. coli* displayed 7 mm zone of inhibition as compared to the antibiotic cefotaxime (17 mm). It can be seen that gram positive bacteria (*Bacillus subtilis*) and gram-negative bacteria (*E. coli*) displayed significant results. Hence copper oxide nanoparticles exhibited good antibacterial activity against gram positive and gram-negative bacterial species. The comparison with literature is summarized in table below:

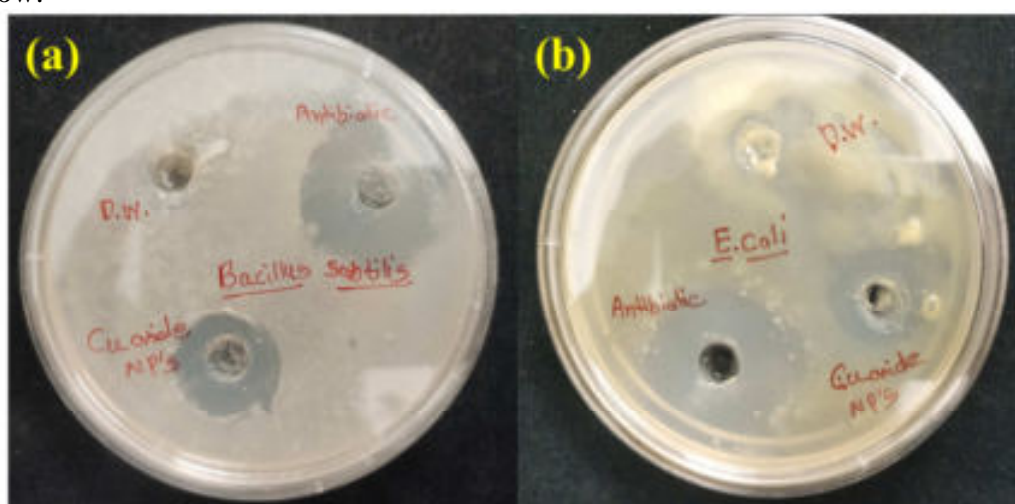
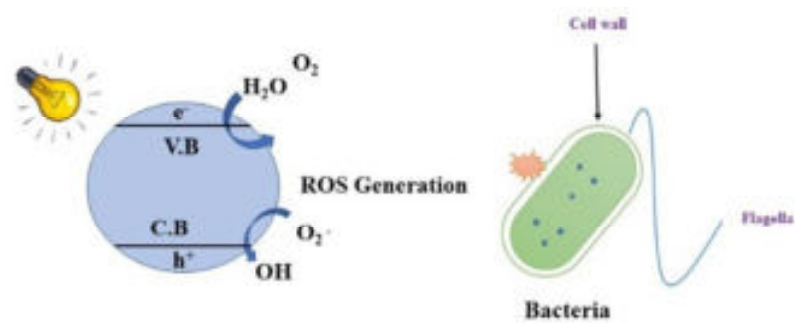


Figure-6. Antibacterial activity of a) *Bacillus subtilis* and b) *E. coli*

**Table-1. Comparison of different bacteria based on copper oxide reported in literature.**

Method	Morphology	Bacterial species	Zone of inhibition (mm)	Ref.
Green approach	Grain	<i>S. aureus</i>	7	[20]
Biosynthesis	Rectangular	<i>S. aureus</i>	6	[12]
Biosynthesis	-	<i>S. aureus</i>	7	[21]
Hydrothermal	Flakes	<i>E. coli</i>	7	This work
Hydrothermal	Flakes	<i>Bacillus subtilis</i>	8	This work

### 3.7 Antibacterial Mechanism of Copper Oxide Nanoparticles



**Figure-7. Antibacterial mechanism of copper oxide nanoparticles**

**Figure-7.** illustrates antibacterial mechanism of copper oxide nanoparticles. When the light incident on reaction sample, electrons excite from valence band to conduction band by leaving holes in valence band. Holes oxidize the water molecule

in the reaction sample to more reactive OH radical owing to the presence of electrons in conduction band. The oxygen molecule gets reduced to  $O^{2-}$  radicals and  $H_2O_2$  reduced to OH radical and these radicals are called reactive oxygen species (ROS). This ROS can directly break cell wall and kill the bacteria. This ROS are necessary to kill the different bacterial species [22].

#### 4. CONCLUSION

We have successfully synthesized copper oxide nanoparticles by hydrothermal method. The phase and crystallite size of CuO NPs confirmed by using X-Ray diffraction pattern. Absorbance and band gap confirmed by using UV visible spectroscopy. Scanning electron microscopy showed flake like morphology of copper oxide nanoparticles. The crystallite size found to be 16.87 nm from Scherrer formula. The band gap of copper oxide nanoparticles was found to be 4.1 eV. FTIR peaks in the range  $500 - 1100\text{ cm}^{-1}$  revealed formation of pure CuO. Scanning electron microscopy showed the nanoflakes morphology. The reactive oxygen species (ROS) are necessary for antibacterial activity and successfully produced by copper oxide nanoparticles synthesized via hydrothermal approach. ROS are necessary to kill the bacterial cell wall and to produce oxidative stress in bacteria. By causing the oxidative stress in the bacteria it is possible to break the cell wall and responsible for contact killing of various bacterial species. This work has the potential to provide insights into the properties and applications of copper oxide nano flakes as antimicrobial agents, and to contribute to the development of more sustainable and effective methods for controlling bacterial growth. The prepared copper oxide nanoparticles exhibited good antibacterial activity against *Bacillus subtilis* and *E. coli*.

#### ACKNOWLEDGEMENT

The authors are thankful to DST-PURSE Phase II (2018-2023) and the UGC DSA Phase II (2018-2020) Program for providing research facilities at the Department of Physics, Shivaji University, Kolhapur, M.S., India.

#### REFERENCES

1. Pendashteh, A., Mousavi, M., Rahmanifar, M. (2013) *Electrochimica Acta*, 88, 347–357.
2. Tran, T., Viet tuyen, N. (2014) *International Scholarly Research Notices*, 2014,
3. Jabbar, S. M. (2017) *Al-Khwarizmi Engineering Journal*, 12, 4, 126-131.

4. Vasantharaj, S., Sathiyavimal, S., Senthilkumar, P., LewisOscar, F., Pugazhendhi, A. (2019) *Journal of Photochemistry and Photobiology B: Biology*, 192, 74-82.
5. Zou, Y.L., Li, Y., Li, J.G., Xie, W.J. (2012) *Chemical Papers*, 66, 4, 278-283.
6. Lanje, A., Sharma, S., Pode, R., Ningthoujam, F. N. A. S. R. (2010) *Advances in Applied Science Research*, 2.
7. Ananth, A., Subramanian, D., Heo, S.M., Mok, Y. S. (2015) *Chemical Engineering Journal*, 262, 179–188.
8. Lv, Y., Li, L., Yin, P., Lei, T. (2020) *Dalton Transactions*, 49, 15, 4699-4709.
9. Ahamed, M., Alhadlaq, H. A., Khan, M. A. M., Karuppiah, P., Al-Dhabi, N. A. (2014) *Journal of Nanomaterials*, 2014, 637858.
10. Raul, P. K., Senapati, S., Sahoo, A. K., Umlong, I. M., Devi, R. R., Thakur, A. J., Veer, V. (2014) *RSC Advances*, 4, 76, 40580-40587.
11. Taran, M., Rad, M., Alavi, M. (2017) *Journal of pharmaceutical sciences*, 23, 3, 198-206.
12. Rad, M., Taran, M., Alavi, M. (2018) *Journal of Nanomedicine and Engineering*, 10, 25-33.
13. Shaffiey, S., Shapoori, M., Bozorgnia, A., Ahmadi, M. (2013) *Nanomedicine journal*, 1, 198-204.
14. Syame, S. M., Mohamed, W., Mahmoud, R. K., Omara, S. T. (2017) *Oriental Journal of Chemistry*, 33, 6, 2959-2969.
15. Swarnkar, R. K., Singh, S. C., Gopal, R. (2009) *AIP Conference Proceedings*, 1147, 1, 205-210.
16. Dhineshbabu, N. R., Rajendran, V., Nithyavathy, N., Vetumperumal, R. (2016) *Applied Nanoscience*, 6, 933-939.
17. Elango, M., Deepa, M., Subramanian, R., Mohamed, M. A. (2018) *Polymer-Plastics Technology and Engineering*, 57, 14, 1440-1451.
18. Eslami, A., Modanlou, N., Hosseini, S., Abbasi, M. (2017) *Central European Journal of Energetic Materials*, 14, 152-168.
19. Jeronsia, J., Raj, D. J., Joseph, A., Rubini, K., Das, S. (2016) *Journal of Medical Sciences (Taiwan)*, 36, 145-151.
20. Sutradhar, P., Saha ,M., Maiti, D. (2014) *Journal of Nanostructure in chemistry*.
21. Ginjupalli, K. A., Ramkrishna., Shaw, T., Tellapragada, C., Gupta, L. K., Upadhya, N. (2016), *International Conference on Advanced Material (SCICON 16)*.
22. Katwal, R., Kaur, H., Sharma, G., Naushad, Mu., Pathania, Deepak. (2015) *Journal of Industrial and Engineering Chemistry*, 2566, 1-12.

# Hydrothermally Prepared WO<sub>3</sub>-Nanostructure as an Efficient Electrode Material for Supercapacitor

U. V. Shembade<sup>a</sup>, S. D. Dhas<sup>a</sup>, M. D. Patil<sup>a</sup>, T. T. Bhosale<sup>a</sup>, N. B. Chougale<sup>a</sup>, M. G. Magadum<sup>a</sup>, S. V. Jadhav<sup>a</sup>, S. R. Ghatage<sup>b</sup>, A. V. Moholkar<sup>a\*</sup>

<sup>a</sup>Department of Physics, Shivaji University, Kolhapur, 416 004, India.

<sup>b</sup>Department of Physics and Electronics, Gopal Krishna Gokhale College, Kolhapur 416001 (MS) India.

\*Corresponding author: avm\_phy@unishivaji.ac.in

---

## ABSTRACT

Here, we describe the simple hydrothermal approach to synthesize WO<sub>3</sub> nanostructured material. The X-ray diffraction technique (XRD), scanning electron microscopy (SEM), surface wettability test, and electrochemical studies including cyclic voltammetry (CV) and galvanostatic charge-discharge (GCD) were used to characterize the WO<sub>3</sub>-nanostructure (NSs) electrode material. The monoclinic crystalline nature of WO<sub>3</sub>-NSs was revealed by an XRD signal. The encapsulated nanoflowers with a non-uniform porosity were observed in the SEM micrographs. The electrochemical properties of WO<sub>3</sub>-stainless steel (WO<sub>3</sub>-SS) electrodes have been examined in 1M KOH electrolyte, and they showed good electrochemical performance. Moreover, WO<sub>3</sub>-stainless steel was a battery-type material that provides specific capacitance (SCs) of 201 F/g at scan rates of 5 mV/s and a good energy density of 1.85 Wh/kg with a power density of 67.5 W/kg at a current density of 3 mA/cm<sup>2</sup>.

## KEYWORDS

Hydrothermal, Metal oxide, Nanoflowers, Supercapacitor.

.....

## 1. INTRODUCTION

Today's world is dealing with an unexpected range of environmental issues, mostly as a result of climate change brought on by the emissions of gases that cause global warming. Non-renewable fossil fuel use is anticipated to significantly decrease during the next few years. As a result, it is necessary to use alternate, sustainable, and renewable energy sources. Due to the rising growth in population, demand for global energy [1]. The device will address these shortcomings required in current market trends i.e., supercapacitors, and batteries [2]. Electrostatically double-layer capacitors (EDLC) and pseudo-capacitors are the two forms of supercapacitors. The majority of EDLCs are carbon-based materials, and due to their high surface-to-volume ratio and broad operating potential window, they are widely used in energy storage systems. Although materials like metal oxides (MOs), transition metal oxides (TMOs), and conducting polymers can operate as pseudocapacitors to store charge

through a quick redox reaction at or near the electrode surface [3]. Various electrode materials, including carbon-based materials, conducting polymers, and TMOs, have been studied for SC. TMOs are the most promising active electrode material. They produce capacitance from extremely quick redox reactions and, more significantly, because they store more energy than EDLCs [4]. Usually, the active electrode material for SCs, such as  $\text{MnO}_2$ ,  $\text{NiO}$ ,  $\text{WO}_3$ , and  $\text{Ni}(\text{OH})_2$  [5-7] have been used as active electrode material for SCs. The scientific community has paid a lot of interest to tungsten oxide, due to its properties such as electrochemically stable n-type semiconductor metal oxide, and present in a variety of applications [8]. Pristine  $\text{WO}_3$  is an intriguing material, because of its notable structural stability, high conductivity, ease of structural changes, and sub-stoichiometric phase transitions. There has been a considerable increase in  $\text{WO}_3$  in the application of photo-catalysis, gas sensing, and electrochromic devices [9]. It has long been accepted that structural flaws rather than just electrical structures have a larger role in determining the characteristics of metal oxides. Additionally, oxygen vacancies can improve electrode material's conductivity and activity. Consequently, tungsten oxide must be introduced in the field of charge storage mechanisms [10]. There are numerous reports on the use of  $\text{WO}_3$  as an electrode material for supercapacitors. For instance, Xu et al. show the hydrothermally created mesoscopic  $\text{WO}_3$  microspheres. The mesoscopic  $\text{WO}_3$  microspheres give the required porosity structures and surface area that is provided by entwined nanofibers for easy electrolyte flow and quick reaction kinetics [11]. Chacon et al. have reported the synthesis and characterization of  $\text{WO}_3$  polymorphs using a solvothermal method. By adjusting the water content in the solvothermal process, they have reported the crystal forms of  $\text{WO}_3$  to be monoclinic, hexagonal, and orthorhombic [12]. Huang and colleagues noticed how the hydrothermal temperature affected the shape, phases, and structure of  $\text{WO}_3$  and examined it for photochromic and electrochemical study [13]. In the current study,  $\text{WO}_3$ -NSs are prepared using a straightforward simple hydrothermal method, and electrochemical performance is assessed using inexpensive stainless-steel substrates in an aqueous KOH electrolyte.

## **2. EXPERIMENTAL SECTION**

### **2.1. Materials**

Sodium tungstate ( $\text{Na}_2\text{WO}_4 \cdot 2\text{H}_2\text{O}$ ), concentrated hydrochloric acid (HCl), hydrogen peroxide ( $\text{H}_2\text{O}_2$ ), double distilled water (DDW), Stainless Steel (SS) substrate, polyvinylidene difluoride (PVDF), Activated carbon (AC), and N-methyl-2-pyrrolidone (NMP) was purchased from Loba Chemie Pvt. Ltd., Mumbai (India). All chemicals were of analytical grade, additional purification was not necessary.

## 2.2. Synthesis of WO<sub>3</sub> NSs

To make WO<sub>3</sub>-NSs, 20 ml of DDW and 0.1 M sodium tungstate were dissolved in a DDW. For 20 minutes, the mixture was magnetically stirred, and add 5 ml of HCl into the precursor solution until it turned yellowish-colored. After, 5 min add 5 ml of H<sub>2</sub>O<sub>2</sub> to form a well-dispersed solution, and the mixture was thoroughly poured into a Teflon-lined stainless steel still autoclave. The autoclave was sealed and heated for 10 hours at 180°C. The well-prepared powder was taken out from the naturally cooling furnace after being rinsed several times with DDW and ethanol. It was then dried at 80°C for 2 hours before being annealed at 450°C for 3 hours shown in **Figure-1**.

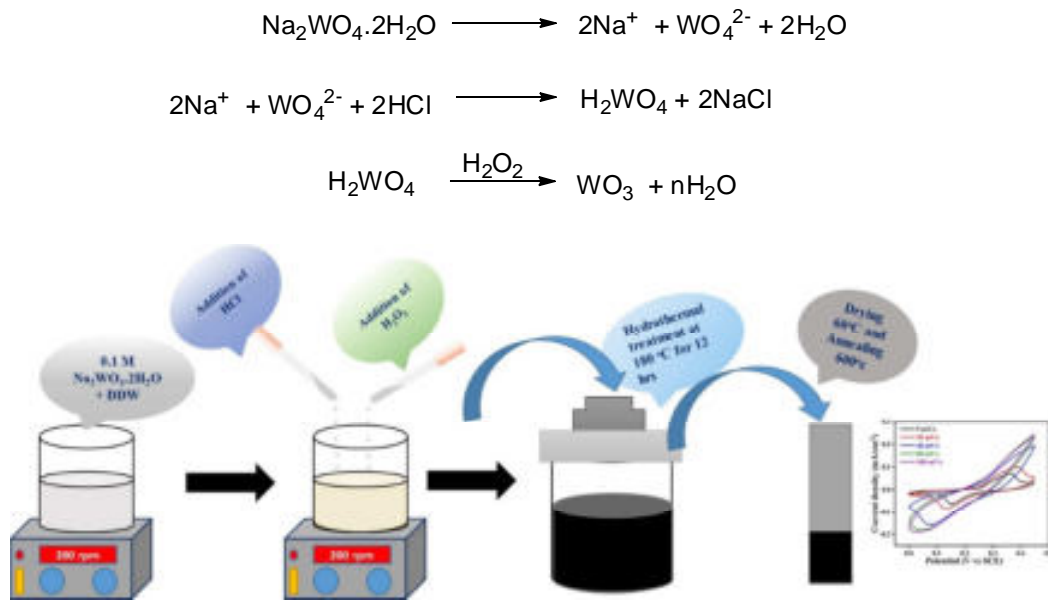


**Figure-1. Schematic for the formation of WO<sub>3</sub>-NSs using the hydrothermal method.**

To create milky white or yellowish tungstic particles, the tungstate ions first go under the treatment of protonation or acidifications. The intermediate H<sub>2</sub>WO<sub>4</sub> ions go through additional hydration to crystallize with water molecules and are kept together by weak intermolecular interactions. This phase is crucial because at this stage the pH and temperature have the most influence over the morphology and size of the nanostructure. The W-O bonds rebuild as the water is removed from the structure, allowing O atoms to join and stack together, causing a phase shift [14, 15]

### 2.3. Characterizations

The X-ray diffraction (XRD) for WO<sub>3</sub>-NSs was completed using a D2 Phaser diffractometer from Bruker Ltd. (Germany) (Cu-K $\alpha$ =1.5405Å). The surface morphology of WO<sub>3</sub>-NSs was studied using scanning electron microscopy (SEM) methods. The surface wettability test was used to determine the contact angle between the water molecule and the WO<sub>3</sub>-SS electrode. A three-electrode assembly in 1 M KOH electrolyte was used to measure the electrochemical characteristics of the WO<sub>3</sub>-SS electrode (Model-VMP3- Bio-Logic, France).

### 2.4. Preparation of WO<sub>3</sub>-SS electrode for electrochemical study

The conductive component (carbon black), binder (PVDF), and active material were combined in a weight ratio of 8:1:1 to form the WO<sub>3</sub>-SS electrode. The combination was thoroughly grounded, and add 3 drops of the NMP which gives the resultant slurry; further, it was deposited onto a substrate made of 1 ×1 cm<sup>2</sup> of SS and dried at 60 °C. A three-electrode system was used to conduct electrochemical analysis on the properly manufactured WO<sub>3</sub>-SS electrode in 1 M KOH electrolyte.

## 3. RESULTS AND DISCUSSION

The phase identification of WO<sub>3</sub>-NSs was accomplished using the powder XRD, and the relevant profiles are displayed in **Figure-2**. For the monoclinic phase of WO<sub>3</sub>, the more intense and sharp diffraction peaks were observed at 2 $\theta$  degree of 23.14°, 23.61°, 24.37°, 26.62°, 28.79°, 33.30°, 34.06°, 35.56°, 41.68°, 47.28°, 48.28°, 50.32°, 53.52° and 55.83° corresponds to their respective (hkl) planes (020), (200), (002), (120), (112), (022), (220), (122), (222), (312), (040), (-114), (024) and (142) for the monoclinic phase of WO<sub>3</sub> (JCPDS 00-024-0747) [16].

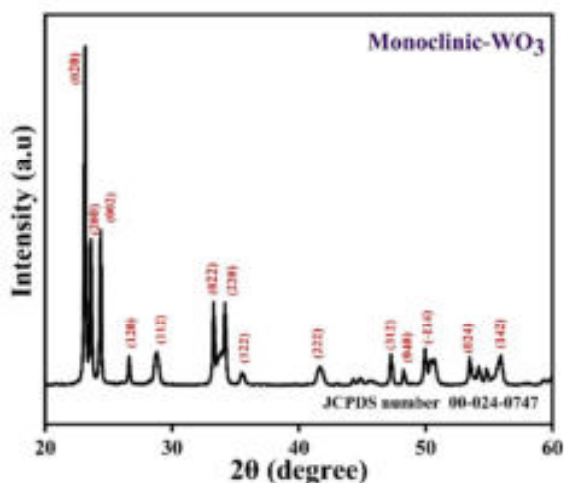


Figure-2. The XRD patterns of WO<sub>3</sub>-NSs.

The peak intensities in XRD patterns are attributed to the crystalline nature of WO<sub>3</sub> material. The average crystallite size (D) and the lattice parameters including interplanar spacing 'd', for different planes of monoclinic WO<sub>3</sub>-NSs are calculated and reported in **Table-1**

$$D = \frac{0.9\lambda}{\beta \cos\theta} \quad (4)$$

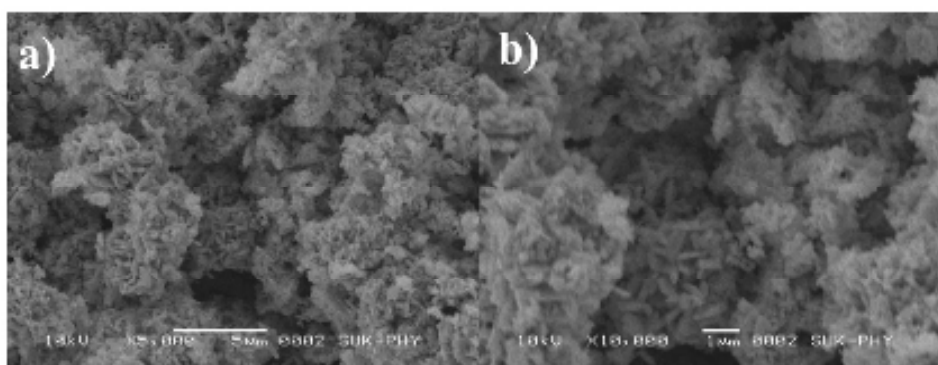
Here, the wavelength of the source ( $\lambda=1.5405 \text{ \AA}$ ),  $\theta$  is the Bragg diffraction angle and  $\beta$  is the full-width half maxima (FWHM). The table shows the typical crystallite size of WO<sub>3</sub>-NSs at various (hkl) planes and shows the 6 nm average crystallite size for WO<sub>3</sub>-NSs.

**Table-1. Crystal structure parameters for WO<sub>3</sub>-NSs material synthesized via hydrothermal method.**

2 $\theta$ (Degree)	Miller indices (hkl)	Interplanar distance (d) ( $\text{\AA}$ )	FWHM ( $\beta$ ) (Rad.)	Lattice parameters (a=b=c) ( $\text{\AA}$ )	Crystallite size (D) (nm)	The average crystallite size (nm)
23.16	(020)	3.76	0.82043	7.53	9.8	6
23.58	(200)	3.64	0.8201		9.90	
24.38	(002)	3.64	0.82018		9.91	
26.59	(120)	3.34	1.76646		4.62	
28.93	(112)	3.08	1.7666		4.64	
33.26	(022)	2.69	1.76643		4.69	
34.18	(220)	2.62	1.76646		4.71	
41.90	(222)	2.15	1.76643		4.82	
47.26	(312)	1.82	1.76643		4.91	
48.28	(040)	1.81	1.76643		4.93	
49.95	(-114)	1.79	1.76657		4.96	

53.47	(024)	1.64	1.76647		5.04	
55.92	(142)	1.63	1.76648		5.09	

Scanning electron microscopy was used to study the surface morphology of WO<sub>3</sub>-NSs at low (X 5,000) and high (X 10,000) magnifications using 10 kV potential. The surface morphology of WO<sub>3</sub>-NSs exhibit irregularly shaped nanoflowers, some microporous gaps, and overgrowth in some locations, as shown in **Figure-3**. The high surface area of these NFs gives an advantage for the electrochemical characteristics. The high porosity and large surface area make it simple for electrolyte ions to access during the redox process [17]. These highly functional NSs like morphology are used for energy storage, and it has great



potential for use in next-generation smart electrochemical components. Therefore, the crystal structure of WO<sub>3</sub>-NSs has a significant impact on electrochemical characteristics

**Figure-3. SEM micrographs of WO<sub>3</sub>-NSs at low (X 5,000) and (X 10,000) high magnifications.**

The surface wettability test investigates how a solid/liquid contact interacts. The suitable interaction between the active electrode material and electrolyte is indicated by the hydrophilic character. With a contact angle of 70°, it has been discovered that the surfaces of WO<sub>3</sub>-SS are hydrophilic to water presented in **Figure-4**. MOs materials are predicted to have extremely high surface energies due to their hydrophobicity. The low contact angle value for the WO<sub>3</sub>-SS electrode is beneficial to improve the electrochemical performance [18].

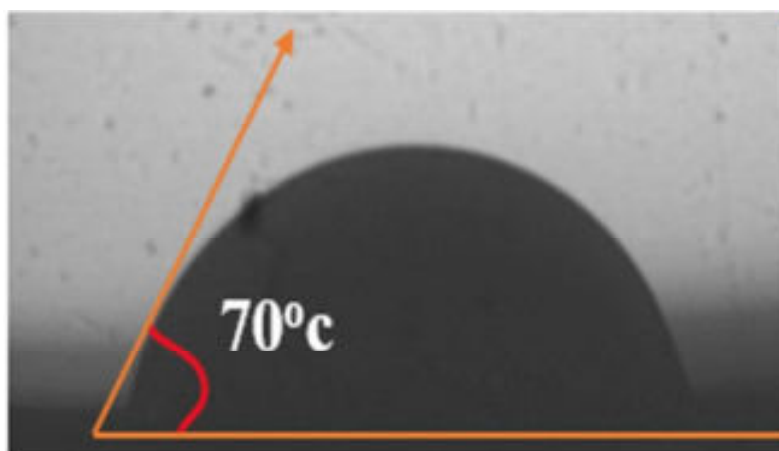


**Figure-4. Surface wettability test of WO<sub>3</sub>-SS electrode**

### 3.1. Electrochemical study

**Figure-5** shows the cyclic voltammogram of the WO<sub>3</sub>-SS electrode at various scan rates in the potential range of (0 V to 0.45 V) vs SCE in an aqueous 1 M KOH solution. The oxidation and reduction peaks of the WO<sub>3</sub>-SS electrode material represent the CV plots at the same potential, but the current density varied, from various scan rates. The atomic size of the components is responsible for the shift in the current density of the WO<sub>3</sub>-SS electrode. The pseudocapacitive character of the WO<sub>3</sub>-SS electrode is confirmed by the emergence of redox peaks in the CV plots. Eventually, at a low scan rate, the well-developed nature of the CV curve indicates good electrochemical performance and better reversibility to the WO<sub>3</sub>-SS electrode. It is easy to see how the scan rate causes the area under the CV curve to increase and the intercalation of H<sup>+</sup> ions onto the surface of WO<sub>3</sub> from the electrolyte. The subsequent response mechanism can be explained by equation (5) [1],



From the cyclic voltammetry curve, the Cs of the WO<sub>3</sub>-SS electrode is determined by using Eq. (6).

$$C_s = \frac{\int I(V)dv}{mv\Delta V} \quad (6)$$

here,  $\int I(V) dv$  indicates the absolute area under the curve, m is the mass of the working electrode, v is the scan rate in millivolts per second and  $\Delta V$  is the potential window in volts. The SCs achieved from CV curves at different scan rates

of 5 mV/s, 10 mV/s, 40 mV/s, 80 mV/s & 100 mV/s are 201 F/g, 160 F/g, 93 F/g, 59 F/g, and 50 F/g respectively and shown in **Table-2**. As the scan rate increases, the  $C_s$  of the  $WO_3$ -SS electrode decreases.

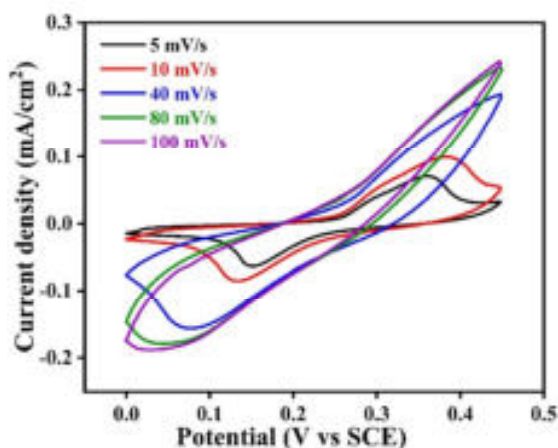


**Figure-5.** CV curves obtained for the various scan rates of  $WO_3$ -SS electrodes in 1 M KOH electrolyte.

**Table 2.** Summarized data of gravimetric SCs for the  $WO_3$ -SS electrodes using CV curves in 1 M KOH electrolyte.

Sr. No.	Scan rate (mV/s)	Specific capacitance (F/g)
1	5	201
2	10	160
3	40	93
4	80	59
5	100	50

The three-electrode system depicted in **Figure-6** is used to record the galvanostatic charge/discharge (GCD) curves of  $WO_3$ -SS electrodes at different current densities, including 5, 7, 9, and 11 mA/cm<sup>2</sup>. The CV curves for  $WO_3$ -SS electrodes reveal that they are pseudocapacitive, and their GCD curves demonstrate the departure from the

triangular form in the potential window of 0 V to 0.4 V which confirms the pseudocapacitive nature of the working electrode.

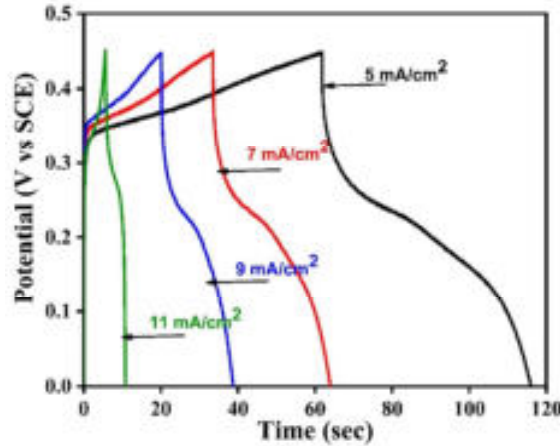


**Figure-6. GCD curves obtained for the current density of WO<sub>3</sub>-SS electrodes in 1 M KOH electrolyte.**

The GCD plots are used to calculate the gravimetric SCs of the WO<sub>3</sub>-SS electrodes using the following equation <sup>12</sup>

$$C_g = \frac{I \Delta t}{m (\nabla v)} \quad (7)$$

where  $m$  is the activated mass electrode material (g),  $\nabla v$  is the operating potential window, and  $C_g$  denotes the SCs (F/g) of the WO<sub>3</sub>-SS electrodes. The highest SCs are measured using the GCD curve at 66 F/g in 3 mA/cm<sup>2</sup>, and the remaining current densities for the WO<sub>3</sub>-SS electrode are 58 F/g, 46 F/g, and 40 F/g, respectively, as shown in **Table-3**. The  $C_g$  value decreased as the current density increased. It is important to note that the OH<sup>-</sup> ions have more time to interact with the working electrode at low current densities than at high current densities. The aforementioned findings demonstrate that the shape, chemical constitution, and electrolyte concentration all affect the super capacitive capabilities of WO<sub>3</sub>-SS electrode material. The formulas for calculating energy density ( $E_d$ ), power density ( $P_d$ ), and Columbic efficiency are as follows [10],

$$E_d = \frac{0.5 \cdot C_g \cdot V^2}{3.6} \quad (8)$$

$$P_d = \frac{S.E. \cdot 3600}{t_d} \quad (9)$$

$$\eta = \frac{t_d}{t_c} * 100 \% \quad (10)$$

At varying current densities, the energy density of the WO<sub>3</sub>-SS electrode varies; the highest energy density is reached at a current density of 3 mA/cm<sup>2</sup> (1.85 Wh/kg at 67.5 W/kg). The Coulombic efficiency values achieved are 78 %, 85 %, 90 %, and 96 % at 3, 5, 7, and 9 mA/cm<sup>2</sup> respectively

**Table-3. Summarized data of gravimetric SCs for the WO<sub>3</sub>-SS electrodes using GCD curves in 1 M KOH electrolyte.**

Current density (mA/cm <sup>2</sup> )	SCs (F/g)	Ed (Wh/kg)	Pd (W/kg)	Coulombic Efficiency (η) (%)
5	66	1.85	67.5	78
7	58	1.65	112.5	85
9	48	1.31	157.5	90
11	38	1.09	199.7	96

EIS is the best method to measure the internal resistance and to identify the frequency response nature of the electrode material.

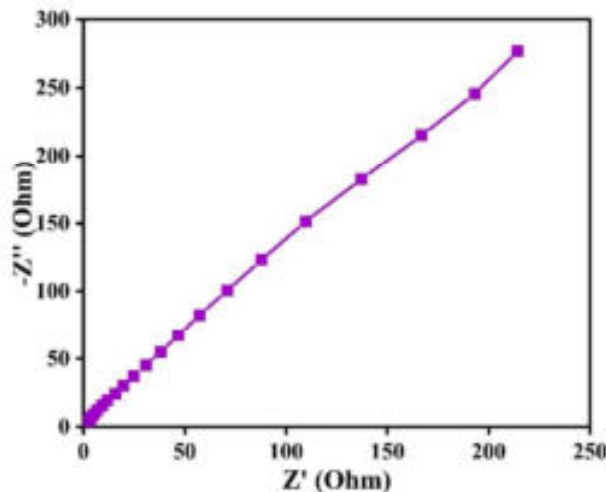


**Figure-7. EIS data obtained for WO<sub>3</sub>-SS electrode in 1 M KOH electrolyte.**

EIS measurement of the WO<sub>3</sub>-SS electrode is carried out over a frequency range of 0.1 Hz to 100 MHz. It represents the plot between the imaginary part -Z''

against the real part  $Z'$ , also known as the Nyquist plot. **Figure-7** shows the Nyquist plots of the  $\text{WO}_3$ -SS electrode in 1 M KOH electrolyte. The  $\text{WO}_3$ -SS electrodes show lower values of  $R_s$  and  $R_{ct}$  which are necessary to store more charges and provide more power. However, the  $\text{WO}_3$ -SS electrodes do not show the semicircle on the Nyquist plot, which indicates less or no charge transfer resistance which provides easy access for electrolyte ions in the low and high-frequency region.

#### 4. CONCLUSION

We report the hydrothermally formed monoclinic phase of  $\text{WO}_3$ -NSs, which is being investigated for the charge storage mechanism. The monoclinic structure of the  $\text{WO}_3$  material is confirmed by the XRD pattern, which also shows its crystalline nature. A non-uniform nanoflowers-like shape across the surface in the SEM micrograph is observed. The hydrophilic character of the  $\text{WO}_3$  material is demonstrated by the contact angle study for the  $\text{WO}_3$ -SS electrode. A three-electrode configuration in 1 M KOH electrolyte has been used to examine the super capacitive characteristics of the  $\text{WO}_3$ -SS electrode material. The CV and GCD studies show that the  $\text{WO}_3$ -SS electrode has moderate electrochemical performance.

#### ACKNOWLEDGMENT

Author A. V. Moholkar acknowledges DST-SERB for providing funding under project No [SERB/ F/1699/2018-19]. All authors are thankful to the Special Assistance Program (SAP) [F.530/16/DSA-II/2018 (SAP-1)] and PIFC (Physics Instrumentation Facility Centre), Department of Physics for providing characterization facilities for the present research work.

#### REFERENCES

1. Dhas, S. D., Maldar, P. S., Patil, M. D., Hubali, K. M., Shembade, U. V., Abitkar, S. B., Waikar, M. R., Sonkawade, R. G., Agawane, G. L., Moholkar, A. V. Hydrothermal Synthesis of Mesoporous  $\text{NiMnO}_3$  Nanostructures for Supercapacitor Application: Effect of Electrolyte. *Journal of Energy Storage* 2021, 35, 102277.
2. Tehrani, F. S., Ahmadian, H., Aliannezhadi, M. Hydrothermal Synthesis and Characterization of  $\text{WO}_3$  Nanostructures: Effect of Reaction Time. *Material Research Express* 2020, 7 (1).
3. Pang, H. F., Xiang, X., Li, Z. J., Fu, Y. Q., Zu, X. T. Hydrothermal Synthesis and Optical Properties of Hexagonal Tungsten Oxide Nanocrystals Assisted by Ammonium Tartrate. *Physica Status Solidi Application and Material Science*. 2012, 209 (3), 537–544.

4. Sun, K., Hua, F., Cui, S., Zhu, Y., Peng, H., Ma, G. An Asymmetric Supercapacitor Based on Controllable WO<sub>3</sub> nanorod Bundle and Alfalfa-Derived Porous Carbon. *RSC Advance* 2021, 11 (59), 37631–37642.
5. Qiu, M., Sun, P., Shen, L., Wang, K., Song, S., Yu, X., Tan, S., Zhao, C., Mai, W. WO<sub>3</sub> Nanoflowers with Excellent Pseudo-Capacitive Performance and the Capacitance Contribution Analysis. *Journal of Material Chemistry A* 2016, 4 (19), 7266–7273.
6. Gupta, S. P., Nishad, H. H., Chakane, S. D., Gosavi, S. W., Late, D. J., Walke, P. S. Phase Transformation in Tungsten Oxide Nanoplates as a Function of Post-Annealing Temperature and Its Electrochemical Influence on Energy Storage. *Nanoscale Advance* 2020, 2 (10), 4689–4701.
7. Jayachandiran, J., Arivanandhan, M., Padmaraj, O., Jayavel, R., Nedumaran, D. Investigation on Ozone-Sensing Characteristics of Surface Sensitive Hybrid RGO/WO<sub>3</sub> Nanocomposite Films at Ambient Temperature. *Advance Composite Hybrid Material* 2020, 3 (1), 16–30.
8. Ganbavle, V. V., Agawane, G. L., Moholkar, A. V., Kim, J. H., Rajpure, K. Y. Structural, Optical, Electrical, and Dielectric Properties of the Spray-Deposited WO<sub>3</sub> Thin Films. *Journal of Material Engineering Performance* 2014, 23 (4), 1204–1213.
9. Patil, C. E., Tarwal, N. L., Jadhav, P. R., Shinde, P. S., Deshmukh, H. P., Karanjkar, M. M., Moholkar, A. V., Gang, M. G., Kim, J. H., Patil, P. S. Electrochromic Performance of the Mixed V<sub>2</sub>O<sub>5</sub>-WO<sub>3</sub> Thin Films Synthesized by Pulsed Spray Pyrolysis Technique. *Current Applied Physics* 2014, 14 (3), 389–395.
10. Hunge, Y. M., Mohite, V. S., Kumbhar, S. S., Rajpure, K. Y., Moholkar, A. V., Bhosale, C. H. Photoelectrocatalytic Degradation of Methyl Red Using Sprayed WO<sub>3</sub> Thin Films under Visible Light Irradiation. *Journal of Material Science and Material Electronics* 2015, 26 (11), 8404–8412.
11. Xu, J., Li, C., Chen, L., Li, Z., Bing, P. Anchoring Carbon Layers and Oxygen Vacancies Endow WO<sub>3</sub>-x/C Electrode with High Specific Capacity and Rate Performance for Supercapacitors. *RSC Advance*. 2019, 9 (49), 28793–28798.
12. Zheng, F., Song, S., Lu, F., Li, R., Bu, N., Liu, J., Li, Y., Hu, P., Zhen, Q. Hydrothermal Preparation, Growth Mechanism and Supercapacitive Properties of WO<sub>3</sub> Nanorod Arrays Grown Directly on a Cu Substrate. *Crystal Engineering Communication* 2016, 18 (21), 3891–3904.
13. Gao, L., Wang, X., Xie, Z., Song, W., Wang, L., Wu, X., Qu, F., Chen, D.,

- Shen, G. High-Performance Energy-Storage Devices Based on WO<sub>3</sub> Nanowire Arrays/Carbon Cloth Integrated Electrodes. *Journal of Material Chemistry* 2013, 1 (24), 7167–7173.
14. Shinde, P. A., Lokhande, A. C., Patil, A. M., Lokhande, C. D. Facile Synthesis of Self-Assembled WO<sub>3</sub> Nanorods for High-Performance Electrochemical Capacitor. *Journal of Alloys Compounds* 2019, 770, 1130–1137.
  15. Lokhande, P. E., Kulkarni, S., Chakrabarti, S., Pathan, H. M., Sindhu, M., Kumar, D., Singh, J., Kumar, A., Kumar Mishra, Y., Toncu, D. C., Syväjärvi, M., Sharma, A., Tiwari, A. The Progress and Roadmap of Metal–Organic Frameworks for High-Performance Supercapacitors. *Coordination Chemistry Review* 2022, 473, 214771.
  16. Saini, S., Chand, P. Effect of Aqueous Electrolytes on H-WO<sub>3</sub> Nanorods as an Electrode Material for Supercapacitor Application. *Chemical Physics letter* 2022, 802, 139760.
  17. Dhas, S. D., Maldar, P. S., Patil, M. D., Mane, S. A., Waikar, M. R., Sonkawade, R. G., Moholkar, A. V. Fabrication of Efficient Electrochemical Capacitors Rooted in Sol-Gel Derived NiMn<sub>2</sub>O<sub>4</sub> Nanoparticles. *Journal of Electroanalytical Chemistry* 2021, 897, 115548.
  18. Dubal, D. P., Dhawale, D. S., Salunkhe, R. R., Jamdade, V. S., Lokhande, C. D. Fabrication of Copper Oxide Multilayer Nanosheets for Supercapacitor Application. *Journal of Alloys and Compounds* 2010, 492 (1–2), 26–30.

## GUIDELINES FOR CONTRIBUTORS

- 1] **Journal of Shivaji University : Science & Technology** is the publication of Shivaji University, Kolhapur (Maharashtra, India), being published twice a year. It is an academic peer reviewed ISSN approved Journal.
- 2] The Journal welcomes research articles based on original research, review papers, research communication/notes by the faculty and research scholars working in various fields of Science and Technology. Articles/Papers can be submitted in English language only.
- 3] The length of manuscripts should not exceed 6000 words for review article, 5000 words for research article, 2000 words for research communication and 1000 words for research note.
- 4] The article/paper must accompany an **abstract not exceeding 200 words**.
- 5] During writing and submission of a manuscript, please follow the author guidelines available on the home page of Journal of Shivaji University: Science and Technology.
- 6] All the sources of literature referred to while writing the article/paper must be properly cited in the text. The serial numbers of End Notes, if any, must also be indicated within text at appropriate places.
- 7] The listing of references must follow the standard format.
- 8] Tables, charts, maps, figures etc. should be placed at appropriate places in the text of the article/paper and must be numbered serially with suitable headings. The tables should be referred to by their numbers within the text. Art-work for maps, figures and charts should be provided separately, if necessary.
- 9] Only articles evaluated and approved by the subject Experts/Referees/Departmental editorial board are considered for their publication in the Journal. The referees evaluate Article/ Paper drafts in term of structure and organization of paper/argument, originality of the research, appropriateness of abstract and introduction, literature review, methodology and data sources, data/evidence and conclusions, and quality of language.
- 10] The name of the author/co-author of the article being submitted should mentioned on the first page of the article/paper below title of that article. An asterisks (\*) is used for defining corresponding author/s of a manuscript.
- 11] For any other information and for inquiries regarding submitted articles/papers preferably use e-mail communications. **(E-mail : editor.jscitech@unishivaji.ac.in)**
- 12] Manuscript should be sent to email of the Editor (**editor.jscitech@unishivaji.ac.in**) {or associate editor of the concerned subject}, Journal of Shivaji University: Science and Technology, Kolhapur with e-copy only (single M.S. word as well as PDF file).  
**Only research articles/review papers/research communication/notes prepared strictly in accordance with the above guidelines will be sent to referees for their evaluation and opinion about their acceptability or otherwise. We do not send back rejected articles.**

